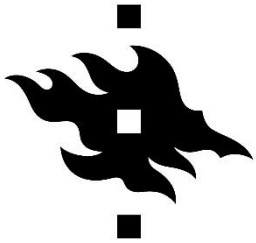

HELSINGIN YLIOPISTO
HELSINGFORS UNIVERSITET
UNIVERSITY OF HELSINKI

Master's Thesis
Master's Programme in Geology and Geophysics

Pedogenic Ferromanganese Nodules in the Late Neogene Sediments of Lantian, Southern Chinese Loess Plateau

Tuomas Junna
06/2020

Supervisors:

Anu Kaakinen (University of Helsinki)
Juha Karhu (University of Helsinki)
Joonas Wasiljeff (University of Helsinki)

UNIVERSITY OF HELSINKI
FACULTY OF SCIENCE
DEPARTMENT OF GEOSCIENCES AND GEOGRAPHY

PL 64 (Gustaf Hällströmin katu 2)
00014 Helsingin yliopisto

HELSINGIN YLIOPISTO
HELSINGFORS UNIVERSITET
UNIVERSITY OF HELSINKI

Tiedekunta – Fakultet – Faculty	Koulutusohjelma – Utbildningsprogram– Degree programme	
Faculty of Science	Master's Programme in Geology and Geophysics	
Tekijä – Författare – Author		
Junna, Tuomas Samuli		
Työn nimi – Arbetets titel – Title		
Pedogenic Ferromanganese Nodules in the Late Neogene Sediments of Lantian, Southern Chinese Loess Plateau		
Opintosuunta – Studieinriktning – Study track		
Hydrogeology and Environmental Geology		
Työn laji – Arbetets art – Level	Aika – Datum – Month and year	Sivumäärä – Sidoantal – Number of pages
Master's thesis	06/2020	73 + 32

Tiivistelmä – Referat – Abstract

Pedogenic ferromanganese nodules and concretions are prevalent redoximorphic features in tropical and sub-tropical soils. The nodules are typically highly enriched in Fe and Mn that are present as oxides, hydroxides and oxyhydroxides. The formation of nodules happens via precipitation and translocation of metals as the soil redox state undergoes cyclical changes between reductive and oxidizing settings. As the nodule elemental distribution and structure is primarily and expression of the prevailing soil redox conditions, Fe-Mn nodules have the potential to be a useful tool of paleoclimatological analysis.

The Chinese Loess Plateau (CLP) is a terrestrial archive for study of changes in the monsoon climate system. During Late Miocene, the intensification of the Asian Monsoon system caused an increase in warmth and humidity in inland Eastern Asia during a global trend of increased aridity and decreasing temperatures. Fe-Mn nodules from three different soil horizons, formed 8.07, 7.7 and 3.7 Ma ago in Lantian, southern CLP, were studied to compare nodules from varying sedimentary settings formed under different moisture regimes.

Using electron microscopy methods, the structure and elemental distribution of nodules were described to compare their redoximorphic features. Large Fe-Mn nodules from floodplain sediments (8.07 Ma) show a well-developed structure, high metal enrichment and signs of variations in rate of formation and dominant redox states. The soil redox conditions are likely primarily controlled by the river flooding. Nodules from two eolian deposits (7.7 Ma and 3.7 Ma) were, on average smaller and showed less metal enrichment, less elemental differentiation and less variance in the dominant redox conditions. Only small, poorly developed nodules were found from older eolian sediments whereas younger soil horizon contained larger nodules with evidence of higher hydromorphism.

While potential for using the nodules from eolian sediments to assess changes in precipitation exists, the lack of paleoclimatological information in smaller nodules, the small sample count, limitations of the methods and variance in depositional settings increase the uncertainty of the interpretation.

Avainsanat – Nyckelord – Keywords

Ferromanganese nodules, Pedogenesis, Lantian, Miocene, Chinese Loess Plateau, Asian Monsoon

Säilytyspaikka – Förvaringställe – Where deposited

HELDA- Digital repository of the University of Helsinki

Muita tietoja – Övriga uppgifter – Additional information

29 figures and 4 tables (appendix not included)

TABLE OF CONTENTS

1. INTRODUCTION

Ferromanganese nodules and concretions are one of the most significant pedogenic components found from subtropical and tropical soils. Fe-Mn nodules typically comprise of soil materials cemented together with Mn and Fe hydroxides, oxyhydroxides and oxides (Cornu et al. 2005). Several studies have described the morphology, mineralogy and chemical speciation of ferromanganese nodules and concretions (Zhang and Karathanasis 1997, Aide 2005, Cornu et al. 2005, Gasparatos et al. 2005, Timofeeva 2008, Szymański et al. 2014).

Fe-Mn nodules and concretions are firm, rounded to sub-rounded morphological elements that display elevated Fe and Mn concentrations compared to the surrounding soil matrix (Aide 2005). Small sized or irregularly shaped nodules often show no internal structure (Timofeeva 2008, Gasparatos 2012), whereas concretions display a distinct concentric layered structure comprising of Mn or Fe enriched rings (Timofeeva 2008). However, both terms are commonly used interchangeably in literature and for brevity, both will be hereafter referred to as nodules.

Fe-Mn nodules are suggested to form in soil horizons that undergo seasonal waterlogging or fluctuations of the water table (McKenzie 1989, Zhang and Karathanasis 1997). This cyclicity of water availability leads to alternating cycles of reductive wet phases enabling the mobilization and translocation of Fe and Mn ions and the subsequent oxidation phase when metal precipitation in pore spaces and on primary soil minerals takes place (Liu et al. 2002, Vepraskas and Lindbo 2012, Yu et al. 2015). Alongside water availability, nodule formation is controlled by temperature, soil composition, groundwater chemistry, redox potential (Eh) and pH (Negra et al. 2005, Cornu et al. 2009, Szymański and Skiba 2013, Yu et al. 2015).

As nodule formation process and the resulting shape, size, structure and chemical composition may reflect pedogenic history, soil composition and pedoenvironmental conditions (Zhang and Karathanasis 1997, Szymański et al. 2014, Yu et al. 2015), the nodules hold the potential to be useful in the study of elemental geochemistry, pedogenic processes and environmental changes. However, even though pedogenic Fe-Mn nodules are representative of soil redox history (White and Dixon 1996) and presumably contain

an abundance of soil environmental history. So far, the results have largely defied wider interpretation. Recently, limited progress has been made in developing a nodule formation model that has been applied in reconstructing the redox history of a single nodule horizon (Yu et al. 2020). A ferromanganese nodule-based proxy for paleoprecipiation has also been suggested by Stilles et al. (2001) where the total Fe content of the nodule could possibly be used to solve the mean annual rainfall during time of nodule formation. This proxy, however, remains untested outside of original study.

The aim of this study is to use two variations of scanning electron microscopy to describe the composition and elemental distribution of Fe-Mn nodules formed during the Late Miocene and the Pliocene from three different soil horizons near Lantian county at the southern Chinese Loess Plateau (CLP). The observations will be used to determine if the Fe-Mn from three different time windows can be used to assess the changes in soil redox state and whether the potential changes are indicative of changes in the East Asian monsoon regime as well as evaluate the usefulness of Fe-Mn nodules use as topic of study for paleoclimatological research.

2. GEOLOGICAL BACKGROUND

The Chinese Loess Plateau (CLP) located in northern China between 32–40°N and 98–115°E, covers roughly 600 000 km^2 making it the world's largest and deepest loess deposit (Liu 1999, Fu et al. 2017). The relative stability of the landscape and the long depositional history makes the CLP a terrestrial archive of palaeoclimatological information, containing up to 22 Ma of global and regional climatic history (Guo et al. 2002).

Lantian study area is located in the Lantian county in Shaanxi Province, China. The area is on the southern part of the CLP on the northern foothills of Qinling Mountains and marks the furthest south occurrence of the so called 'Red Clays' (Kaakinen and Lunkka 2003). The Cenozoic sedimentary deposition has taken place in the Weihe Graben basin: a tectonic depression up to 100 km wide spanning some 400 km in the NE to SW direction. The landmasses of the graben were originally part of the upwarding landmasses

of Qinling orogeny that resulted from collisions between North China Craton and South China Blocks during the Triassic (Ratschbacher et al. 2003).

Formation of the graben took place during the Eocene (Liu et al. 2013) due to large scale tectonic movements causing the change of the regional stress regime from compressive to extensional (Zhang et al. 1995 and references therein). This graben, lying on average 400 meters above sea level (Zhang et al. 1995), is bordered by the southern border fault of Mt. Beishan to the north and Huashan-Qinling piedmont fault in the south and is marked by further faulting caused by uneven vertical movements that have led to the formation of distinct fault block mountains and new planation surfaces during Paleogene and Neogene periods (Figure 1, Zhang et al. 1995).

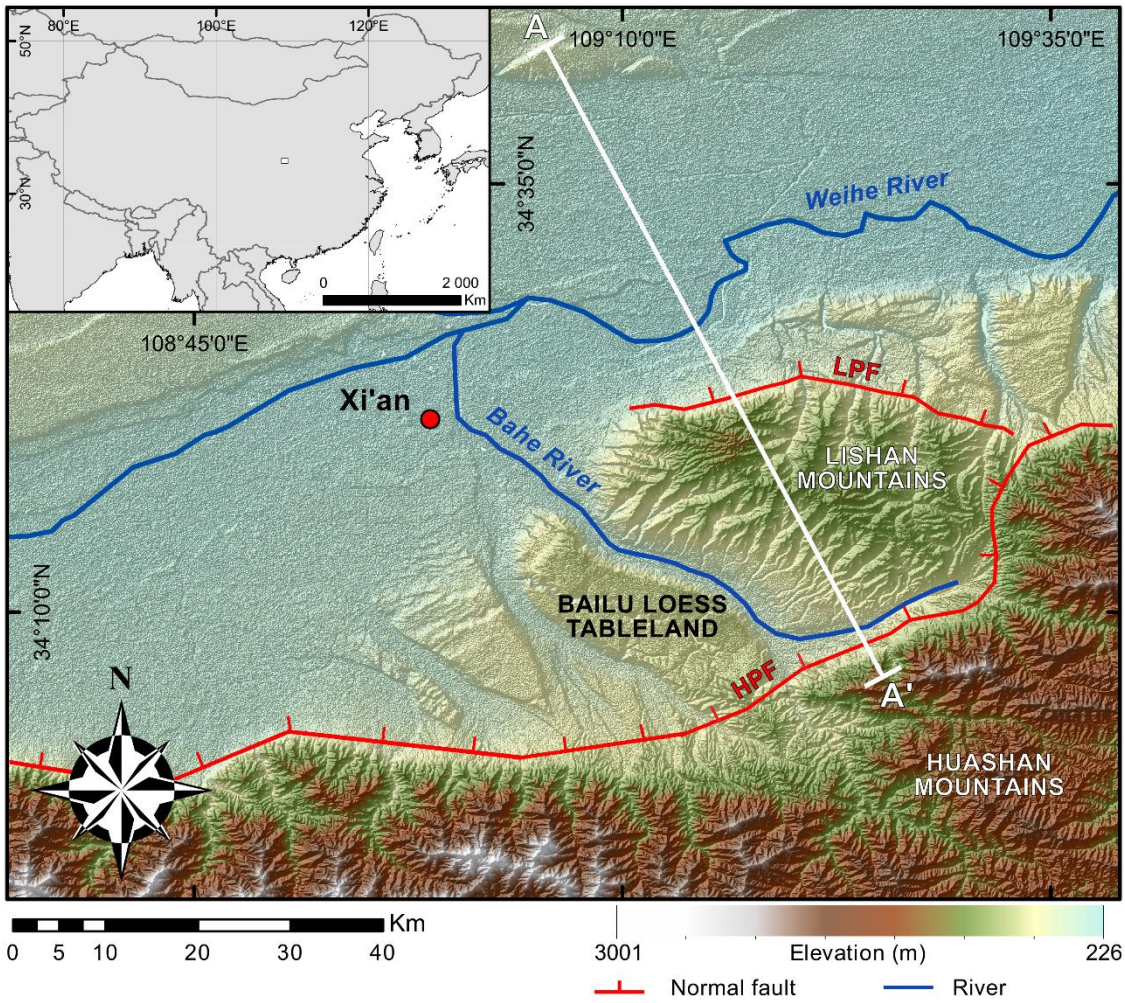

Figure 1. The studied sections in Lantian span across the NW slopes Bailu Loess Tableland. Indicated also are Huashan Piedmont Fault (HPF), Lishan Piedmont Fault (LPF) and Lishan Mountains. Line A, drawn after Rao et al. (2017), marks the location of cross section in Figure 2. Faults drawn after Zhang et al. (1995) and Rao et al. (2017). Digital elevation model from USGS/NASA SRTM data from International Centre for Tropical Agriculture (Jarvis et al. 2008), 1:10 land polygons and city locations from Natural Earth (2018).

On the surface, the Huashan-Qinling piedmont fault also represents a lithological boundary between the upthrown, deeply metamorphosed Archean basement rocks and their Mesozoic granitic intrusions and the downthrown Cenozoic loess tablelands and alluvial fans that have accumulated in the Weihe Graben basin (Figure 2, Du et al. 2017).

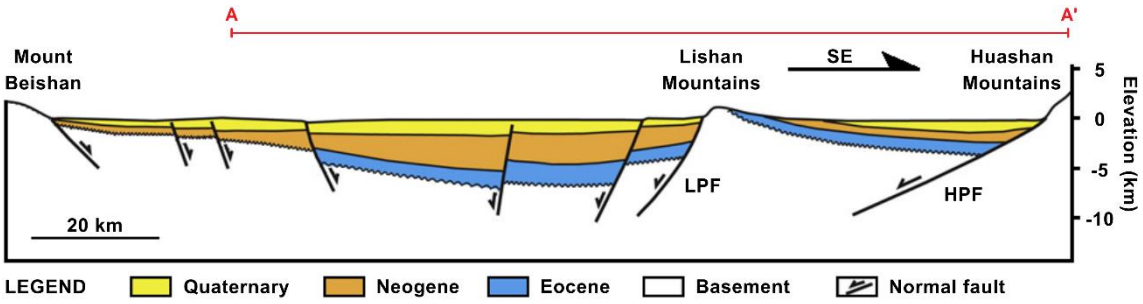

Figure 2. NW-SE cross section of the Weihe Graben showing fault structure and age of deposition for sedimentary strata. LPF stands for Lishan piedmont fault and HPF for Huashan-Qinling piedmont fault. Cross section location marked as A in Figure 1. Edited from Rao et al. (2017).

Study area resides in the SE of Weihe Graben, in a fault block known as the Lishan uplift, some 15 km NW from the N-NW dipping Huashan-Qinling piedmont fault that has general strike direction of roughly 70 degrees in the area. The Lishan uplift block is separated from the low laying Weihe Graben basement by the Lishan piedmont fault to the north and Lingtong-Chang'an fault to the SW (Du et al. 2017). Between the Lishan mountains to the north, Huashan mountains to the NE and Bailu Loess Tableland to the SW, the Bahe river gulley exposes thick sedimentary successions of the north-east facing foot of Bailu Loess Tableland from banks of which the samples of this study were collected. The sedimentary strata in the area gently dip towards the SE from the exposed Lishan mountain basement rocks, along the basement profile towards the exposed Huashan basement rocks (Kaakinen and Lunkka 2003, Rao et al. 2017).

2.1. Stratigraphical framework

The Weihe Graben is infilled with Cenozoic strata (Wang 1987) reaching a maximum thickness of over 6 km (Liu et al. 2013). The sedimentary infill is compartmentalized into distinct lithostratigraphic formations of spatially varying thicknesses (Figure 3, Liu et al. 2013). The following description of sedimentary formations present in Weihe

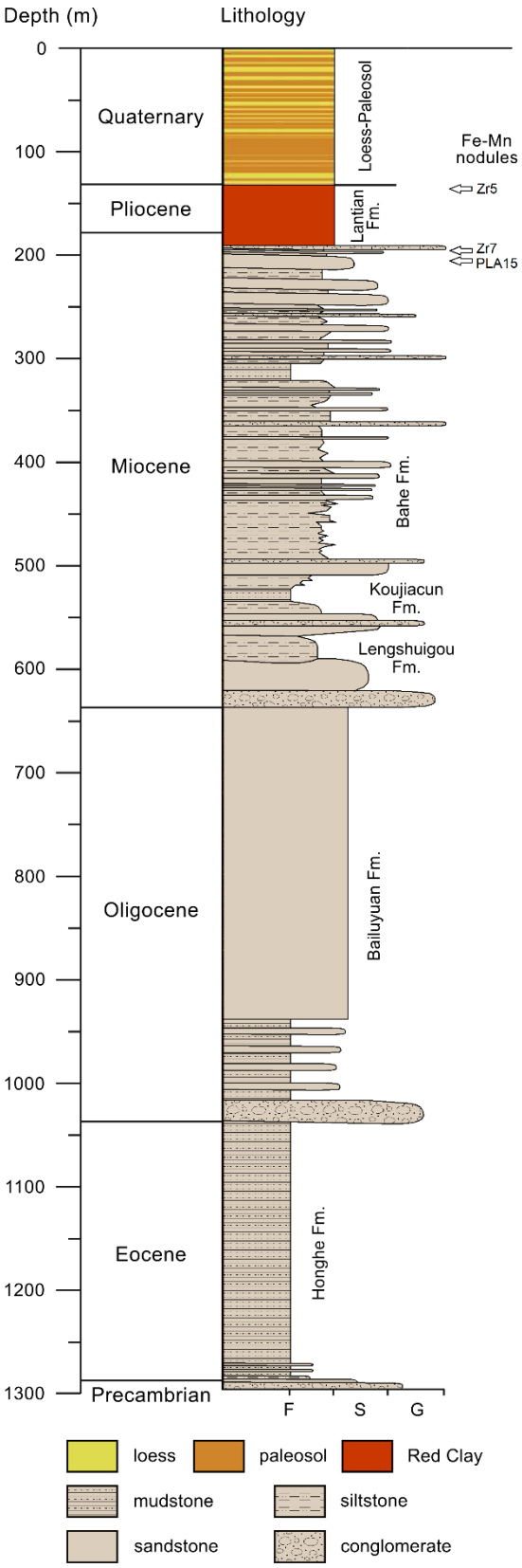

Figure 3. Composite log of the sedimentology in Weihe Graben. Edited from Wang et al. (2014).

Graben are based on Kaakinen and Lunkka (2003) and references therein and Liu et al. (2019).

Older of the two Paleogene formations is the Eocene Honghe Fm, 166–820 meters thick (Liu et al. 2019) strata separated from the Precambrian basement by an angular unconformity (Kaakinen and Lunkka 2003). The base of the strata comprises of thick conglomerate bed that is overlain by layers of sandstones, sandy mudstones and mudstones (Kaakinen and Lunkka 2003). Outcrops of the the Honghe Fm are exposed north of the Bahe river (Kaakinen and Lunkka 2003).

Younger Paleogene unit, the Bailuyuan Fm, deposition took place during late Eocene – early Oligocene (Kaakinen and Lunkka 2003) and the thickness varies between ~43–785 meters (Liu et al. 2019). The formation consists of white sandstones interbedded with brown mudstones which can be observed south of the Bahe river. Between the Bailuyan Fm and the Neogene deposits, a temporal hiatus is present in stratigraphy.

Oldest of the Neogene deposits is the Early – Middle Miocene Lengshuigou Fm, a roughly 80 meters thick formation comprising of sandy conglomerates, sandstones and sandy

mudstones (Liu et al. 2019). These fluviatile rocks are accompanied by several vertebrate fossil that are thought to be of Middle Miocene epoch (Kaakinen and Lunkka 2003).

While the exact lithostratigraphic correlation between Leangshuigou Fm and the younger, 60 meters thick Koujiacun Fm remains obfuscated, the Koujiacun Fm hosts fossils that bear similarities to Middle Miocene fossils of the Tungur locality in Inner Mongolia (Kaakinen and Lunkka 2003). Thus, while there is no direct relationship of these two Formations comprising of similar rock types, Koujiacun Fm is considered to postdate Leangshuigou Fm in published stratigraphy (Liu et al. 2019).

The Bahe Fm is the thickest (~300 m) and youngest of the Miocene formations and has a basal age of ~11 Ma (Kaakinen 2005). The complex formation consists of lower part characterized by reddish brown mudstones and pale sandstones and upper part where reddish and yellow mudstones and sandy mudstones bear interbeds of sandstones and sandy conglomerates (Kaakinen and Lunkka 2003). Through magnetostratigraphic and biostratigraphic correlation, the Late-Miocene age of the Bahe Fm is widely accepted (Zhang et al. 2013, Wang et al. 2014).

Sedimentology and depositional settings of the Bahe Fm are comprehensively described and interpreted in Kaakinen and Lunkka (2003). The sedimentological work was carried out at the north-east facing cliffs of the Bailu tablelands along a 10 km long transect on the southern side of the Bahe River. The sections cover the base of Bahe Fm, which in the area, is some 300 meters thick (Kaakinen and Lunkka 2003).

Kaakinen and Lunkka (2003) identified a total of 13 different lithofacies that mainly associated with fluvial systems. The Bahe Fm is dominated by aggradational deposition of overbank sediments with intermittent coarse-grained channel-fills suggesting an environment where flood plain deposits accumulate outside of a frequently shifting low sinuosity river (Kaakinen and Lunkka, 2003). The flood plain sediments in Bahe Fm are mainly massive, fine grained sediments that display features associated with paleosol formation such as root traces, carbonate nodules and mottling (Kaakinen and Lunkka 2003).

Lacustrine elements are observed as marl beds overlying mudstones that have been interpreted to have precipitated into shallow lakes or ponds (Kaakinen and Lunkka 2003). The thickness of marl beds varies across the sequence, suggesting a system of successive bodies of still water. There is no distinct change in the depositional regime throughout the Bahe Fm, although Kaakinen and Lunkka (2003) note a large-scale trend of upwards fining grain size, which they attribute to tectonic dynamics rather than climatic change. Fe-Mn nodules are found from the topmost flood plain deposits of the sequence. The lower flood plain deposits show film-like and filamentous Fe-Mn agglutinations but lack spherical nodule formation (Kaakinen, personal comm. 2019).

An angular unconformity separates the younger Lantian Fm (6.8–2.6 Ma) from the underlying Bahe Fm (Kaakinen and Lunkka 2003). The base of this ~60 meters thick formation (Liu et al. 2019) is identifiable by a conglomerate bed. The fluvial conglomerate bed is channelized and shows trough-cross stratification interbedded with sandstones (Kaakinen 2005). The lowest 'Red Clay' deposits host and upwards decreasing amounts of thin, massive sand beds and sand lenses whereas the rest of the Lantian Fm comprises of relatively homogenous 'Red Clay' deposits with upwards fining grain size (Kaakinen 2005).

The dominant lithology of the formation comprises of massive silty clay and red brown silt (Kaakinen and Lunkka 2003). This fine-grained lithology is marked by cyclic occurrence of carbonate nodule horizons, a typical feature consistent with 'Red Clay' deposits. Carbonate content in Lantian Fm varies between 10–80 % and remains highly scattered with no discernible trends across the section, apart from a one, up to 2-meter-thick carbonate nodule rich caliche layer at the very top of the Lantian Fm (Kaakinen 2005). Apart from the lowest conglomerate bed, bulk of the Lantian Fm has been deposited from eolian transportation (Guo et al. 2002, Shang et al. 2016.).

The Lantian Fm is overlain by a Quaternary loess-paleosol sequence with basal age 2.6 Ma. It consists of a total of over thirty alternating layers of both loess and red-brown paleosols (Kaakinen 2005).

2.2. Climatological Settings

The current climatological settings of the Lantian can be characterised as semi-humid monsoon climate of warm temperate zone. The Mean Annual Temperature (MAT) in nearby city of Xi'an is 14.8 °C and the Mean Annual Rainfall (MAP) is, on average, 528 mm a^{-1} (AM Online Project 2020). Over the Chinese Loess Plateau, most of the rainfall is the result of humidity transfer from South China Sea by the East Asian Summer Monsoon (EASM), with some overlapping contribution from the Indian monsoon (Figure 4, Wang and Follmer 1997) whereby 68–87 % of rainfall takes place between May and September (Liu et al. 2005). Winter months see little rainfall during the dry winter monsoon. The Lantian area is separated from the subtropical, higher humidity climate in the south by the Qinling mountains. The flora of the Lantian region can be characterized as forest steppe vegetation with broadleaf deciduous forest (Cai et al. 2013) and the Qinling mountains south of Lantian act as a divider, separating the temperate forest steppe vegetation prevalent in the Lantian region from the higher humidity and subtropical forests in the south.

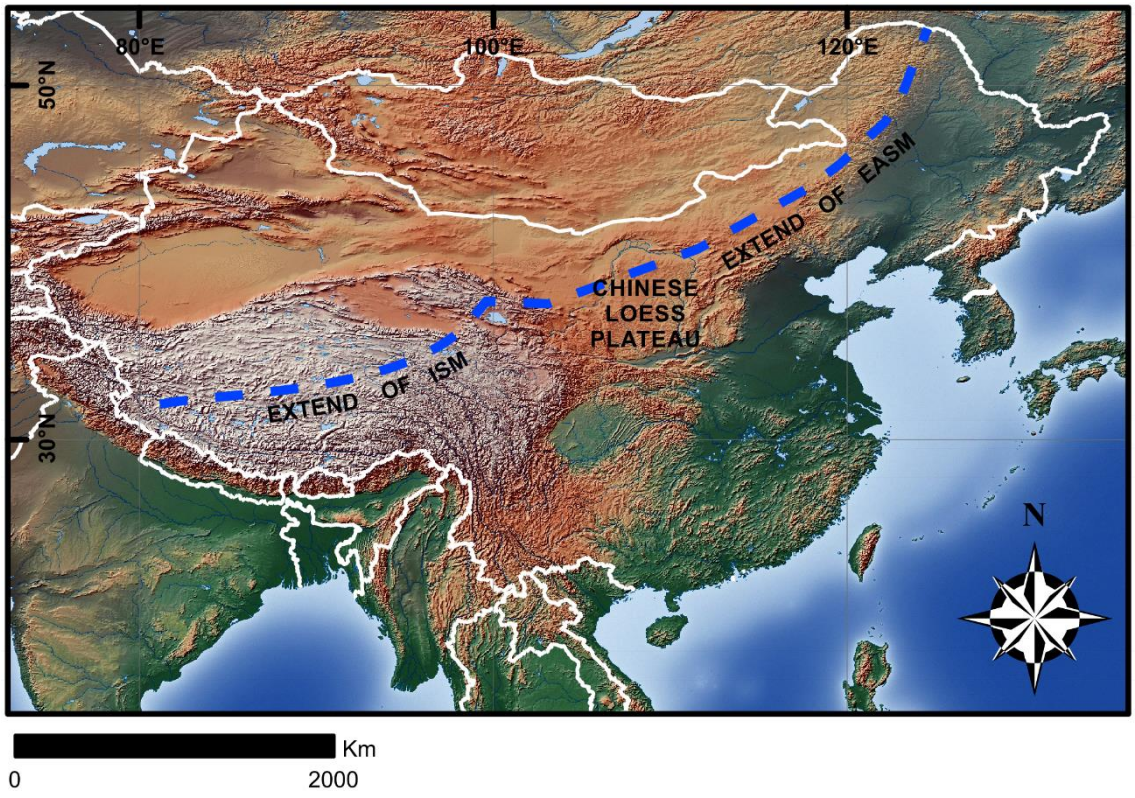

Figure 4. The location of the Chinese Loess Plateau and the current extent of the East Asian Summer Monsoon (EASM) and the Indian Summer Monsoon (ISM) after (Chen et al. 2015). Elevation cross-blended hypsometric tint 1:10 raster and 1:10 country border polygon from Natural Earth (2018).

2.3. Paleoclimatological and paleoenvironmental settings

On a global scale, the Early and Middle Miocene marked an increase in global temperatures after the cool and semi-arid Oligocene (Janis 1993, Zachos et al. 2001). The Early Miocene (23.5–16.5 Ma) saw an increase in global thermal gradients (Wei and Kennet 1986) and first a slight global cooling followed by warming leading to the Middle Miocene Climatic Optimum (MMCO, Zachos et al. 2001). This Miocene temperature maxima was followed by "The Middle Miocene Transition" that marked the beginning of further increase in latitudinal climatic gradients (Flower and Kennet 1994) and a steady trend of global cooling from 13.5 Ma onwards (Zachos et al. 2001). The global cooling trend and expansion of southern ice sheets continued throughout the Late Miocene and accelerated after the Pliocene transition (Figure 5, Zachos et al. 2001). However, while the global climatic trend during Middle and Late Miocene was moving towards lower temperatures and increased mid-latitude aridity (Janis 1993, Liu et al. 2009), the intensification of the East Asian Summer Monsoon (EASM) during Late Miocene (An et al. 2001, Zheng et al. 2004) lead to increased precipitation and humidity in at least some parts of the mid-latitude East Asia (Kaakinen et al. 2006, Passey et al. 2009).

Due to the human dependence on Asian monsoon regime, extensive work has been done to decipher the evolution of the Asian monsoon (An et al. 2001, Sun and Wang 2005, Guo et al. 2008, Clift et al. 2014, Lu and Guo 2014) with the aim of understanding the monsoonal climate variability and predicting future change. However, the conclusions drawn from variable temperature and precipitation proxies from both marine settings and terrestrial sequences in various parts of the CLP are subject to some variance due to the nature of benthic $\delta^{18}O$ stacks used to assess global temperature and the regional variance in terrestrial climatic conditions.

Since Early Miocene, there is evidence of increased heat and humidity dependant chemical weathering and pedogenesis in CLP deposits, however, it is likely to result from elevated temperatures instead of precipitation (Zhao et al. 2020). The effect of EASM likely only reached westernmost parts of the CLP during Late Oligocene – Early Miocene (Guo et al. 2008). During the MMCO (18.5–14 Ma, Zachos et al. 2001). Increased evidence of rising temperatures and precipitation in CLP sediments are interpreted to be the result of the early intensification of the summer monsoon (Clift et al. 2008, Zhao et

al. 2020). Moving towards Late Miocene, the global climate displayed a cooling trend derived from the benthic $\delta^{18}O$ stacks (Zachos et al. 2001). This trend is observed in the CLP as decrease of temperature-controlled weathering (Zhao et al. 2020) and higher soil goethite content typically corresponding to weaker seasonal changes in soil moisture regime (Zhang and Nie 2017) suggesting decreased EASM intensity during 14–8 Ma (Zhao et al. 2020). This notion is corroborated by pollen observations from the CLP that show assemblage changes reflecting decreased EASM intensity (Jiang and Ding 2008).

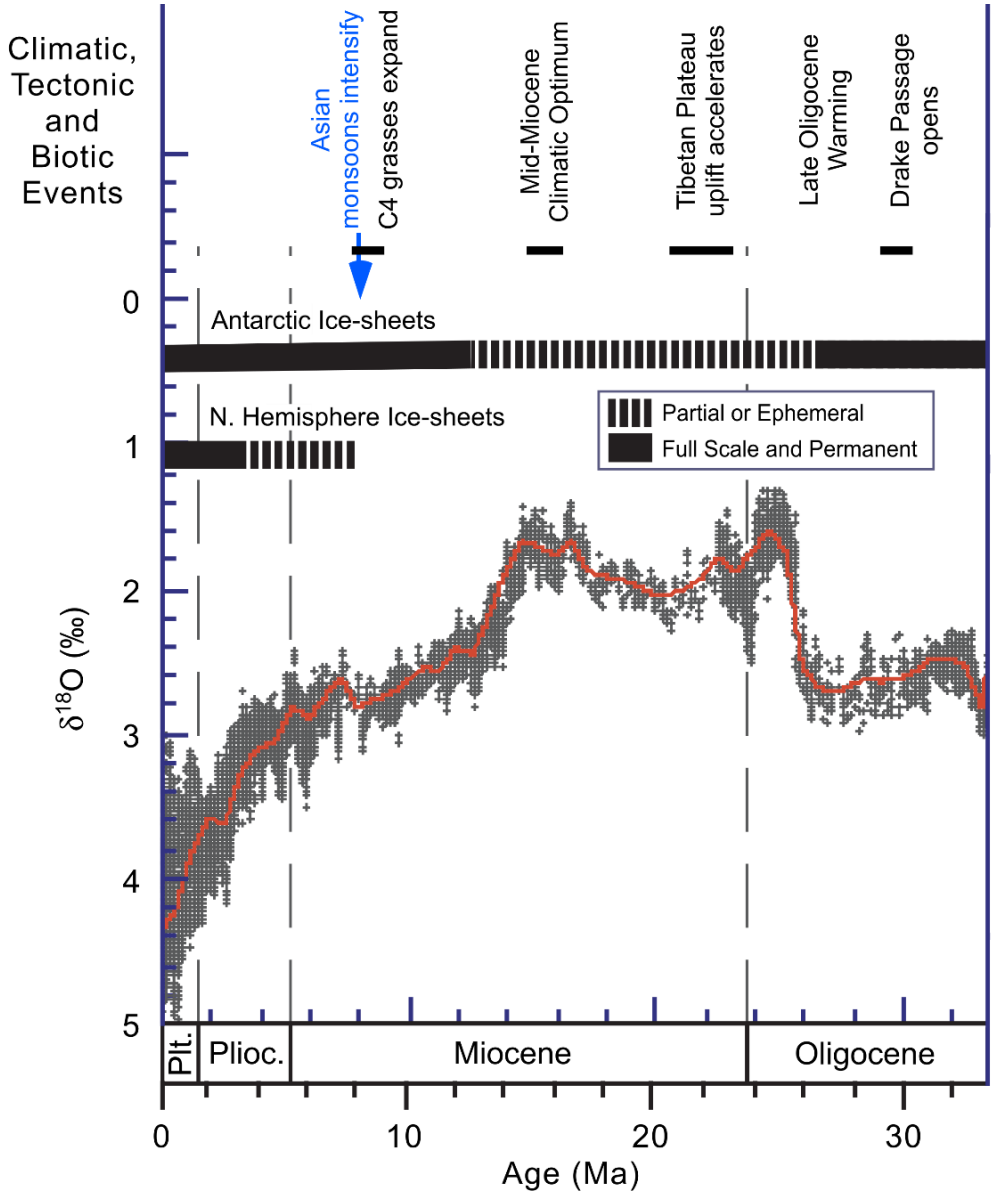

Figure 5. Marine benthic $\delta^{18}O$ stacks reflecting global temperature changes and ice-volume effect. Major climatic, tectonic and biotic events and ice sheet coverage illustrated on a timeline. Edited from Zachos et al. (2001).

After 8 Ma, the gradual strengthening of the monsoon is noted in several studies from the South China Sea (Hess and Kuhnt 2005) as well as the CLP (An et al. 2001, Guo et al. 2002) where EASM reached highest intensity during 4.5–2.6 Ma, although some evidence from the South China Sea suggests that the highest EASM intensity period was between 5–3.8 Ma (Gai et al. 2020). Clay mineral assemblages from Chaona section in central CLP display an assemblage shift that is dividable into three intervals where interval I (7.5–6.9 Ma) is relatively cool and dry, interval II (6.9–4.1 Ma) displays stepwise increase in precipitation and oscillation of cool and dry conditions and step III (4.1–2.6 Ma) the highest increase in markers for summer monsoon intensity (Wang et al. 2019). Likewise, the progressive increase in iron oxide characteristics indicating precipitation, temperature and pedogenesis reach maxima between 4.5–2.6 Ma (Zhao et al. 2020) which is also reflected in the enhanced chemical precipitation observed in the South China Sea during the same time period (Clift et al. 2008).

After the 2.6 Ma, iron oxide based EASM proxies studied in Southern and South Eastern CLP display a decreasing trend in precipitation, pedogenesis and temperatures after Late Pliocene to the Early Pleistocene strengthening again as the glacial-interglacial cyclicity begins to enhance the monsoon cyclicity at ~1.0 Ma (Zhao et al. 2020). This notion is corroborated by magnetic susceptibility and bulk grain size observations in Pleistocene sediments from Yushan, located some 50 km north of Lantian, that reflect overall arid conditions starting from 2.22 Ma with minor periods of higher humidity (Wu et al. 2018). During Mid-Pleistocene transition, when global climate cyclicity changed from the 41-ka obliquity band to the 100-ka eccentricity dominant cyclicity (Hönisch et al. 2009), the changes in monsoon intensity are present as periods of higher humidity overprinting complex pattern of changes during 0.94–0.86 Ma followed by a humidity maxima during 0.62–0.48 Ma (Wu et al. 2018).

Due to the size and topography of the CLP, the general trends mentioned above do show variation, particularly between the general CLP trends and the intramontane basins in the South-Western CLP where a general cooling trend is observed starting around ~7 Ma ago (Chen et al. 2019). This suggests that the general paleosol redox conditions and amount of meteoric rainfall varies spatially and that different locations and their paleoclimatological and pedogenic settings have to be analysed on a case-by-case basis

and highlights the importance of multiproxy approach, e.g. the inclusion of biological proxies as well as soil isotope geochemistry.

Paleoenvironmental reconstructions can be based on the distribution C_3/C_4 vegetation and how it is reflected proxies such as soil carbonate $\delta^{13}C$ (Kaakinen et al. 2006), mammalian tooth enamel $\delta^{13}C$ (Passey et al. 2009) as well as direct fossil evidence based environmental reconstructions (Zhang et al. 2013).

As the CLP is located in the sphere of influence of the monsoon climate system (Figure 4), changes in the monsoon intensity are reflected heavily on the spatiotemporal distribution of C_3/C_4 vegetation. The distribution of these two photosynthesis pathways is controlled primarily by temperature (Ehleringer et al. 1997), seasonality and aridity (Wang and Follmer 1998, Shen et al. 2018) which all can be used to estimate the intensity and extent of summer monsoon (An et al. 2005, Liu et al. 2005). The changes in pedogenic carbonate (Kaakinen et al. 2006) and fossil tooth (Passey et al., 2009) $\delta^{13}C$ values reflect changes in C_3/C_4 plant distribution (Cerling 1984) due to C_3 plants being more discriminating towards heavier ^{13}C (Deines 1980).

Fossil tooth enamel $\delta^{13}C$ from Late Miocene show a northward increasing trend signalling increased C_4 vegetation coverage towards northern extent of the CLP which is interpreted as sign of vegetation ecosystem change from C_3 plant dominated, evergreen forest settings in the south, towards forest steppe and desert steppe environments in the north (Passey at al. 2009). In Passey et al. (2009) model, during the Miocene-Pliocene (7–4 Ma) the C_3 dominated evergreen forest environments covered the southern CLP where Lantian is located. After 4 Ma, the vegetation zones began shifting southwards with time and C_3/C_4 mixed forest steppe vegetation became dominant in the area since 2 Ma (Passey et al. 2009). This reconstruction would imply relatively higher effective humidity and amount of woody vegetation in the Lantian area during the Miocene–Pliocene transition.

Soil carbonate observations from the Bahe Fm show relatively constant $\delta^{13}C$ values during ~10–6.8 Ma with an average value of -8.7 ± 0.2 ‰ that has been interpreted as an almost pure C_3 vegetation under high water stress (Kaakinen et al., 2006). $\delta^{13}C$ values from the Lantian Fm (~6.8–2.6 Ma) soil carbonates are slightly more dispersed and have an average 9.4 ± 0.5 ‰ across the formation with no significant increase in values before

4.5 Ma and surpassing -8 ‰ at 2.6 Ma (Kaakinen et al. 2006), indicating C_3 dominated vegetation during Lantian Fm deposition.

Relatively abundant vertebrate fossil discoveries from both the Bahe Fm and the lower part the Lantian Fm have been found and used for biota-based reconstructions of the paleoenvironment in the area (Zhang et al. 2013). A very distinct faunal turnover is observed at the Bahe Fm - Lantian Fm turnover, although the lack of fossil discoveries from the top part of Bahe Fm prevents precise dating of the observed change (Zhang et al. 2013). The fossils of Bahe Fm reflect open conditions with presence, among others, of equids, rhinocerotids, giraffids and bovids associated with open, plain like environments (Zhang et al. 2013). After the turnover from Bahe Fm to Lantian Fm, the faunal assemblages reflect much more closed, forested environments that can be observed as the increased presence of suids, small giraffids and cervids (Zhang et al. 2013).

All in all, the sedimentological, geochemical and fossil-based evidence suggest a relatively stable, semi-arid and open flood plain environment during the formation of Bahe Fm that is succeeded by increased forest coverage and closing of the paleoenvironments. The change is likely due to increased precipitation caused by the intensification of the summer monsoon circulation (An et al. 2001). This development is generally an exception from the global trend of increased aridity and reduced temperatures (Janis 1993).

3. FE-MN NODULES AND CONCRETIONS

The geochemical study of soil ferromanganese elements began during the 1970's (Childs 1975) and started to make strides towards the turn of the millennium (Ram et al. 2001, Aide 2005). Early study of Fe-Mn nodules and morphology focused using electron microscopy was limited largely to qualitative analysis of element distribution and interpretations made on high magnification imaging (Pawluk and Dumanski 1973), but as scanning electron microscopy (SEM) became a more prevalent method, semi-quantitative and quantitative elemental analysis and analysis of elemental distribution became possible (White and Dixon 1996, Palumbo et al. 2001, Liu et al. 2002, Cornu et al. 2005).

Mineralogical study of Fe-Mn nodules has long been troublesome due to the minerals being very poorly crystalline or completely X-ray amorphous, significantly hindering the use of X-ray diffraction (XRD) for mineral identification (Childs 1975). The primary mineral grains commonly acting as nodule nuclei have been identified to be quartz, feldspars or micas (Manceau et al. 2003). The main ferric oxides, oxyhydroxides and hydroxides (hereafter all referred to as oxides for brevity) have been shown to be goethite, haematite and ferrihydrite with variable amounts of Al substitutions (Liu et al. 2002, Cornu et al. 2005). Mn oxide identification has proved even more challenging, but XRD methods and selective dissolution methods (Tokashiki et al. 2003) have been successfully combined to identify minerals like vernadite and lithiophorite (Liu et al. 2002, Vidhana Arachchi et al. 2004).

Mineral analysis of Fe-Mn nodules truly became viable with the advent of modern synchrotron-based methods, such as X-ray absorption near edge structure spectroscopy (D'Amore et al. 2005), extended X-ray absorption fine structure spectroscopy (D'Amore et al. 2005, Vodyanitskii 2006) and synchrotron based microdiffraction (μXRD) and micro X-ray fluorescence (μXRF), have revolutionized the study of both elemental and trace element chemistry as well as Fe-Mn mineral content (Vodyanitskii 2006). Likewise, modern micro-Raman spectrometers have been successfully used for mineral identification in poorly crystalline Fe-Mn nodules from marine settings (Ostrooumov 2017), making the method promising for study of pedogenic nodule mineralogy. Synchrotron X-ray microscopy has been used to accurately map the speciation of elements and mineral content in several nodules of different origin as well as to identify minerals such as feroxyhyte, a type of ferrihydrite, as well as several Mn minerals such as scarce amounts of birnessite (Vodyanitskii 2006).

The study of the three-dimensional structure of Fe-Mn nodules begun in late 20th century but was initially limited largely to nodules of marine origin (Duliu et al. 1997). As standard computer tomography (CT) is mostly useful as qualitative imaging-based assessment of structure homogeneity, attempts to see the mineralogical and elemental distribution in three dimensional settings involved slicing of very brittle nodule material into thin sections and then reconstructing the results. The advent of synchrotron-based X-ray micro-computed tomography (SR-μCT) allowed the accurate mapping of nodule pore networks and elemental distribution of Fe-Mn nodules (Yu et al. 2015).

3.1. Formation of Fe-Mn Nodules and Concretions

There is no singular theory of formation for pedogenic Fe-Mn nodules, but several theories have been proposed (Tebo et al. 2004, Jien et al. 2010, Timofeeva et al. 2014, Zhang et al. 2014, Yu et al. 2015, Sipos et al. 2016, Ettler et al. 2017). The formation can be mediated by microbial activity (Tebo et al. 2004, Timofeeva et al. 2014) or through abiotic redox reactions over alternating wet-dry cycles. All suggested abiotic theories adhere to a shared pathway of early nodule formation where soil Fe-Mn nodules are formed by processes of reduction, translocation and oxidation of Fe and Mn oxides (Vepraskas and Lindbo 2012). During wet phases, soils are mainly reductive environments where the mobility of soil Fe and Mn is enhanced primarily as Fe(II) and Mn(II) ions (Schwertmann and Taylor 1989). During dry periods the soil environment becomes more oxidized, leading to reprecipitation of Fe(II) and Mn(II) in soil pores and on the surface of primary soil minerals such as quartz, feldspars or micas as poorly crystalline oxides (Golden et al. 1988, Yu et al. 2015). This cementation results in creation of a "proto-nodule" which is a discreet, low-porosity, compact nodule of reducible material (Huang et al. 2008). There is also evidence from one nodule bearing horizon, where the microfractures of weathering biotite are filled with amorphous Fe-Mn oxyhydroxides thus eventually forming the proto-nodule out of weathering biotite (Šegvić et al. 2018). The kinetic resistance to reducibility in the proto-nodule make the nodules act as a nuclei of high redox potential that grows as new Fe(II) and Mn(II) ions precipitate on the surface of the nodule (Yu et al. 2015).

As Fe reduction and mobilization takes place at lower Eh values compared to Mn, Mn may remain mobile in environments where Fe is not readily reduced (White and Dixon 1996, Frohne et al. 2011, Yu et al. 2015). Due to the high mobility and oxidation potential requirement for Mn precipitation, it can relocate and precipitate into cracks and pores within the nodule where more oxidizing conditions prevail (Yu et al. 2015). The often thermodynamically unstable Mn oxides are initially precipitated on primary minerals, followed by precipitation in micropores and succeeded by precipitation of Fe oxides on the surface (Yu et al. 2015). While these abiotic processes of wet-dry cyclicity dominate the formation of Fe-Mn nodules, pore filling is essentially an entropy reducing process requiring additional energy, making it likely that the extra energy required is derived from microbial activity (Yu et al. 2020). As the soil environment goes through alternating

reductive and oxidizing conditions, eventually multiple concentric Mn-Fe rings grow on the initial proto-nodule forming a structure of concentric Fe or Mn oxide rings.

During times of relative higher water availability, the hydrous Mn and Fe phases (birnessite and ferrihydrate, respectively) form in micropores within the soil. As lack of water starts to limit the hydrous phases, the formation of minerals proceeds towards more stable lattices like hollandite and goethite (Schwertmann and Taylor 1989, Gasparatos 2012). However, in actual samples birnessite is a relatively rare mineral only present as thin coatings while lithiophorite and vernadite are the dominant Mn bearing minerals (Vodyanitskii 2006), which may be due to the relative scarcity of Mn(III) and Mn(IV) cations. Still, mineral content reflects theory as most unstable minerals such as ferric ferrihydrite proper and feroxyhyte and manganates vernadite and birnessite are concentrated near the nucleus of the nodule, whereas the outer envelope consists of mostly relatively stable goethite and hollandite (Vodyanitskii 2006). It is to be noted, however, that synchrotron radiation-based methods have been applied to a very limited number of samples from few regions, so variability of the minerals present could alter to some degree depending on the pedogenic environment.

It is also noted that oxidation of Fe(II) can be considerably accelerated by the presence of Mn(IV) ions (McKenzie 1989) in a situation where manganese oxides that contain Mn(IV) precipitate initially, the oxidation of Mn(IV) and Fe(II) can cause the precipitation of the Fe(III) phase (Schwertmann and Taylor 1989). In this case and under certain Eh-pH conditions, the presence of birnessite may promote the crystallization of Fe ions forming mainly goethite (α-FeOOH) and lepidocrocite (γ-FeOOH) along the expected ferrihydrite (Krishnamurti and Huang 1989).

Very few peer reviewed quantitative studies of nodule formation duration exist, and the timeframes are very much estimated as Fe-Mn nodules are typically beyond U-Th-Pb- and ^{14}C dating. Likely, depending on the environment, the process of forming a mature, ring structured nodule could last from few thousand years (Stiles et al. 2001) to tens of thousands of years (Yu et al. 2020). In one case a modern forest soil Fe-Mn nodule revealed that the organic carbon trapped within the nodule had a ^{14}C age of more than 21 000 years (Elberling et al. 2013).

The formation rate is mainly controlled by rate of changes in the soil redox conditions where slower changes increase Fe and Mn enrichment (Yu et al. 2020). Fe-Mn nodule porosity can be used to assess the nodule formation as during periods of slow changes in redox settings, more metals can precipitate within the soil pore network resulting in lesser porosity within the nodules (Yu et al. 2020). This implies that during faster changes of soil redox state, the Fe-Mn nodule pores could be partially blocked by the quicker precipitation of Fe-Mn minerals, resulting in smaller Fe-Mn enrichment. Due to the process of nodule formation and the slow rate of growth, nodules found from same soil horizon can then be in different stages of formation and display considerable differences in shape, enrichment and in structure or lack thereof.

Fe-Mn nodules are known from various types of pedoenvironments such as alfisols, fluvisols, ultisols, gleysols, planosols and stagnosols (IUSS WG WRB 2015) as well as several types of undefined paleosols. To facilitate the formation of redoximorphic features, requiring dissolution, translocation and oxidation of redox sensitive elements, several criteria must be simultaneously fulfilled (Blume et al. 2016): 1) decomposable organic substrate has to be present, 2) temperature and environment has to be suitable to support microflora activity, 3) soil must be water saturated 4) oxygen must be restricted enough to form anaerobic conditions 5) alternative electron acceptors must be present and 6) anaerobic conditions have to be followed by subsequent aeration.

Sipos et al. (2016) studied the effects of soil settings in nodule formation by the changes in nodule microfabric and the elemental distribution. The results of Sipos et al. (2016) indicate that the length and frequency of waterlogging to affect the cementation of primary soil minerals, re-arrangement of elements and the rate of impregnation of nodules' interior, where fast impregnation was often combined with exfoliation of the outer coating band. Likewise, an increase in rate of hydromorphism resulted in the dominance of Mn oxides to turning to dominance of Fe oxides (Sipos et al. 2016). However, this was not seen to be the case in all parts of the nodules, implying that the process is affected by numerous factors, such as the supply of Fe and Mn, rate of ion diffusion towards nodule interior and the resistance of nodule phase associations (Sipos et al. 2016). The relations between nodule microfabric, distribution of chemical components and the host soil are largely unexplored on wider scale and under more contrasting soil settings.

3.2. Elemental Chemistry

Main elements in Fe-Mn nodules are Si, Al, Fe and Mn and minor element constituents are Ba, Ca, Mg, K, Na, Ti, Pb and Co (Liu et al. 2002). EDS-SEM detectable amounts of Cd, Cr, Cu, Ni, V, Zn and Zr are also relatively common (Liu et al. 2002, Yu and Lu 2016). Element concentration compared to surrounding soil is calculated as enrichment factor (EF). These EF values display that ferromanganese nodules are highly Mn enriched, 25–60 times the concentration of host soil (Table 1, Childs 1975 Palumbo et al. 2001, Liu et al. 2002), and to lesser extent, Fe with EF decreasing to around 2–5 in larger nodules (Palumbo et al. 2001, Cornu et al. 2005). Simultaneously, nodules are usually depleted in most common alkaline earth metals such as Ca and Mg in regard to the host soil (Gasparatos 2012).

Table 1. Fe-Mn nodule enrichment factors (EF) reported in previous studies.

	EF_{Si}	EF_{Al}	EF_{Mn}	EF_{Fe}	EF_{Ca}	EF_{Mg}	EF_{K}
Tan et al. (2006)	0.70	0.78	57.8	2.11	2.29	0.66	0.66
Palumbo et al. (2001)		0.95	30.7	2.34	0.14	0.56	0.78
Childs (1975)	0.72	0.83	25.7	3.5	0.71	-	0.89

Carbon in Fe-Mn nodules is associated with Mn oxides with the C content increasing alongside Mn concentration (Tebo et al. 2004). Fe-Mn nodules can be highly carbon enriched with an EF of 10–20 (Rennert et al. 2014). The carbon is mainly derived from microbial activity (Tebo et al. 2004) and derives mostly of lipopolysaccharides and extracellular proteins (Estes et al. 2017).

The capacity of Fe-Mn nodules to absorb metals is well documented (McKenzie 1989) and is of particular interest in the study of the toxic heavy metal sequestration capabilities of soil Fe-Mn nodules (Gasparatos 2012). The generally large absorption capacity and scavenging potential of Mn oxides means that they function as one of the primary controls of metal ion availability in soils (Gasparatos 2012). Mn oxides are particularly effective heavy metal scavengers as their surface becomes negatively charged as soil pH increases, allowing the trapping of heavy metals as the nodules are formed (Liu et al. 2002). The metal ion affinities on the surface of Mn oxides can be generally described in a decreasing order as follows: Pb > Cu > Mn > Co > Zn > Ni (McKenzie 1980). This has been observed

to be a working estimate, although not universally applicable (Liu et al. 2002, Timofeeva et al. 2014). Contradicting reports of Pb association exist, as in some nodules Pb has been reported to be strongly associated with Mn phases of the Fe-Mn nodules (Liu et al. 2002, Cornu et al. 2005, Timofeeva et al. 2014), but there is also evidence of Pb sequestration with Fe phases (Palumbo et al. 2001, Aide 2005, Yu and Lu 2016). Similar discrepancy exists with Co, as Palumbo et al. (2001) discovered no association towards either oxide phases, whereas Neaman et al. (2008) observed Co to be associated with Mn oxides in nodules.

The most significant Fe associated heavy metal is Cr as ferromanganese nodules are possibly the most important scavengers of Cr(III) via Fe isomorphic substitutions (Tzou et al. 2003). Also, in Chinese alfisols, the nodule Fe content displays a linear correlation with not just Cr, but other heavy metals such As, Mo and Se (Manceau et al. 2002, Aide 2005). It is then reasonable to say that he knowledge on spatial distributions and dynamics of heavy metals in Fe-Mn nodules, while making strides in the recent years, is still lacking as different correlations have been observed from nodules collected from various soils (Gasparatos 2012, Yu and Lu 2016).

4. SAMPLES AND METHODS

PLA15 series of samples originate from upper Bahe Fm, henceforth referred to with a working title “upper Bahe Fm”, from strata that is known as fossil locality 6 (Zhang et al. 2013) and have been dated to 8.07 Ma (Zhang et al. 2013, Kaakinen, personal comm. 2020). The nodules were collected from floodplain siltstone (Kaakinen, personal comm. 2020). The red-brown siltstone is massive and bears an abundance of very large, dark brown nodules typically ranging between 3–5.5 mm in size. Floodplain deposits in the lower parts of the Bahe Fm show no spherical Fe-Mn nodules, only filamentous and film-like Fe-Mn agglutinations (Kaakinen, personal comm. 2020). No paleosol analysis has been done for upper Bahe Fm paleosols. The soil environment features indicate waterlogging with possible periodic oxygen depletion. The rate of sediment deposition in Bahe Fm varies between 4–6 cm ka^{-1} (Kaakinen 2005, Zhang et al. 2013).

The samples were removed from a roughly 3 dm^3 block of consolidated sediment matrix in University of Helsinki using dental tools. Block of this size contained several hundreds of Fe-Mn nodules. A total of 11 samples from upper Bahe Fm were selected for analysis.

Zr7 samples originate from a horizon on top of the Bahe Fm that is henceforth referred to under the working title of "topmost Bahe Fm." The site is dated to 7.7 Ma and referred to as fossil locality 52 in Kaakinen and Lunkka (2003) and Zhang et al. (2013). Unlike most of Bahe Fm, the topmost Bahe Fm deposits show a clear eolian component largely resembling the 'Red Clays' present in overlaying Lantian Fm (Kaakinen, personal comm. 2020). However, unlike most of Lantian Fm, the topmost Bahe Fm strata shows thin, laterally continuous sandy beds indicating fluvial activity. The Fe-Mn-nodule-bearing silty claystones showed to contain carbonates upon hydrochloric acid reaction test (Kaakinen, personal comm. 2020). The primary sediment structures have been destroyed by pedogenic processes, but signs of roots are present as green striping. The nodules from topmost Bahe Fm are all of smaller size (~1–2 mm), reddish or dark brown and the sample quantity is limited. All samples, seven of which were chosen for analysis, have been separated from soil matrix on site upon collection.

Zr5 samples originate from the top of the Lantian Fm with a depositional age of 3.7 Ma (Kaakinen, personal comm. 2020) from a horizon henceforth referred to with a working title "Lantian Fm." The Fe-Mn-nodule-bearing horizon of silty claystone is located right under a up to two-meter-thick caliche horizon formed over a very long time span, indicative of high precipitation and subsequent evaporation. The Fe-Mn nodule location in relation to the gradational basal contact of the carbonate nodules varies between immediate contact and 50 cm (Kaakinen, personal comm. 2020). Lantian Fm deposition is considerably slow, with calculated sedimentation rate of 1.38 cm ka^{-1} (Kaakinen 2005, Zhang et al.2013).

Most Zr5 have been separated from sediment matrix on site. Samples 8–11 of the series have been collected on a later date and separated from the matrix at the University of Helsinki. The samples are primarily of smaller size (1.5–2 mm) but larger nodules up to 5 mm are present in small quantity. The smaller samples appear reddish brown whereas the larger nodules are darker shade of brown. Nodule content per sediment volume is considerably lower than in the sediment block from upper Bahe Fm.

4.1. Sample preparation

For SEM analysis, samples were to be measured from the equatorial plane of the spherical nodule. A variable height sample mount was prepared out of molding putty and nodules of different sizes were aligned horizontally by their largest diameter point. The mounted samples were placed in an outer mold and cast in epoxy resin. After curing, half of the samples, specified with suffix H in sample names, were prepared as 30 μm thick thin sections and the rest of the samples were prepared into half dome shaped thick sections marked with a sample ID suffix D. Thin sections were prepared to have some samples with potential for mineralogical studies using μ-XRD method. A total of 29 nodules samples were prepared, of which 13 as thin sections and 16 as thick sections.

Thin section samples were planed from both sides until the largest diameter 30 μm thick section was left, which was attached to a glass slide using epoxy glue. Thick section samples were planed from one side only until the specified equatorial plane was reached with the resin matrix acting as a sample holder. The epoxy casting and sample cutting was done in the University of Helsinki thin section laboratory.

Before SEM measurements, samples were carbon coated at the Geological Survey of Finland laboratories to prevent overcharges under electron beam in non-conductive materials that could inhibit image formation and deteriorate the samples. In a coating chamber, a carbon rod is sealed in a vacuum between two electrical high-current terminals and heated to the carbon evaporation temperature. The resulting stream of very fine carbon was deposited on top of the samples over 15 minutes.

4.2. FE-SEM and EDS-SEM

Scanning electron microscopy combined with energy dispersive X-ray spectrometry (EDS-SEM) is a commonly used and widely applied technique for elemental microanalysis. Electron microscopy is method where the surface of the sample is scanned with a focused beam of high-energy electrons. The electron beams produce different interactions with the atoms of the target sample. Inelastic and elastic scattering produce

signals that can be used for image formation as well as quantitative and semi-quantitative elemental analysis.

Imaging is typically based on secondary electrons emitted by the target atoms upon excitation with the electron beam and detected with a secondary electron detector. Elemental analysis most commonly utilize characteristic X-rays that are emitted as high energy incident electrons eject electrons from the inner shell of the target atom and the vacancy is filled by an electron from the outer shell. Due to the unique atomic structure of each element, the difference in energy between inner and outer shells may release as an X-ray of specific energy that can be measured using X-ray Energy-Dispersive spectroscopy (EDS). The sample analysis was done using Energy Dispersive X-ray Scanning Electron Microscopy (EDS-SEM) equipment of Geological Survey of Finland Mineral Processing Laboratory in Espoo, Finland.

Elemental mapping was done using the JEOL JSM-7100F FE-SEM combined with Oxford Instruments X-Max EDS operating under Oxford Instruments proprietary Aztec software. The electron beam was run at 20 kV accelerating voltage and 1 nA probe current in high vacuum and COMPO-backscattered signal. Aztec software was used to compile, depending on nodule size, 33–80 semi-quantitative element distribution images into a montage image containing the distribution of elements of interest in the nodule. Likewise using the Aztec software, the total elemental composition of the exposed equatorial plane of the spherical nodule was calculated to a semi-quantitative standard. EDS energy calibration was done six times in total: prior to measurements and after every four consecutive hours of use.

Elemental spot analysis was carried out with JEOL JSM-5900LV SEM with Oxford Instruments X-Sight EDS detector. Accelerating voltage of the electron beam was set to 15 kV and probe current to 1 nA. Analyzed spots were chosen along the radius of the nodule to cover major phases visible in the SEM imaging. Process and data acquisition were controlled by Oxford Instruments proprietary Inca software that delivers elemental data of semi-quantitative quality. EDS energy calibration was done prior to measurements.

All measurements were done using the carbon sample coat preselection in Aztec and Inca software, with minimum count number of 300 000 and 20-seconds live time. Results were normalized to 100 with elemental automatic identification threshold set to 2x σ.

5. RESULTS

5.1. FE-SEM

5.1.1. PLA15

Apart from samples 1H and 4H, PLA15 sample series is relatively homogenous in both appearance and elemental distribution (Table 2, Figures 6–7). Nodule shapes vary from spherical to sub-angular. On most samples, the structural anisotropy is higher in less spherical samples.

Table 2. FE-SEM total surface concentrations of PLA15 samples as wt-%

	1H	**2H**	**3H**	**4H**	**5D**	**6D**	**7D**	**8D**	**9D**	**10D**	**11D**
O	44.7	44.2	45.1	44.7	44.9	45.7	44.6	43.1	45.0	43.7	42.3
Si	20.4	19.8	20.7	17.4	19.9	19.1	21,9	19.8	19.2	20.1	20.0
Mn	9.9	10.3	9.9	11.8	10.8	10.6	8.7	12.9	10.5	12.0	12.2
Fe	12.6	8.5	8.4	11.4	9.4	8.1	9.0	8.8	8.8	10.3	9.8
Al	5.1	-	6.6	6.0	5.9	6.4	6.3	6.1	5.8	6.5	6.4
Ba	1.4	2.5	2.3	1.8	2.6	2.7	1.7	3.2	2.5	2.9	3.1
K	1.6	2.0	2.2	1.9	2.0	2.3	2.3	2.1	2.1	2.2	2.2
Cl	1.0	0.7	1.2	1.7	1.5	1.5	1.4	1.0	2.1	0.8	0.7
Mg	1.0	-	1.4	1.2	1.4	1.5	1.3	1.4	1.3	-	1.4
Ca	1.0	0.8	0.8	1.1	0.8	0.8	0.8	0.8	2.1	0.8	0.8
Ti	0.4	0.4	0.4	0.3	0.4	0.4	0.5	0.4	0.4	0.4	0.4
In	0.2	0.2	0.3	-	0.4	0.3	0.3	0.3	0.3	0.3	0.3
S	-	-	-	0.1	0.2	0.2	-	-	0.1	-	0.1
Na	-	-	0.5	-	-	0.4	0.6	-	-	-	-
P	-	-	-	-	-	-	-	-	0.7	-	-
Mo	0.3	-	-	-	-	-	0.4	-	-	-	-
V	0.2	-	-	0.1	-	-	-	-	-	-	-
Pb	-	-	-	0.4	-	-	-	-	-	-	-
Br	-	10.6	-	-	-	-	-	-	-	-	-

A well-developed concentric ring structure with alternating Fe and Mn rich phases is present in most samples with structure becoming more pronounced with increase of nodule size. Smaller samples (6D, 7D and 9D) show less developed internal structure but are not significantly less enriched in Fe and Mn (Table 2). Samples 1H and 4H lack unbroken ring structure and have a mottled appearance. Primary soil fragments are observable as grey crystals under SEM imaging. Samples 3H and 4H show considerable degradation that took place during sample preparation and transport.

Nodule interior and the outer coating is typically Mn enriched (Figures 6–7) and most samples contain higher mass fraction of Mn than Fe, with Mn content ranging between 8.7–12.9 wt-% and Fe between 8.1–12.6 wt-% (Table 2).

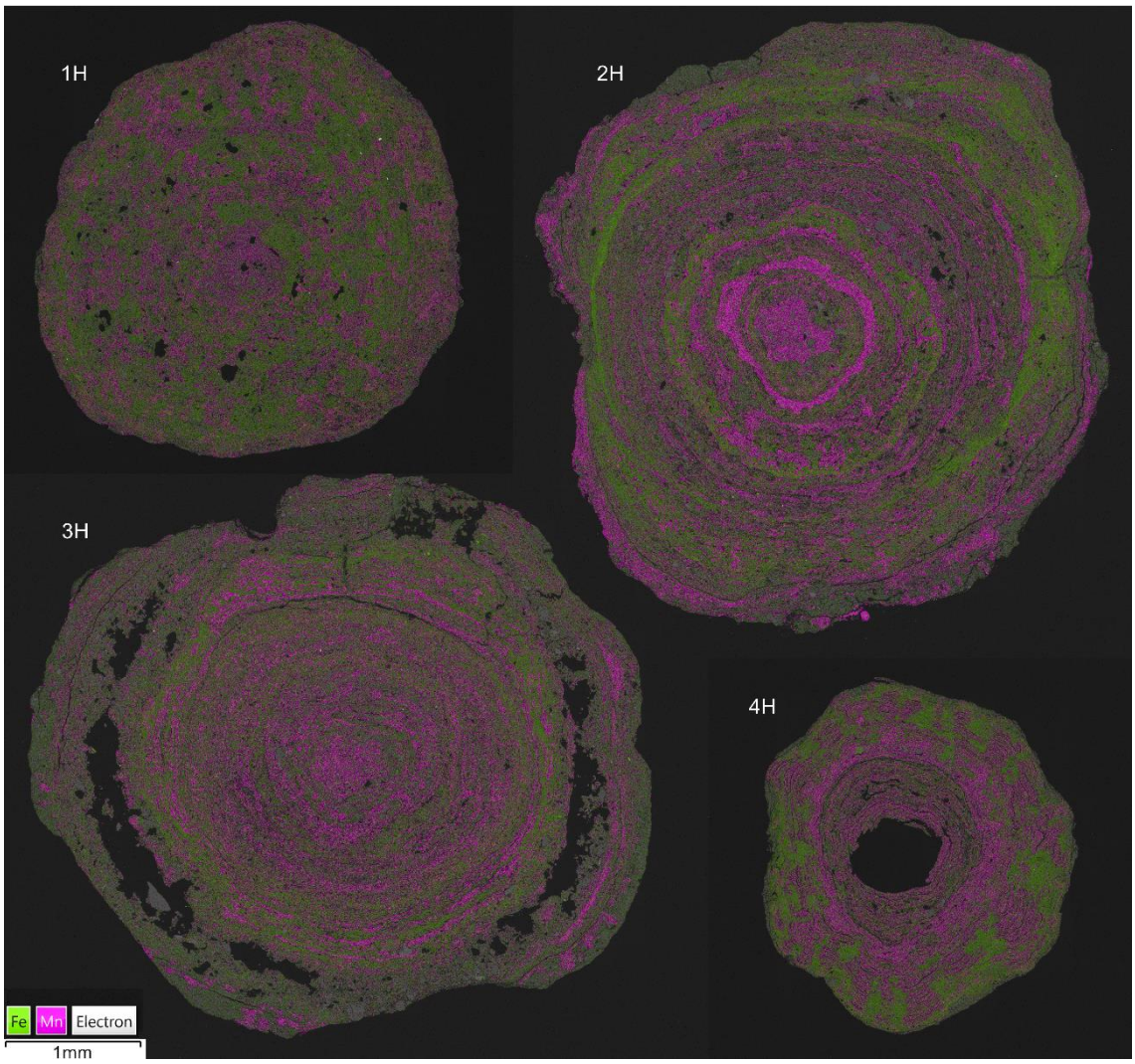

Figure 6. FE-SEM elemental mapping of PLA15 samples prepared as thin sections. Samples 3H and 4H show considerable degradation that has taken place during sample preparation process.

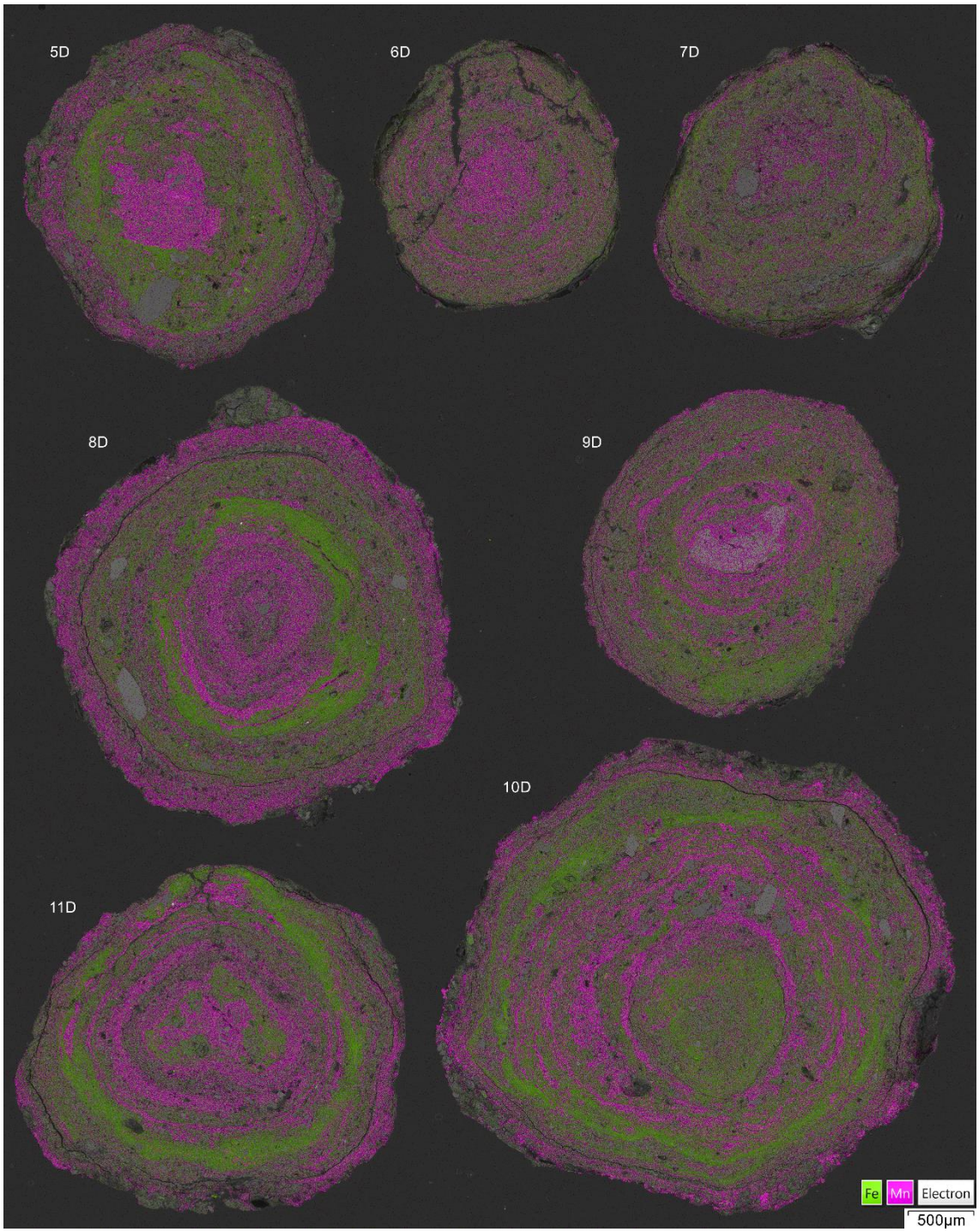

Figure 7. FE-SEM elemental mapping of PLA15 thick section samples.

5.1.2. Zr7

In general, Zr7 series of samples are marked with small size and textural immaturity and low Fe-Mn enrichment (Figure 8). The sample shapes vary between almost spherical and sub-rounded. All but one of the samples in the Zr7 series show poorly developed structure and poor differentiation of Fe and Mn. Faint Mn rings are observable on most samples,

but the Fe distribution remains relatively constant throughout the samples (Figure 8) Sample 2H has a mottled appearance with larger Mn content than other samples. Nodules of this sample series contain a low amount of very small Si and Fe rich primary soil mineral fragments.

The chemical composition is relatively high in Si and most samples are only moderately Fe enriched (6.6–10.4 wt-%) and somewhat poorly Mn enriched (5.6–8.7 wt-%, Table 3).

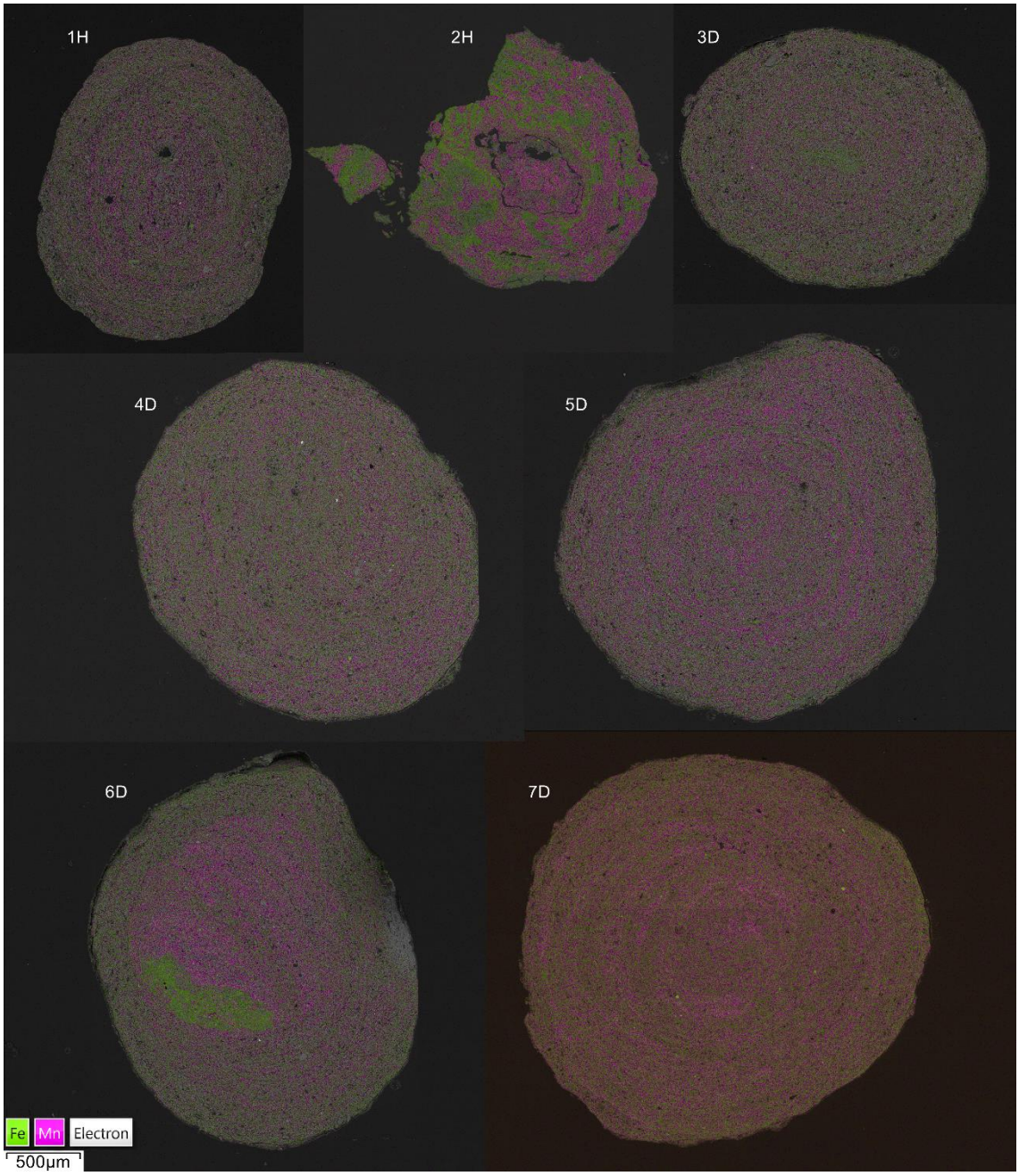

Figure 8. FE-SEM Fe-Mn elemental mapping of Zr7 thin sections (H) and thick sections (D).

Table 3. FE-SEM total surface concentrations of Zr7 samples as wt-%

	1H	2H	3D	4D	5D	6D	7D
O	48.6	47.9	44.2	45.4	44.6	45.1	45.2
Si	23.3	18.1	24.4	24.1	24.0	23.1	23.6
Mn	5.5	8.7	5.6	5.8	7.9	7.0	7.3
Fe	6.1	10.4	8.0	6.9	6.6	7.7	7.4
Al	7.6	5.8	8.7	8.7	7.9	8.0	7.7
Ba	1.0	1.1	1.2	1.2	1.6	1.7	1.5
K	2.8	1.7	3.3	3.2	3.1	2.3	2.9
Cl	1.5	2.2	0.7	0.7	0.6	0.9	0.7
Mg	1.3	1.1	1.6	1.7	1.5	1.5	1.4
Ca	0.6	2.4	0.7	0.7	0.7	1.1	0.7
Ti	0.5	0.4	0.6	0.6	0.6	0.5	0.5
In	0.4	0.2	0.3	0.3	0.3	-	0.3
S	0.1	0.1	0.2	0.1	0.2	-	0.1
Na	0.6	-	0.5	0.5	-	0.5	0.6

5.1.3. Zr5

Sample series is the most heterogenous in size, structure and elemental distribution. Mn content of the samples shows considerable variation and typically decreases with the size of the nodule (1.8–13.6 wt-%) while, apart from sample 8D with an anomalous iron content of 16.1 wt-%, other samples range between 5.7–8.0 wt-% (Table 4).

Table 4. FE-SEM total surface concentrations of Zr5 samples as wt-%

	1H	2H	3H	4H	5H	6H	7H	8D	9D	10D	11D
O	43.6	47.4	49.6	49.0	48.4	48.1	49.7	45.2	44.8	44.2	45.2
Si	19.7	20.7	23.4	23.6	23.6	21.4	25.0	22.3	23.5	24.4	23.8
Mn	13.6	9.0	4.3	4.1	6.4	7.8	2.6	1.8	8.1	5.6	7.7
Fe	7.6	7.2	5.8	6.8	5.7	6.0	6.9	16.1	6.6	8.0	6.5
Al	6.1	6.4	8.2	6.3	7.3	7.4	7.7	7.1	7.8	8.7	7.9
Ba	3.3	2.2	1.2	0.7	1.1	1.8	0.5	0.4	1.6	1.2	1.5
K	2.1	2.3	2.7	2.3	2.7	2.5	2.6	2.5	3.0	3.2	3.0
Cl	0.9	0.7	1.5	1.2	1.3	1.4	1.8	0.6	0.8	0.7	0.6
Mg	1.4	1.4	1.8	1.0	1.3	1.6	-	1.3	1.5	1.6	1.6
Ca	1.0	0.9	0.6	0.7	0.7	0.8	0.7	0.9	0.7	0.7	0.7
Ti	0.4	0.5	0.5	0.4	0.5	0.5	0.5	0.4	0.6	0.6	0.6
In	0.2	0.3	0.4	0.5	0.4	0.3	0.5	0.3	0.4	0.3	0.3
S	-	-	-	-	-	-	-	0.1	0.2	0.2	0.2
Na	-	-	-	0.5	0.6	0.4	1.4	0.6	0.6	0.5	-
P	-	-	-	-	-	-	-	0.3	-	-	-
V	-	-	-	-	-	-	-	0.1	-	-	-

Two samples of larger size (~3.5 mm, 1H and 2H) display distinct and well differentiated ring structures and medium sized samples with less defined structure (~2–3 mm, Figure 9). Smallest samples display faint Fe-Mn differentiation or no structure at all (~1.5–2.5 mm, Figure 10). Samples are almost spherical or sub-rounded. Apart from samples 2H and, to lesser extent, 5H, nodules do not have Mn enriched interior. Many nodules host large Si rich soil mineral fragments as well as some Fe rich fragments. Visually, the large fragments do not affect nodule structure apart from slightly reducing the nodule sphericity. Sample 8D has an anomalously high Fe content with just a few poorly defined Mn rich zones.

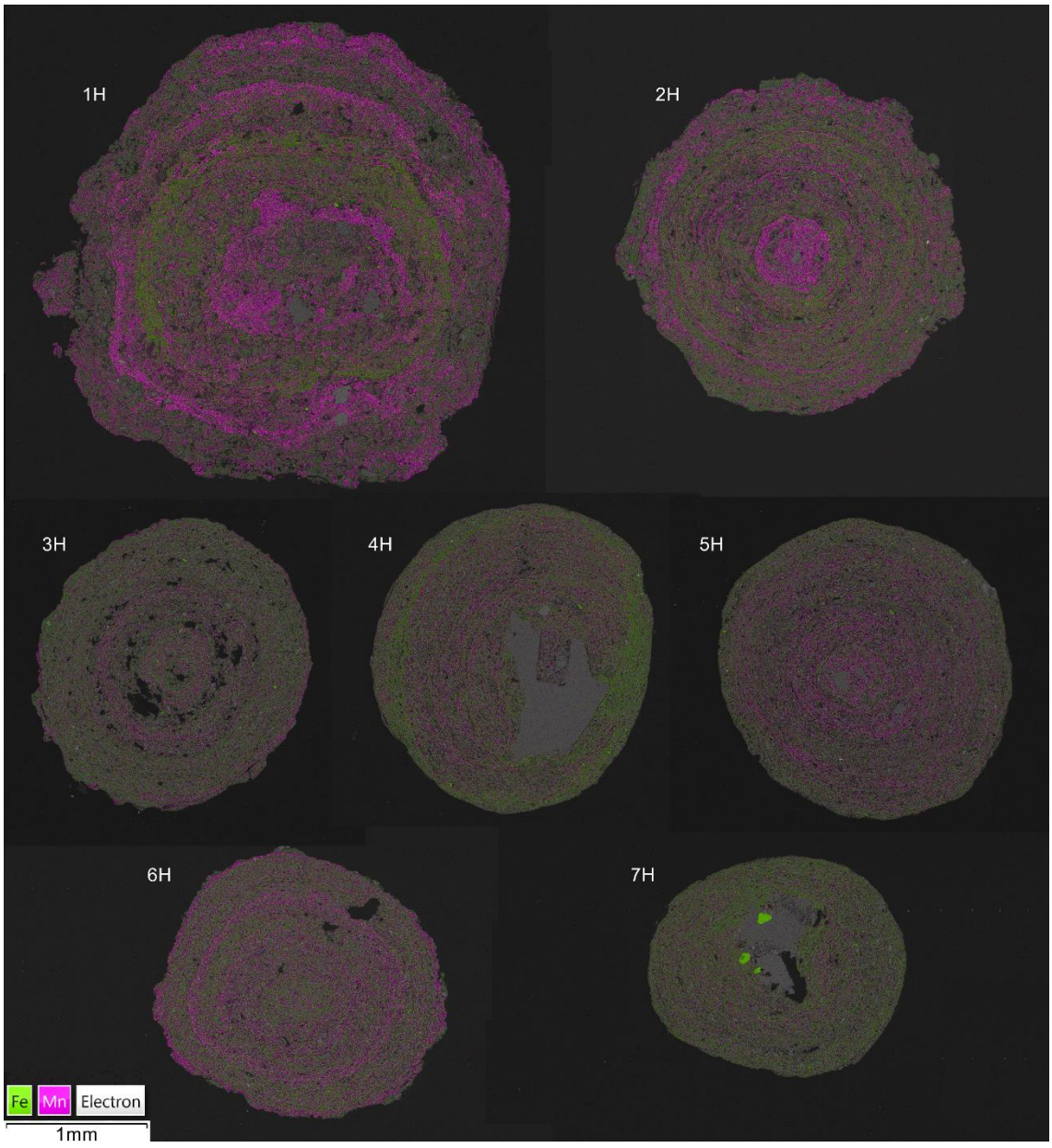

Figure 9. FE-SEM Fe-Mn elemental mapping of Zr5 thin sections.

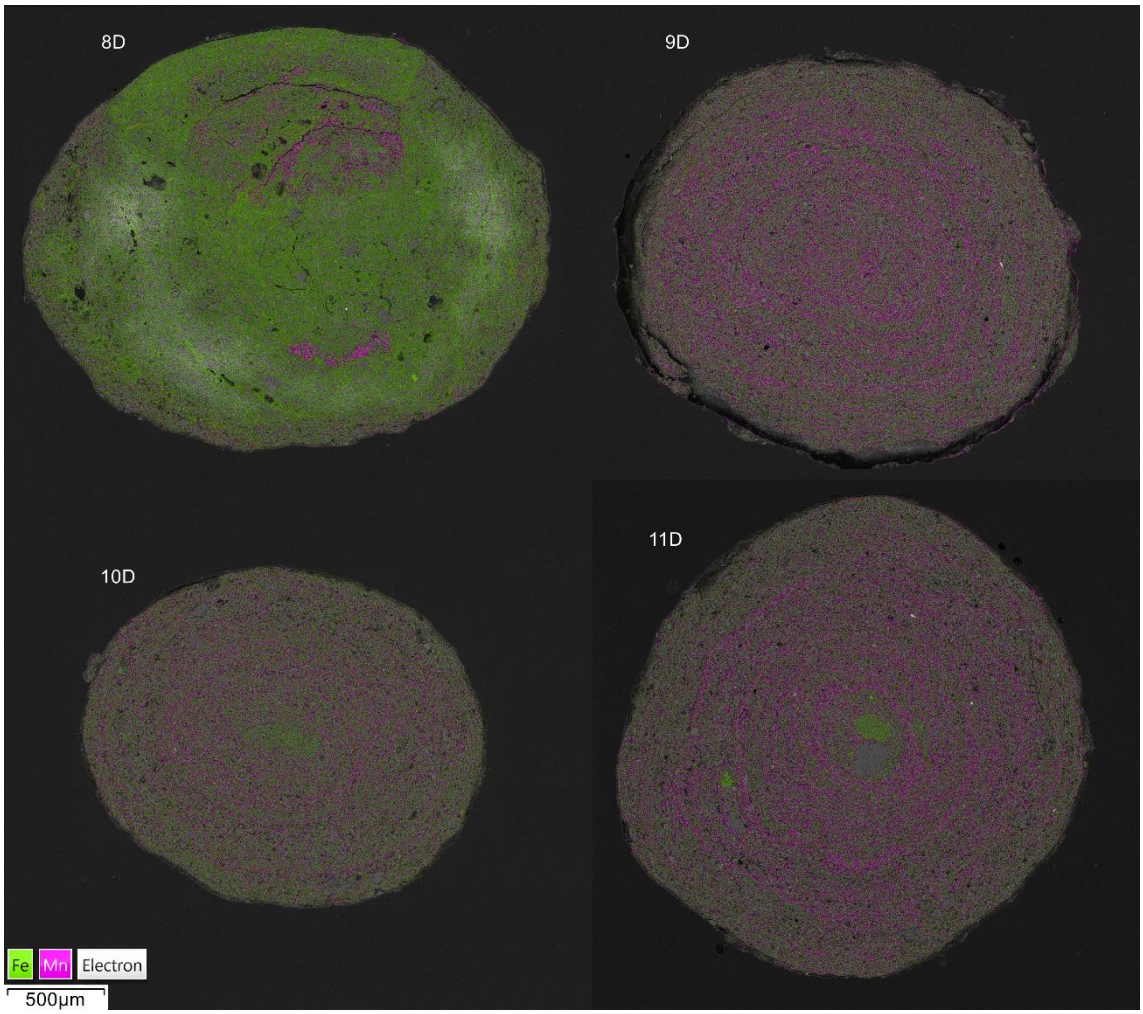

Figure 10. FE-SEM Fe-Mn elemental mapping of Zr5 thick sections.

5.2. EDS-SEM point measurements

A total of 14 samples were chosen for EDS-SEM point analysis. On most samples, two radial lines, located 50–55 µm apart and consisting of 8–16 points along the nodule radius were measured. Where no distinct difference between measurement points was observed under secondary electron imaging, a single line was used. Measurement locations are visualized on FE-SEM Fe-Mn mapping images with distribution mass fractions of Si, Fe and Mn displayed on graphs in Figures 11–24. Six samples from PLA15 assemblage were selected (Figures 11–16), one from Zr7 (Figure 17) and seven samples from Zr5 (Figures 18–24). Full results containing measured minor elements are found in Appendix A.

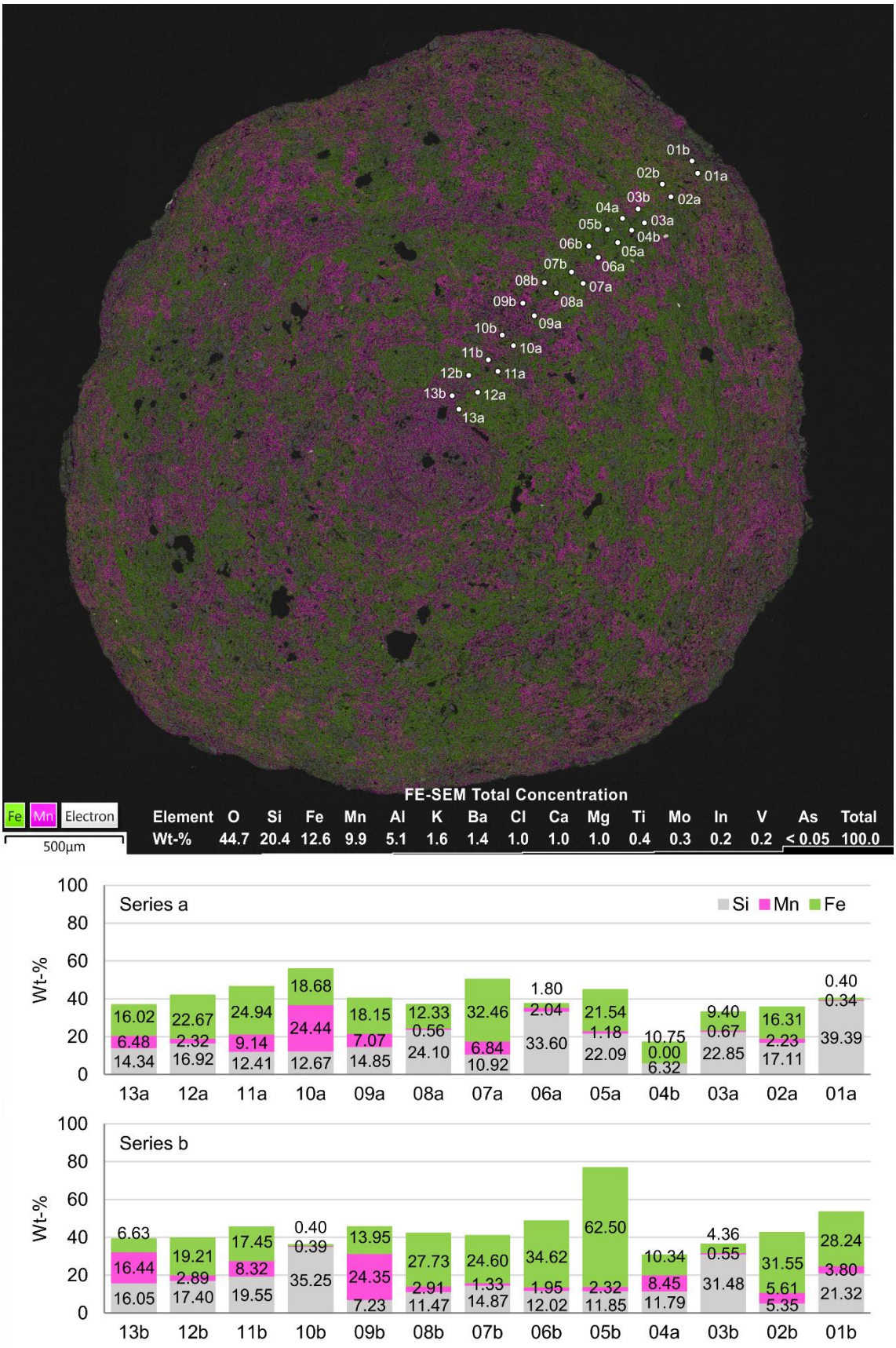

Figure 11. EDS-SEM Fe-Mn-Si concentration analysis locations superimposed on FE-SEM Fe-Mn map in sample PLA15-1H. Concentrations in wt-%.

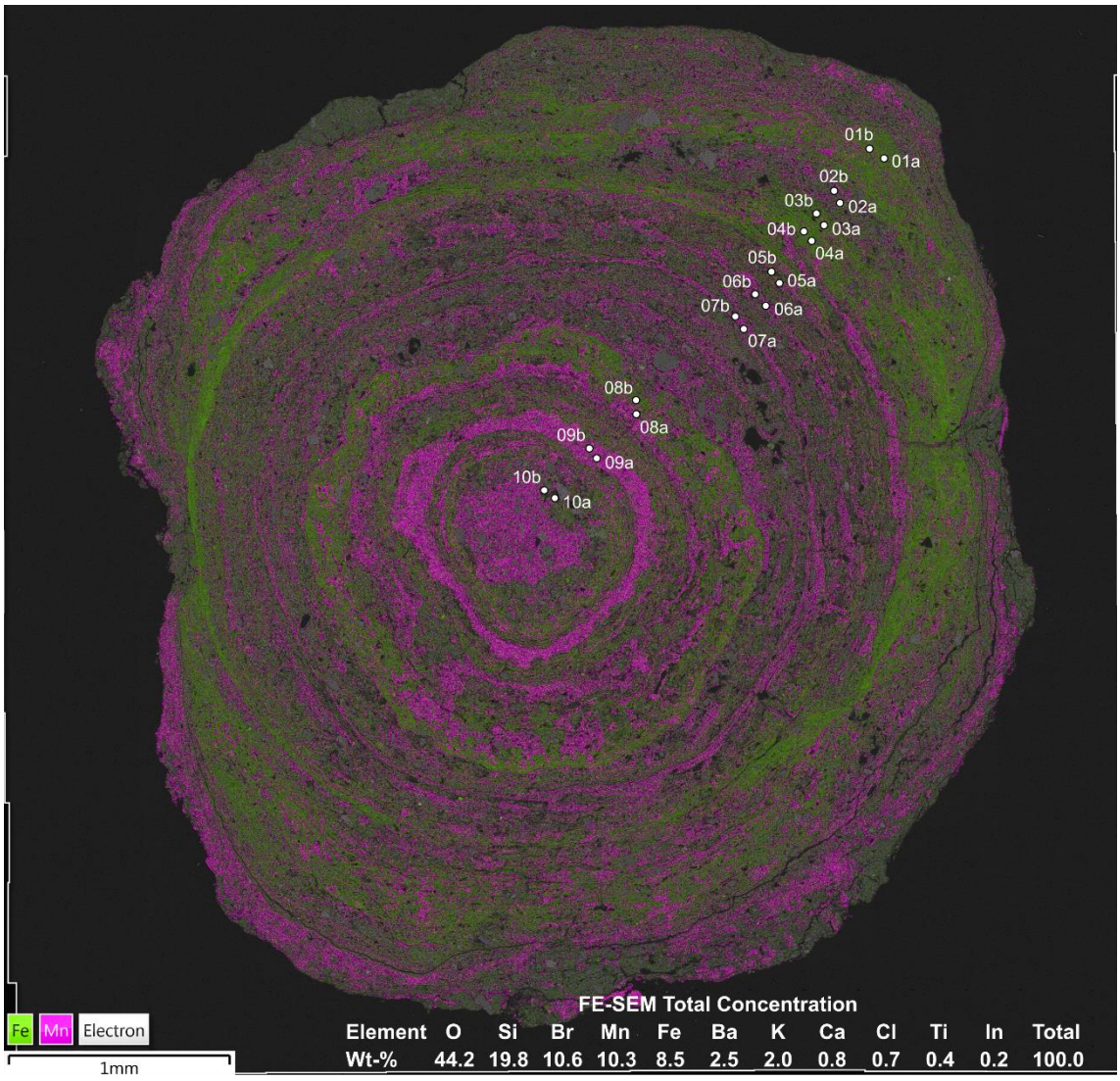

Figure 12. EDS-SEM Fe-Mn-Si concentration analysis locations superimposed on FE-SEM Fe-Mn map in sample PLA15-2H. Concentrations in wt-%.

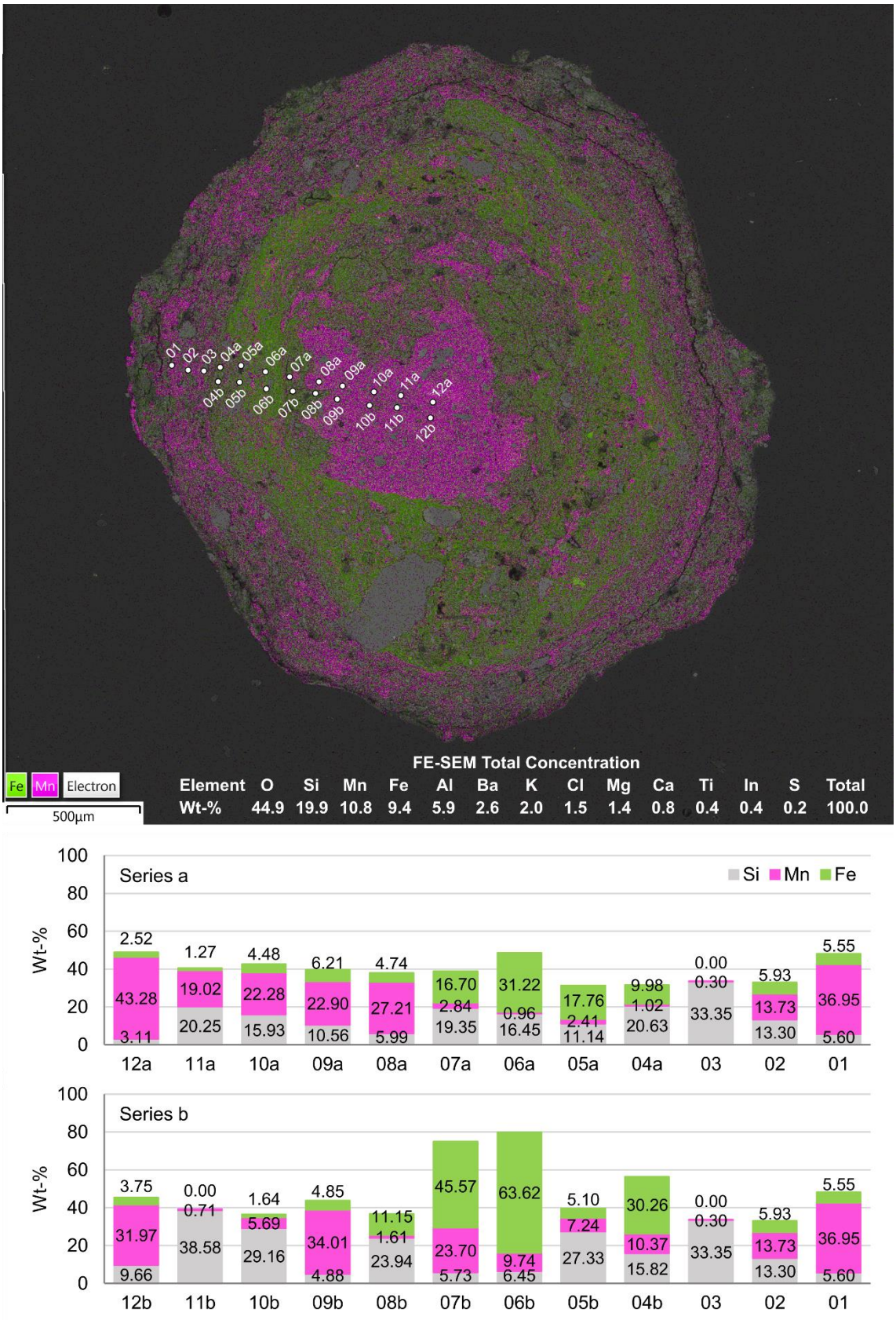

Figure 13. EDS-SEM Fe-Mn-Si concentration analysis locations superimposed on FE-SEM Fe-Mn map in sample PLA15-5D. Concentrations in wt-%.

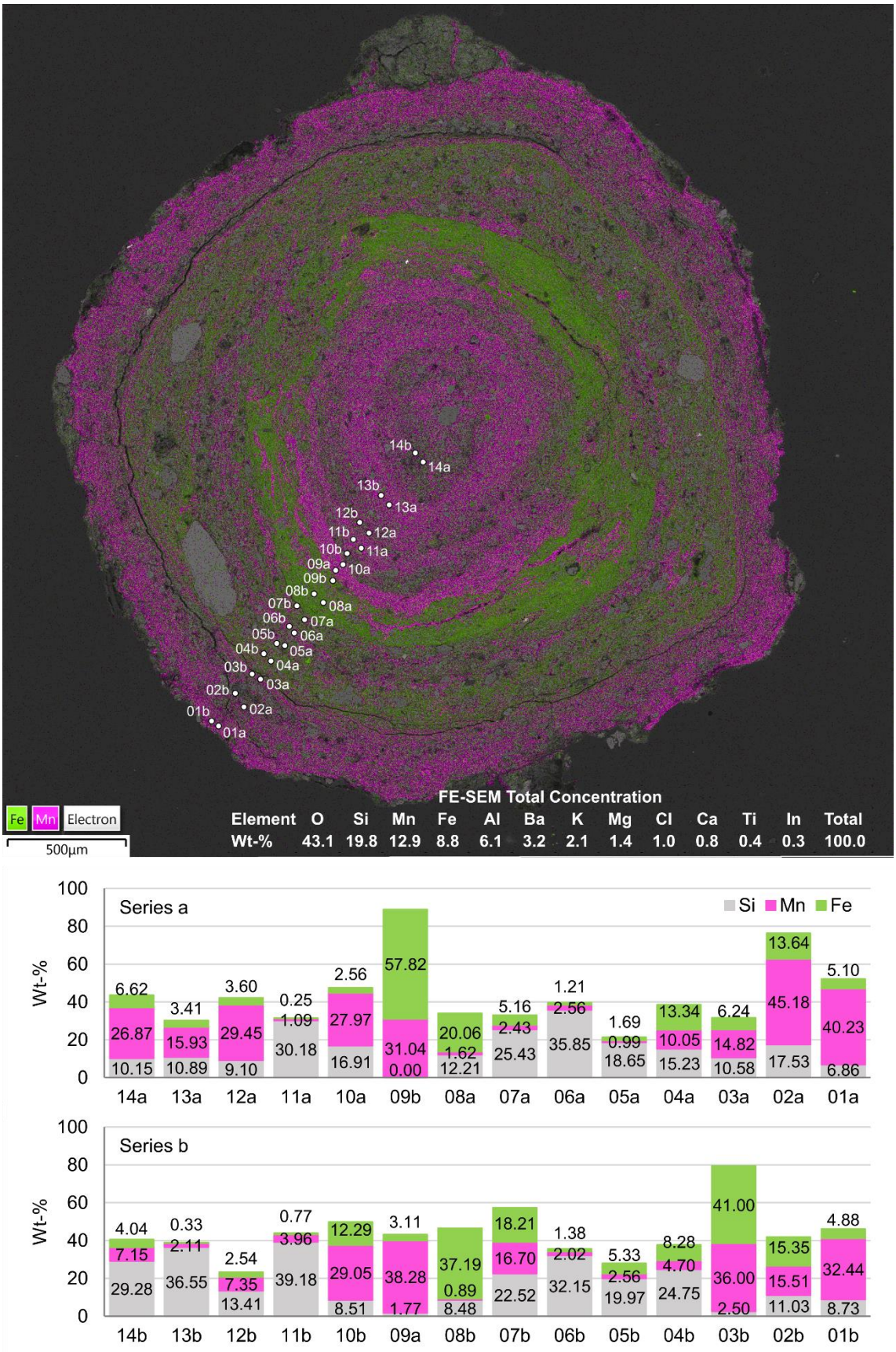

Figure 14. EDS-SEM Fe-Mn-Si concentration analysis locations superimposed on FE-SEM Fe-Mn map in sample PLA15-8D. Concentrations in wt-%.

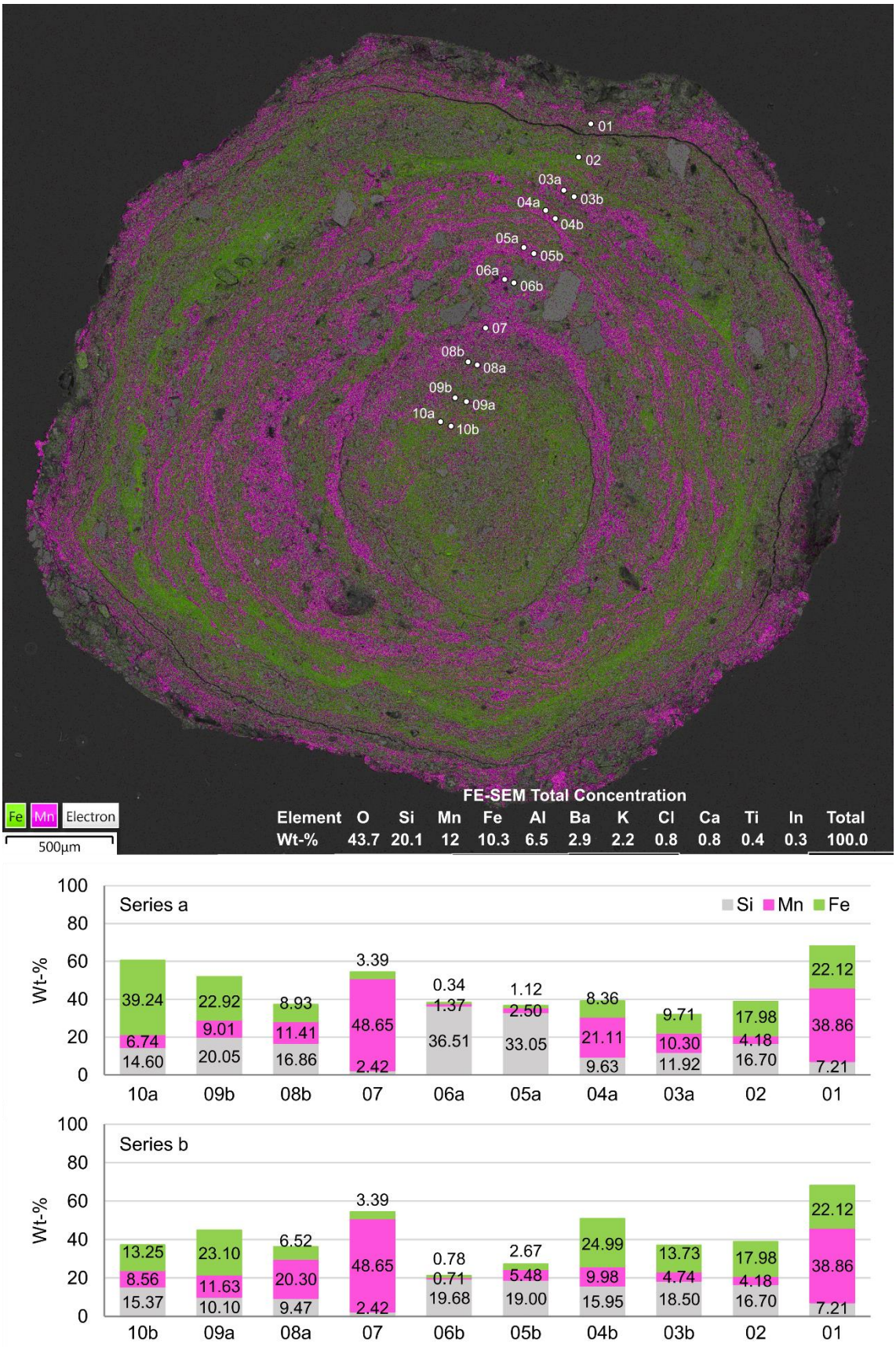

Figure 15. EDS-SEM Fe-Mn-Si concentration analysis locations superimposed on FE-SEM Fe-Mn map in sample PLA15-10D. Concentrations in wt-%.

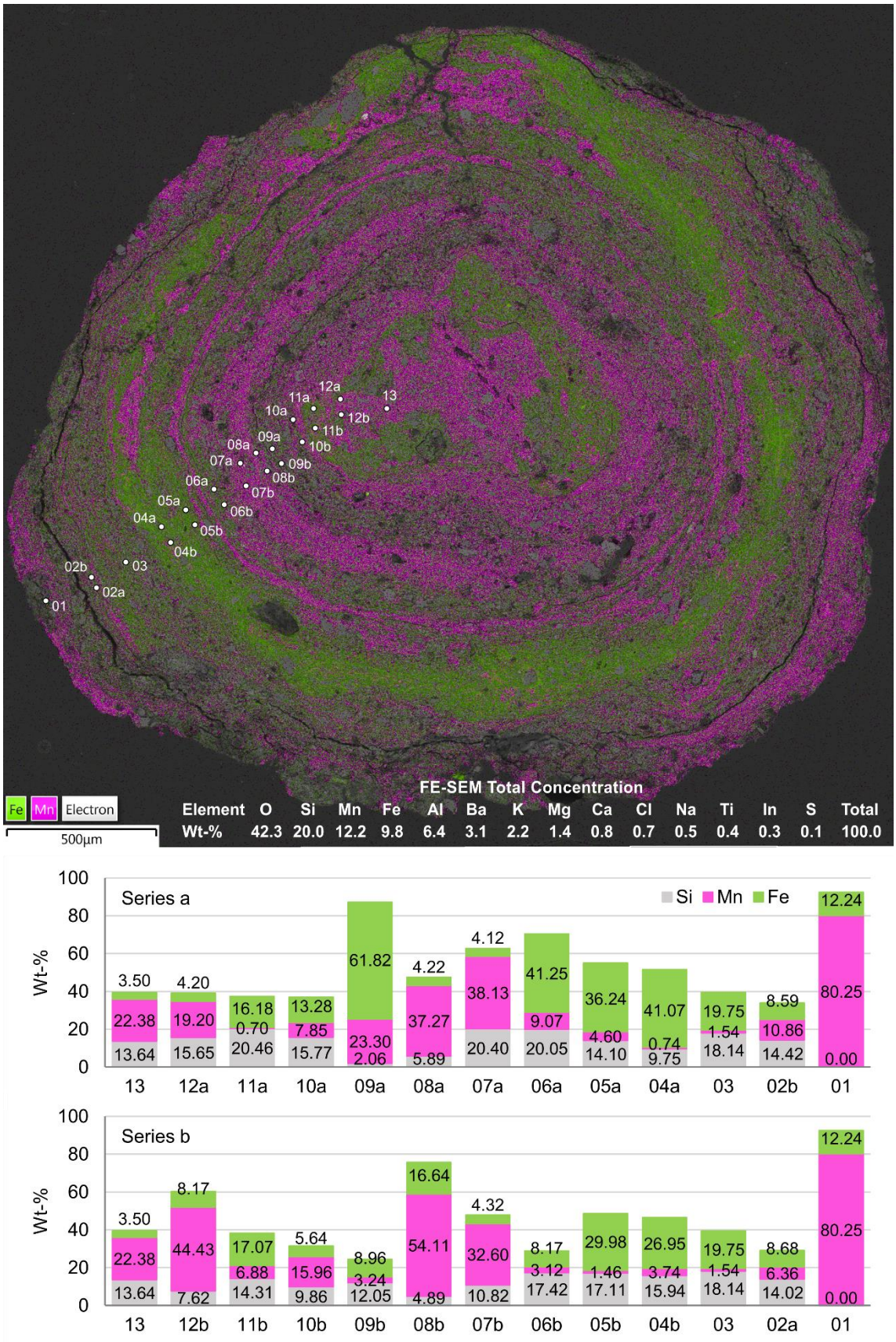

Figure 16. EDS-SEM Fe-Mn-Si concentration analysis locations superimposed on FE-SEM Fe-Mn map in sample PLA15-11D. Concentrations in wt-%.

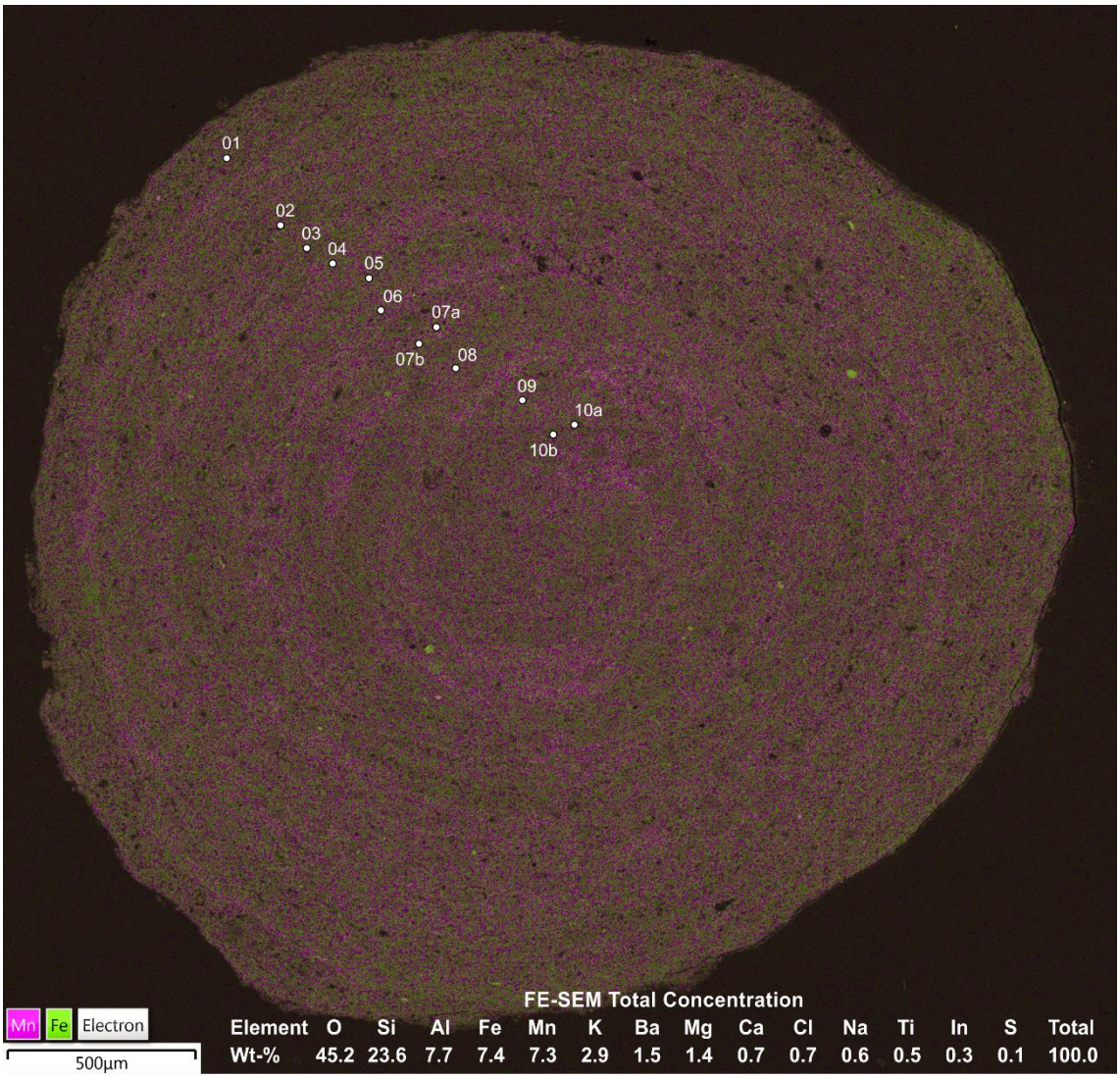

Figure 17. EDS-SEM Fe-Mn-Si concentration analysis locations superimposed on FE-SEM Fe-Mn map in sample Zr7-7D. Concentrations in wt-%.

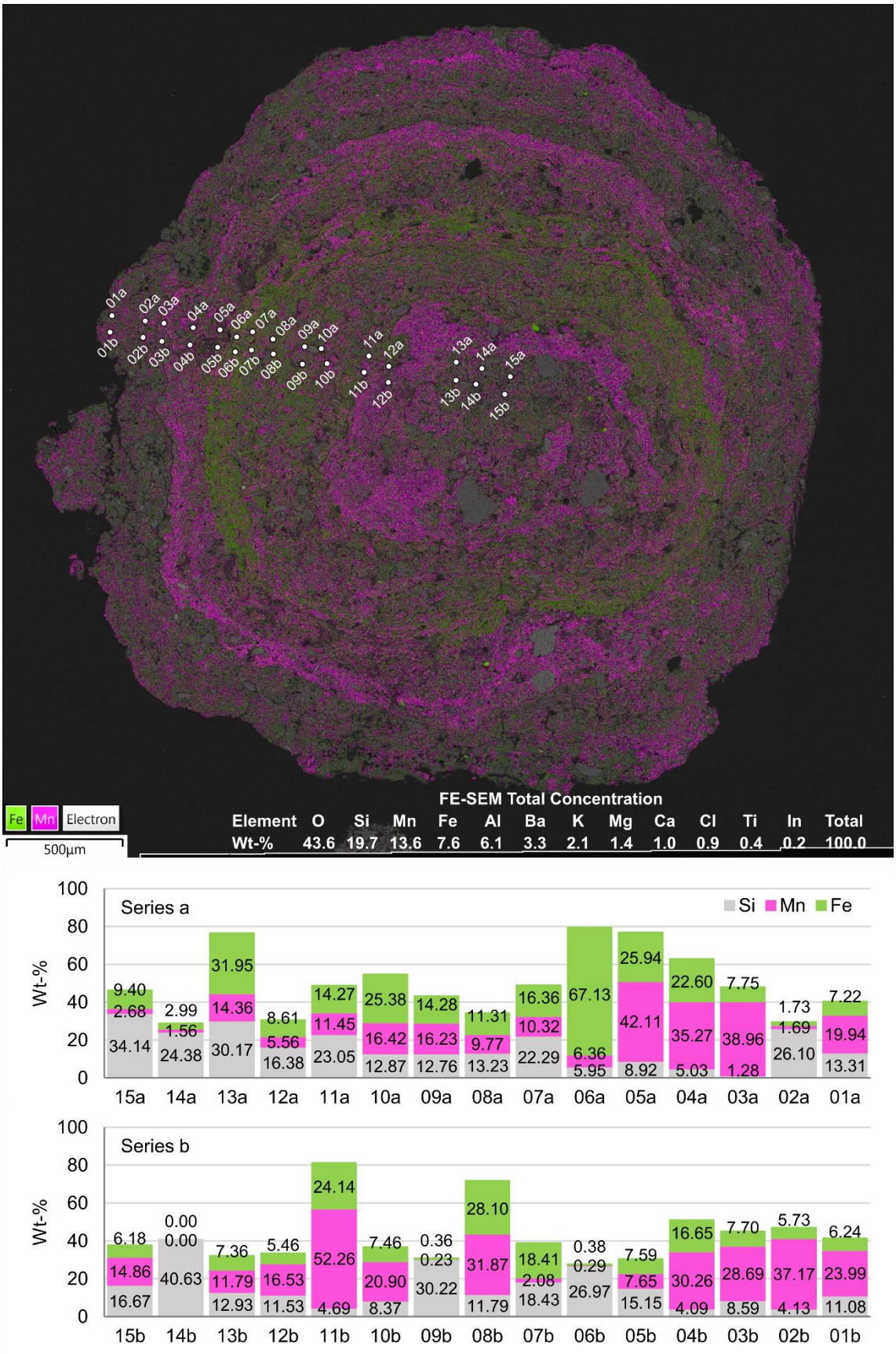

Figure 18. EDS-SEM Fe-Mn-Si concentration analysis locations superimposed on FE-SEM Fe-Mn map in sample Zr5-1H. Concentrations in wt-%.

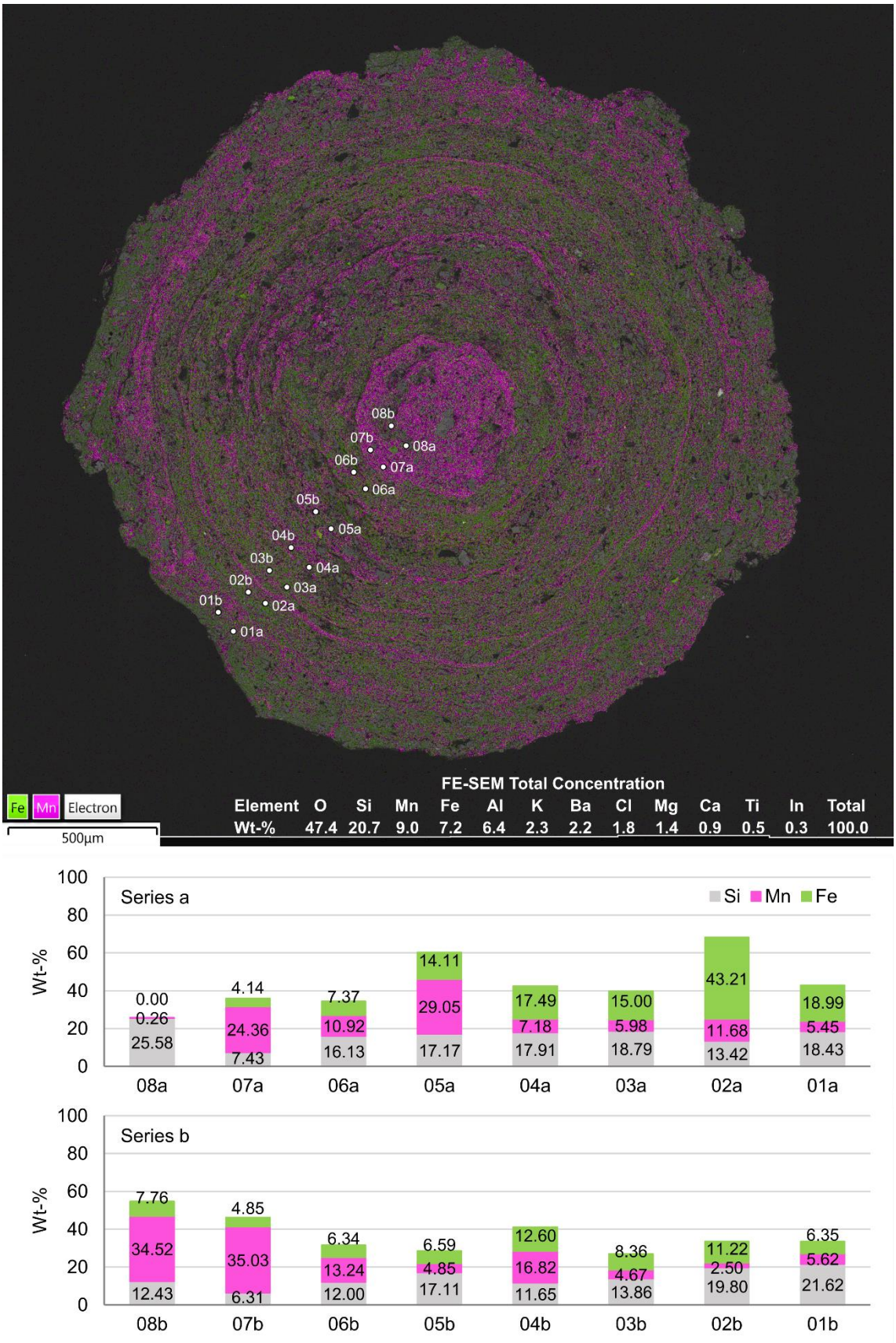

Figure 19. EDS-SEM Fe-Mn-Si concentration analysis locations superimposed on FE-SEM Fe-Mn map in sample Zr5-2H. Concentrations in wt-%.

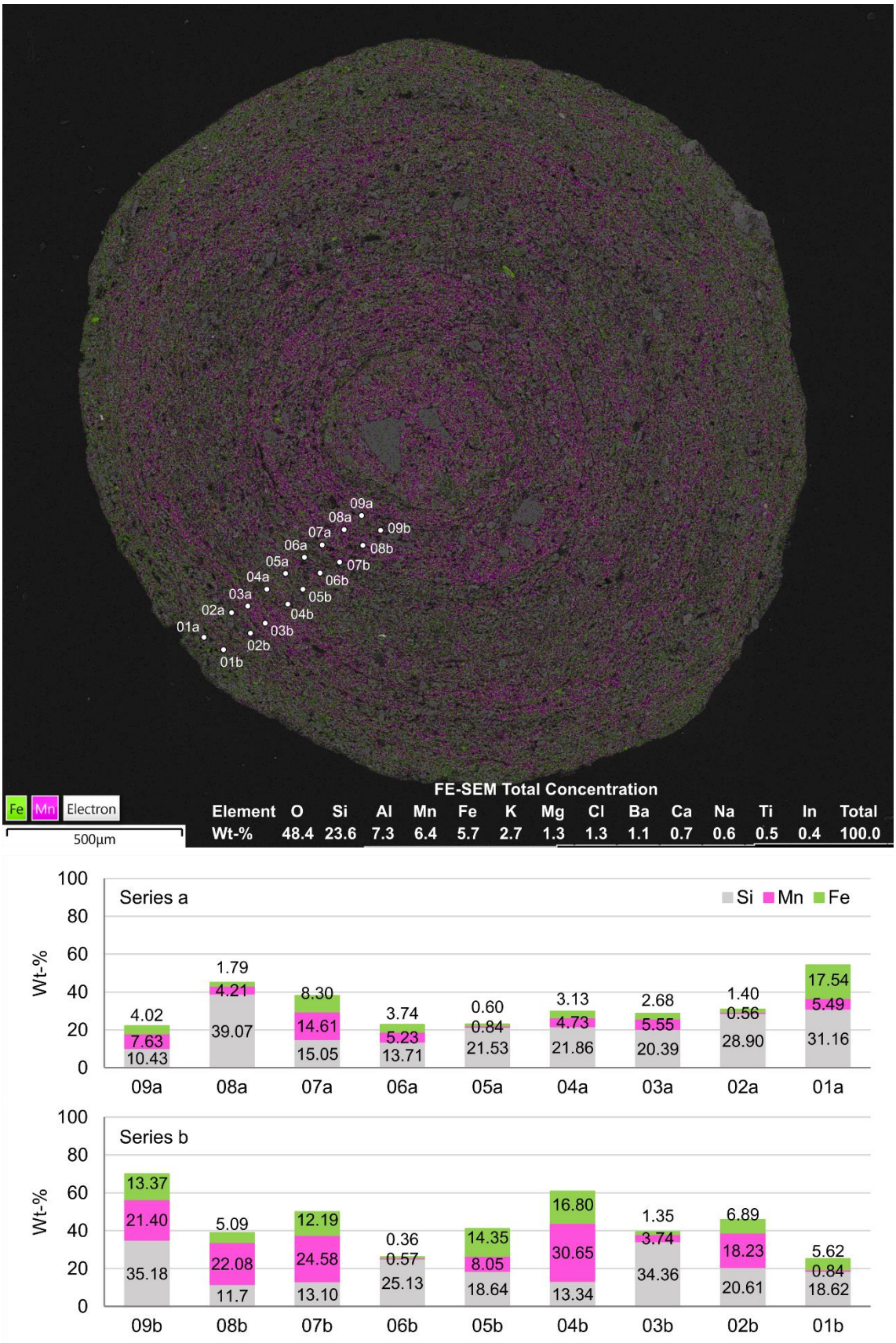

Figure 20. EDS-SEM Fe-Mn-Si concentration analysis locations superimposed on FE-SEM Fe-Mn map in sample Zr5-5H. Concentrations in wt-%.

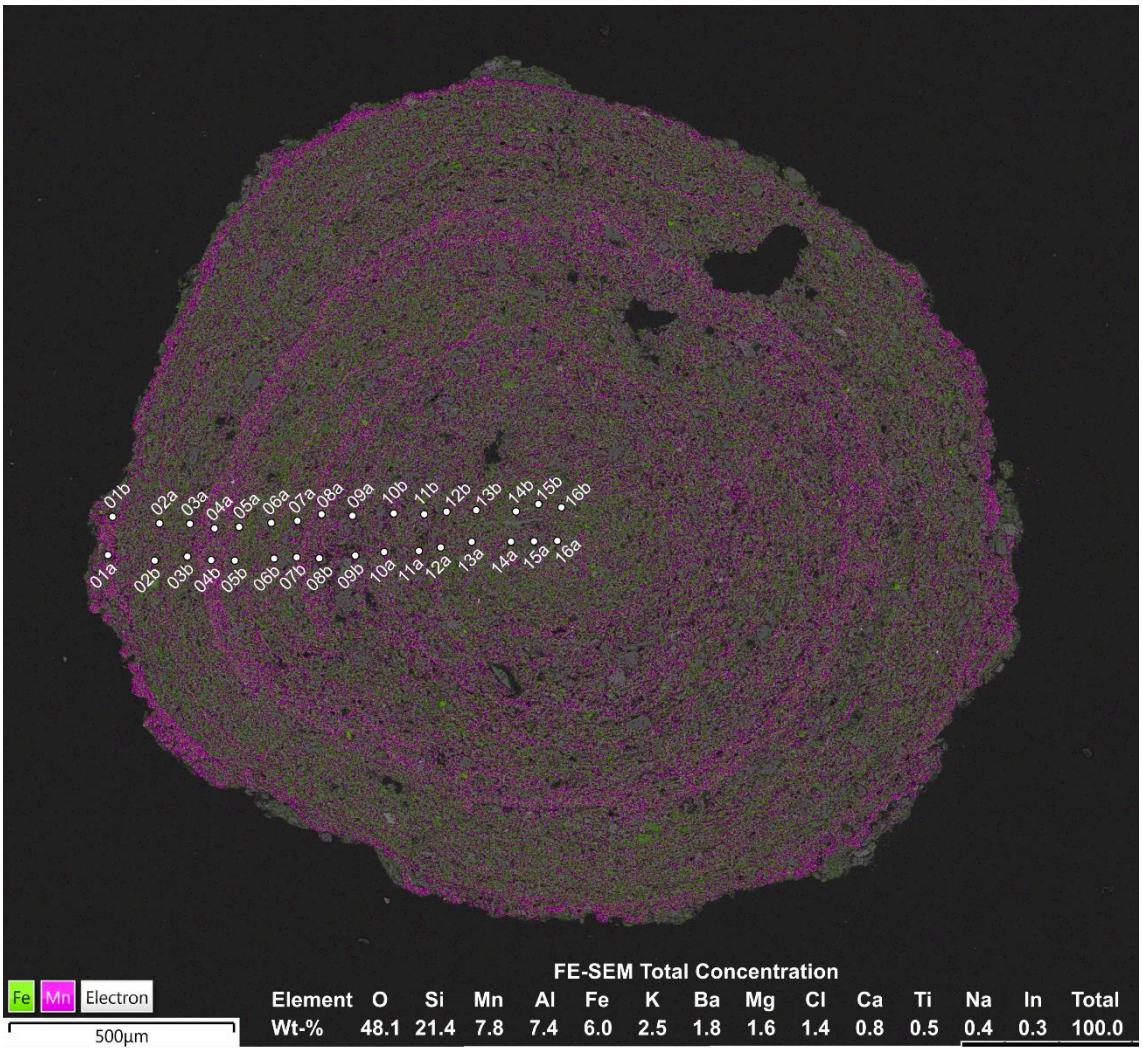

Figure 21. EDS-SEM Fe-Mn-Si concentration analysis locations superimposed on FE-SEM Fe-Mn map in sample Zr5-6H. Concentrations in wt-%.

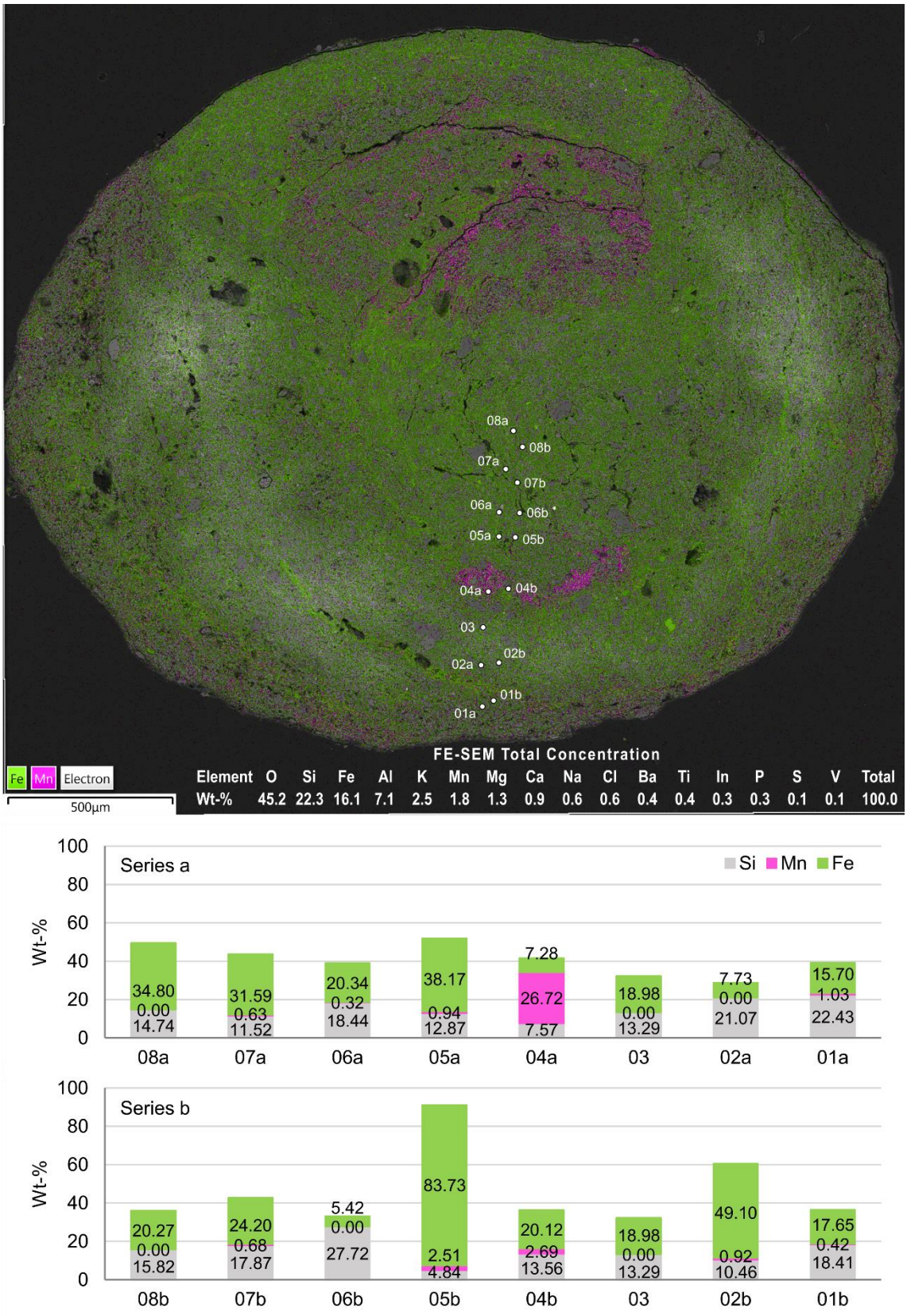

Figure 22. EDS-SEM Fe-Mn-Si concentration analysis locations superimposed on FE-SEM Fe-Mn map in sample Zr5-9D. Concentrations in wt-%.

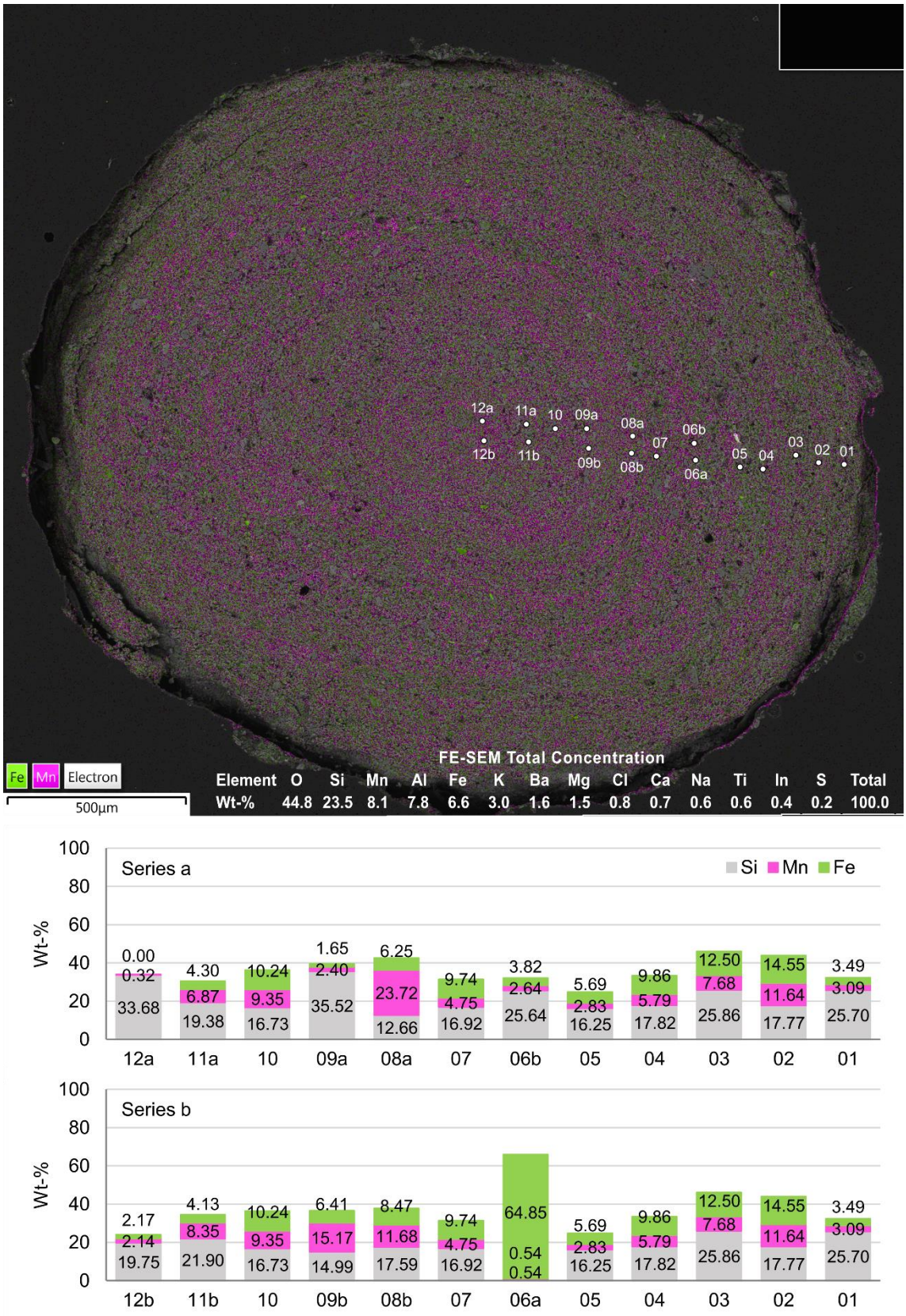

Figure 23. EDS-SEM Fe-Mn-Si concentration analysis locations superimposed on FE-SEM Fe-Mn map in sample Zr5-10D. Concentrations in wt-%.

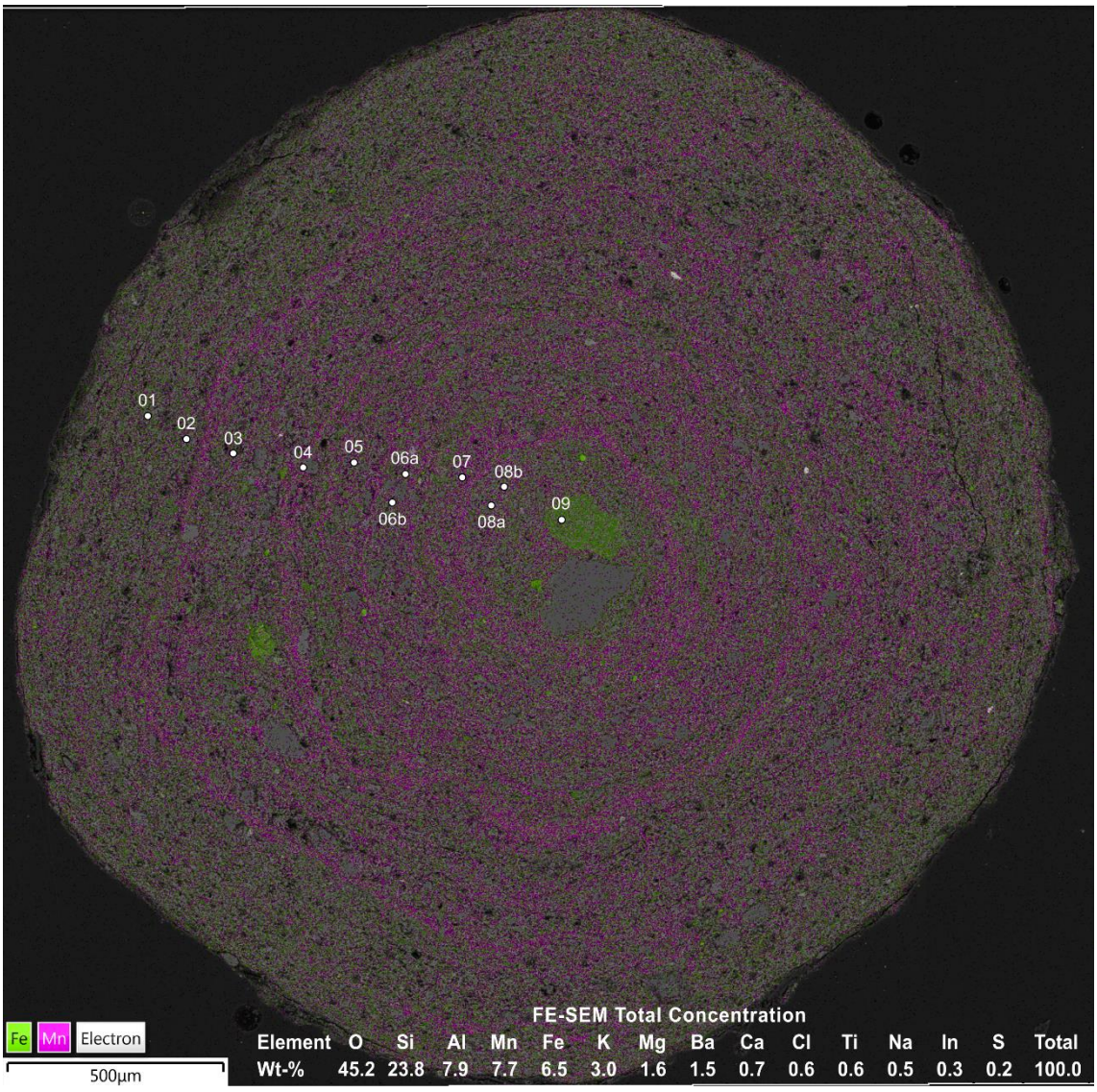

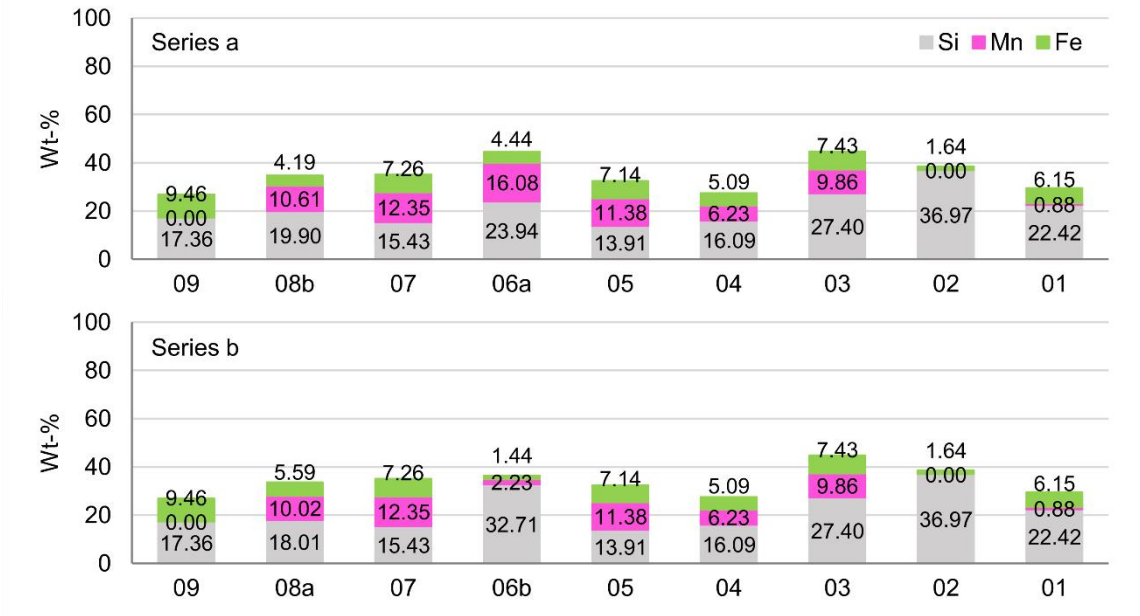

Figure 24. EDS-SEM Fe-Mn-Si concentration analysis locations superimposed on FE-SEM Fe-Mn map in sample Zr5-12D. Series a and b are combined where only one measurement exists. Concentrations in wt-%.

6. DISCUSSION

6.1. Quality of measurements

EDS-SEM is a proven method for elemental microanalysis, but it poses several limitations that some are part of the method itself and some are unique to the study of poorly crystalline, brittle and porous materials. While EDS-SEM analysis is capable of matching the analytical accuracy and precision of wavelength dispersive spectrometry (Ritchie et al. 2012), the reliance on automatic characteristic X-ray peak identification and the beam effects on uneven sample surface topography in brittle material add considerable uncertainty to the data.

Reliance on automatic peak identification, in this case the Oxford Instruments Inca and Aztec software controlling the EDS-analysis, means that the control of matrix correction calculations and validation of standardless analysis procedures is left to the control of proprietary software. This is known to produce very reliable results as long as strict measurement protocol is followed (Newbury and Ritchie 2013). The following optimization parameters are chosen by the instrument operator: optimised EDS time constant (resolution), solid angle of the EDS, beam current optimization for acceptable dead time, EDS energy calibration and spectrum count number adjustments. After instrument optimization, however, the possibility of incorrect elemental assignments can still take place not only in trace level constituents but on major constituent levels as well (Newbury and Ritchie 2013).

The brittle, microcrystalline structure of the samples made the material more difficult to polish to high standards as well as subjected the sample surfaces to rapid deterioration during transportation and possibly carbon coating. Deterioration of the surface increases the chances of errors caused by the lack of control of sample geometry (shape, local inclination). This poses the risk of introducing geometric errors of relatively high magnitude (Newbury and Ritchie 2013).

Aztec and Inca calculate the standard deviation of the concentration (σ_C) to determine the confidence interval of each of the calculated element concentrations. These calculations,

although being subject to slight variation between different manufacturers, are described in detail by Goldstein et al. (2003) and take into account the major sources of variation in k-ratio ($k = I_{unknown} / I_{standard}$, where I is measured X-ray intensity) which include the counts for characteristic peaks and the background for both the $I_{unknown}$ and for the standard denominator. Software provided standard deviation calculations for measurements where σ of 0.0 ($\sigma < 0.05$ rounded to one decimal place) was achieved for all major elements apart from oxygen (O) measurements which all had σ of 0.1 ($0.05 \leq \sigma \leq 0.10$ rounded to one decimal place) in FE-SEM. In EDS-SEM point measurements, a σ of 0.0 was achieved for major constituents and σ of 0.1 for some minor constituents. Both FE-SEM and EDS-SEM measurement calculations were optimized for low σ major element identification. Disqualification of σ over 0.1 reduces sensitivity for trace and minor elements.

Two elemental anomalies are present in FE-SEM peaks identified by the Aztec software. Sample PLA15-2H is measured to contain 10.6 wt-% of Br. As Al is not detected in sample, the measurement appears as a peak misassignment error mixing the Br L_α transition (1.480 keV) and Al K_α transition (1.486 keV) energies. This renders PLA15-2H compositional FE-SEM calculations unusable. A systematic error is also present as identification of In in all samples with a concentration of ~0.3 wt-% in each sample. In was not detected at all in any of the samples by EDS-SEM point measurements, nor is it likely that any of the most probable interfering elements would be present in such steady concentrations in all samples. Thus In measurements can be a result of systematic peak misidentification caused by energy resolution of the detector where either escape peaks or lower order transition peaks are systematically being misassigned.

EDS-SEM point analysis, while retaining σ value standard of 0 for major elements and 0.1 for some minor elements, show impossibly high Fe values on the most Fe rich parts of some nodules. In sample Zr5-9D (Figure 22) measurement 05b shows Fe content of 83.73 wt-% which, when converted to either FeO or Fe_2O_3 would yield Fe oxide content percentages of 107.7 and 125.4, respectively. Another high Fe measurement can be found from sample Zr5-10D (Figure 23) measurement 06a. However, due to low concentration of other elements in the measured spot, the result of 64.85 wt-% would translate a to 83.4 % pure FeO, putting it in realm of plausible, although unlikely.

6.2. Representativeness of data

The number of samples, 29 FE-SEM maps and 14 EDS-SEM point samples, is not high enough to establish robust picture of nodule characteristics from different sample collection points. Neither is the sample count high enough to establish credible statistical correlations of sample surface bulk elemental compositions. Furthermore, nodules of different sizes cannot be directly compared as their structure and Fe-Mn oxide enrichment varies depending on the nodule size. Nodule equatorial surface bulk composition was measured, but it is not a working approximation for the total chemical composition of the nodule due to the anisotropy of the chemical composition and asymmetry of nodule shape.

Samples prepared as thin sections, particularly larger samples PLA15-3H and PLA15-4H, suffered notable degradation during sample preparation and transportation. While the concentration results obtained from these two samples fall roughly in line with results from rest of the PLA15 samples, the loss of large fragments in samples likely skews the results. The relative uniformity of both structure and elemental composition of PLA15 samples suggests that the sample series is fairly representative of Fe-Mn nodules of 3.5–5 mm in size found in the upper Bahe Fm.

Apart from samples Zr5-1H and Zr5-2H, both of which were of larger size (3.6 and 3.1 mm, respectively), all the Zr5 and Zr7 samples are of smaller size and display considerably higher heterogeneity in appearance and Fe and Mn concentrations. This, however, is to be expected as these samples represent nodules in earlier steps of the nodule formation process where the concentric ring structure is absent or in early stages of formation. Due to the sample count, there is no way to assess whether even more heterogeneity would be present in significant numbers in both Zr sample series and whether any trends of prevailing nodule elemental compositions could arise. As Zr5-1H and Zr5-2H were the only available samples of larger size, it is not prudent to suggest that they are wholly representative, even though observations in larger PLA15 samples suggest that longer formation times and increased nodule maturity increases compositional homogeneity.

The EDS-SEM point measurements are limited in number. The measurement points were chosen under SEM imaging with aim of capturing the composition of phases discernible

under SEM imaging. Instrument time permitting, a more continuous line would yield more consistent data of nodule element distribution. The limitations of low amount of data points is also visible within phases, as most samples have two measurement point for each observed phase placed roughly, 50–55 µm from each other. The percentage difference of Fe and Mn concentration values measured from neighbouring points varies between 0.65–194.5 %. Due to the very poorly crystalline nature of the nodule material it is also impossible to have a line of measurements that represents the entire nodule, as major element concentrations vary to a great degree even within few µm and within the same internal structural element. Thus, the Fe-Mn elemental distribution is visually best represented in FE-SEM imaging. EDS-SEM does provide valuable information of co-existence and abundance of Fe and Mn oxides in different nodule horizons.

6.3. Observations on elemental distribution and structure

6.3.1. PLA15

The large size of the samples contributes the increase in structural complexity and elemental separation (Gasparatos 2012, Yu et al. 2015, Sipos et al. 2016). The irregularity in overall shape and interior structure is likely driven by the anisotropy of the internal pore network affecting the distribution of metal translocation from the nodule surface to the interior (Yu et al. 2015). The anisotropy of the pore network is likely caused by partial clogging by clay minerals (Rhoton et al. 1993) or microscale variations in the soil pore space redox settings.

The separation of Fe and Mn is thought to begin during the initial nodule formation with both metals being able to precipitate onto the surface of the nodule as oxides. The commonly seen high Mn content can be the result of nodule interior conditions being more oxidizing during proto-nodule formation (Yu et al. 2015). However, Mn enrichment of the nodule interior has been shown to happen after the very initial phases of nodule formation (Jien et al. 2010). The pedoenvironmental implication is that the Mn impregnation could happen in soil redox settings where the conditions alternate between reducing and oxidizing settings for Fe but remain always reducing for Mn as suggested by White and Dixon (1996). Sample PLA15-10D lacks the manganese enriched interior,

appearing to have a heavily Fe rich interior in FE-SEM imaging. This atypical feature could be a result of different initial time frame and redox settings during proto-nodule formation, but it would not account for the lack of Mn translocation. However, upon inspection of the individual Mn-distribution map (Figure 25), the anisotropic penetration of Mn towards the nodule interior could be a result of lower than usual porosity in the initial nodule. Lesser porosity prevents Mn translocation towards the interior implying that the observed higher Fe/Mn ratio mainly results from the lack of Mn impregnation.

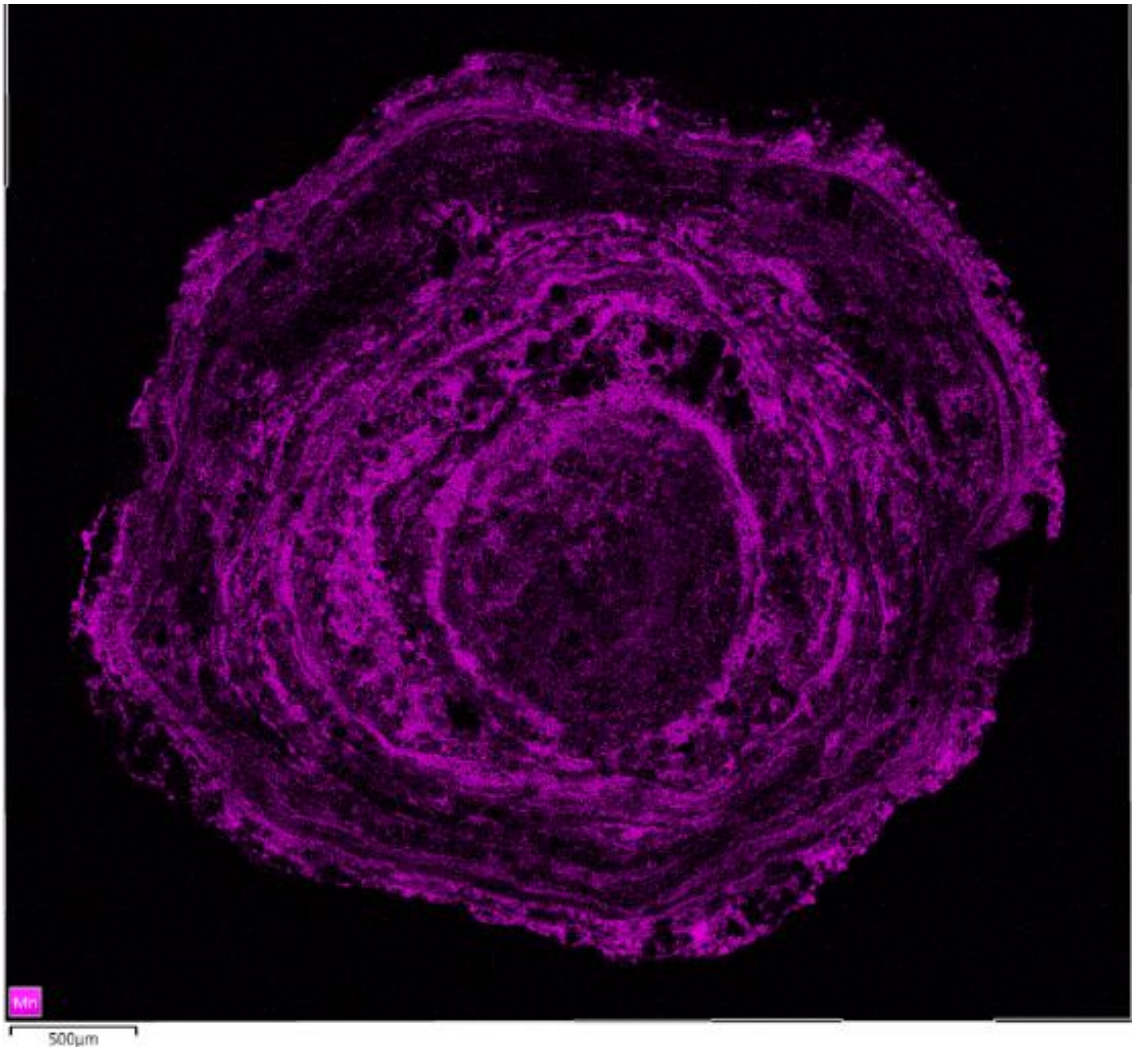

Figure 25. FE-SEM Mn-distribution map of sample PLA15-10D

As the nodule matures, the concentric ring structure starts to grow via precipitation, the separation of Fe and Mn becomes more pronounced. The different bands can be dominated by the presence of Fe, Mn or both Fe and Mn oxides (Figures 11–16). The separation into distinct structural bands is largely driven by the soil Eh changes, with slow, large magnitude changes in the soil redox state promoting higher differentiation

(Sipos et al. 2016). Fe precipitation window is in lower redox potential soil environment where Mn will not yet precipitate. The widening of the Fe band then requires the Eh settings to fluctuate mainly near the wet, low redox potential conditions (Yu et al. 2020). The higher redox potential window is where Mn precipitates over previously precipitated Fe oxides. Likewise, thickening of the Mn band is implicative of prolonged periods of soil redox state fluctuating in higher redox potential i.e. dryer conditions (Yu et al. 2020).

Most Fe bands host some measure of Mn, which is likely result of Mn(II) ions translocation through the nodule pore network as Fe precipitation takes place (White and Dixon 1996). However, present in many samples are bands where both Fe and Mn have precipitated in large quantities. Co-precipitation takes place during rapid increase of the redox potential meaning that the thickening of the co-precipitated band is indicative of rapid and repetitive large-scale fluctuations of the soil redox state (Yu et al. 2020).

Using this approach, it is possible to distinguish separate growth phases where different redox conditions prevail. Although the accuracy is limited by number of EDS-SEM data points and most importantly lack of pore fill data, five different growth phases can be identified from the sample PLA15-2H (Figure 26):

1) Mn enriched nodule interior, where the proto-nodule pore network is enriched in Mn due to the higher redox potential of the nodule interior.
2) Phase marked by relatively slowly changing soil redox conditions, allowing the precipitation of either Fe in wet, low redox potential conditions and Mn in dryer settings. Prolonged Fe precipitation windows are marked with Mn-ion translocation towards higher Eh conditions in the nodule through radial pore channels.
3) A phase during which the frequency and amplitude of the changes in soil redox settings is increased. While there are heavily Fe and Mn enriched spots in this band, the generally low enrichment of Fe and Mn suggests increased co-precipitation resulting lesser pore filling by free ions during rapid precipitation.
4) A prolonged phase of Fe precipitation in low redox potential. A thick, Fe rich band is marked with Mn pore fillings indicative of conditions where Mn-ions remain mobile in the soil solution and only precipitate in the soil pore network.
5) A distinct Mn rich crustal layer that has started to separate from the rest of the nodule. Precipitation takes place in higher redox conditions.

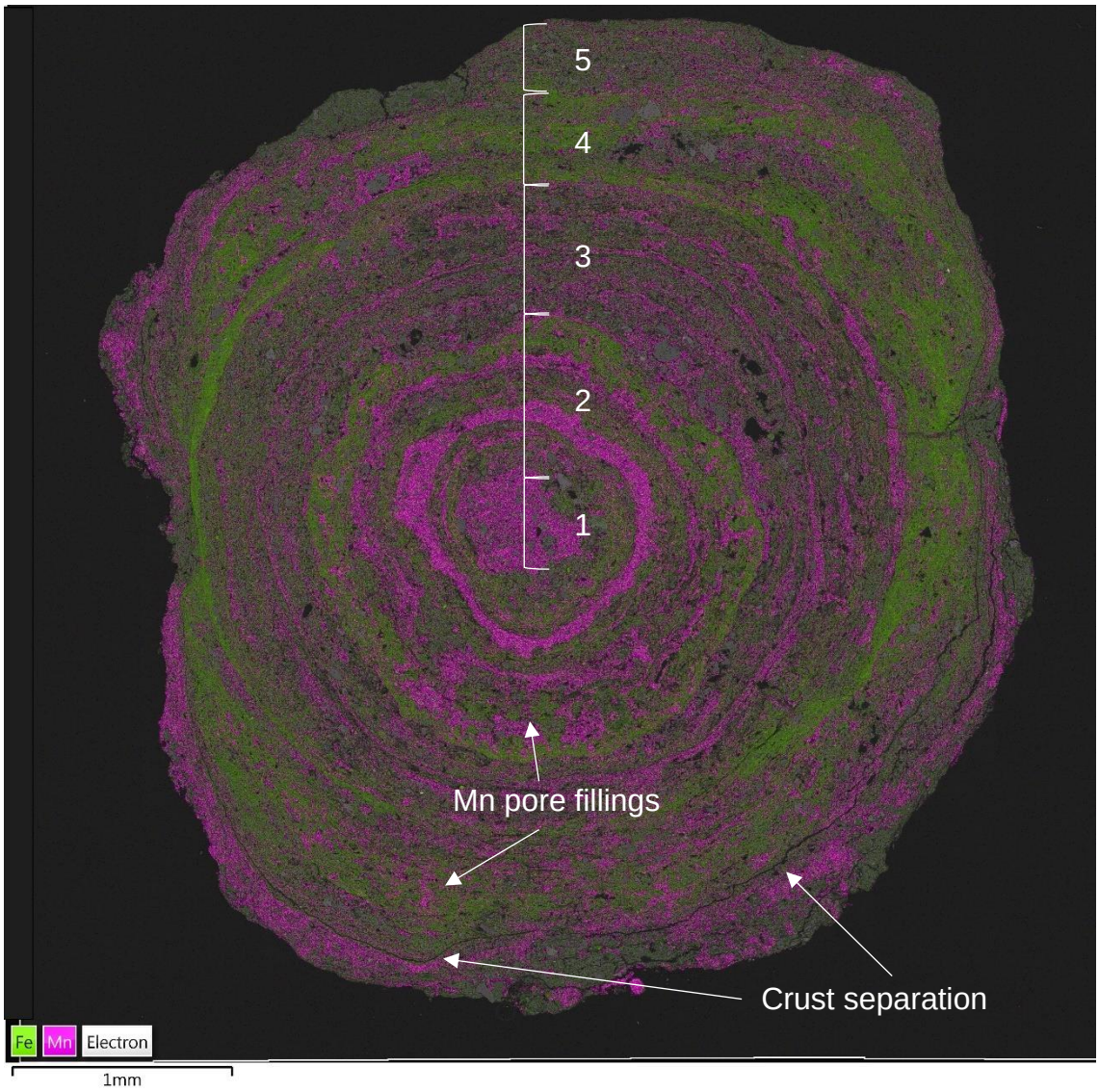

Figure 26. FE-SEM Fe-Mn map of PLA15-2H with interpreted growth phases. 1) Mn enriched nodule interior. 2) Relatively slowly changing redox conditions, where thicker successive bands of Fe and Mn oxides precipitate. 3) Rapid large-scale fluctuations of the soil redox state leading to precipitation of both Fe and Mn oxides 4) Prolonged, low redox potential Fe precipitation. 5) Mn rich crustal layer. Radial Mn pore fillings precipitated during Fe precipitation window in phases 2 and 4 and separation of crustal coating marked with arrows.

The crustal layer is clearly visible under SEM imaging in most PLA15 samples and is often rich in Mn (Figures 6–7). While the crustal layer commonly hosts some Fe, the prominent goethite coating typically associated with many types of pedogenic Fe-Mn nodules is not present (Vodyanitskii 2006). The separation of crustal band from the rest of the nodule can be a result of exfoliation during nodule metal enrichment process (Figure 27, Sipos et al. 2016). According to Sipos et al. (2016), exfoliation happens as the outer coating band is subjected to more reductive settings and ions are rapidly transported from the coating to the nodule interior with pore water. However, most nodules from

floodplain deposits studied by Sipos et al. (2016) largely lack the concentric ring structure seen in upper Bahe Fm nodules and consist only of Mn rich interior and Fe rich exterior. The crust separation is not present between any of the interior structural rings in any of the studied samples in upper Bahe Fm. Furthermore, the high Mn enrichment observed in the PLA15 samples does not directly support particularly rapid enrichment described by Sipos et al. (2016) as increased enrichment can be considered indicative of slower redox changes over a longer time (Yu et al. 2020).

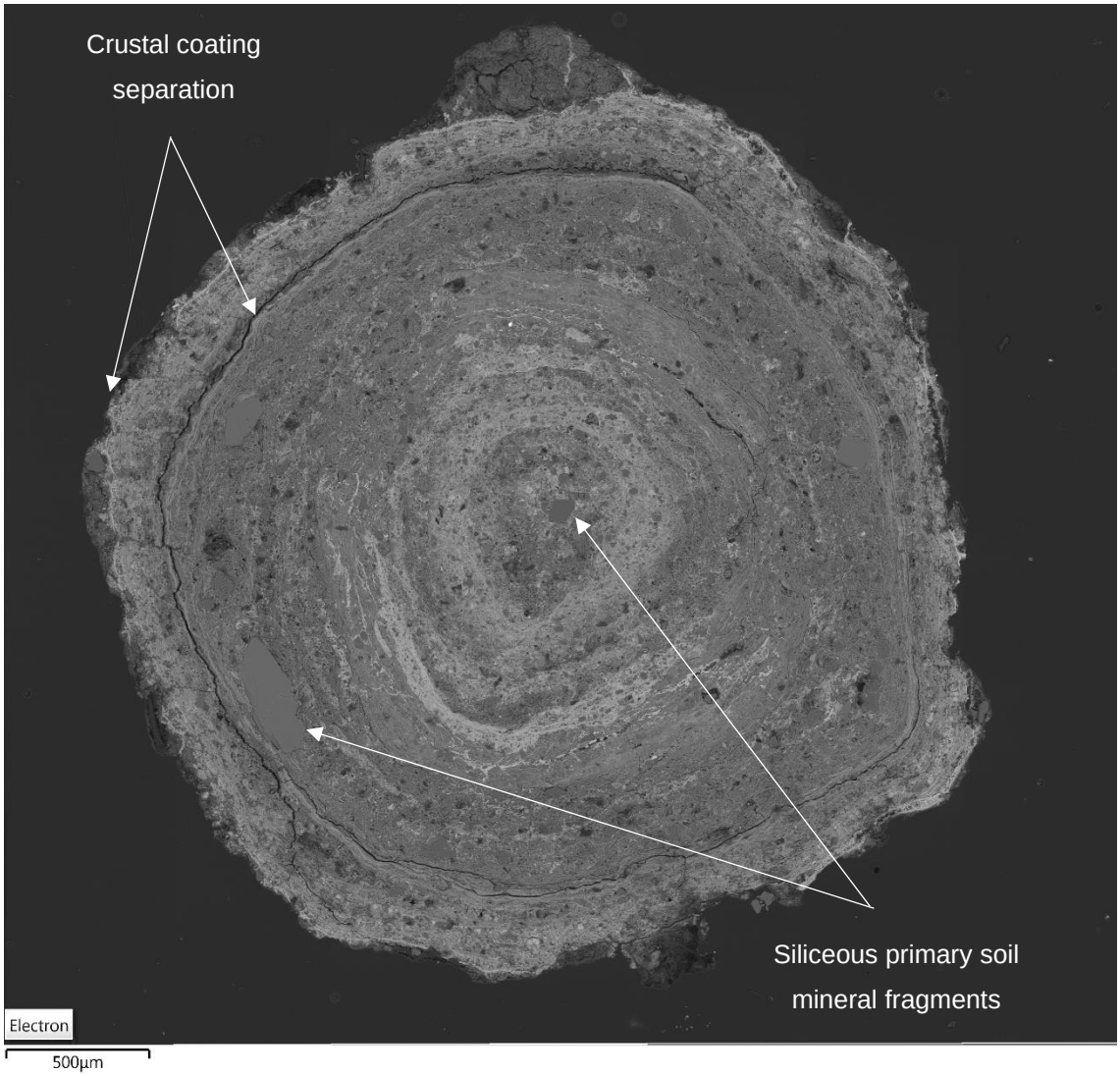

Figure 27. SEM montage image of the sample PLA15-8D. Visible are Si rich fragments in the nodule interior and exterior parts and the separation of the crustal layer.

It is possible, that the separation of the crust may be promoted by the tension of the swelling of clay minerals underside the crust (Sipos et al. 2016). There is evidence of the clay mineral content of the nodules influencing significantly the size of the nodules by

affecting the porosity and compactness of the nodule (Jien et al. 2010) and thus limiting the translocation of cementing metals via the nodule pore network.

It is also possible that the microfractures observed are a result of nodule formation ceasing. As precipitation of Mn takes place in higher redox states, Mn is typically dissolved and translocated from the surface towards the nodule interior where the conditions are less reductive allowing Mn to act as cement (Huang et al. 2008, Sipos et al. 2016). It then stands to reason that if more reductive conditions are not met for prolonged periods after initial crust precipitation, Mn cannot translocate towards the interior and act as cement in the pore spaces between the precipitated crust and the inner rings.

Samples PLA15-1H and PLA15-4H have a distinct distribution of Fe and Mn oxides. Lacking the concentric ring structure (Figure 28), they are mottled in appearance with irregular and blotchy distribution of oxides (1H) or almost channelized, radial expression (4H). Both samples lack the outer coating layer present in other samples of larger size. This form, where Mn is present mainly as crack and void fillings is the result of prolonged stay at the Fe precipitation window where Mn remains mobile (White and Dixon 1996) and can continue if the outer crust does not coat the nodule surface (Sipos et al. 2016).

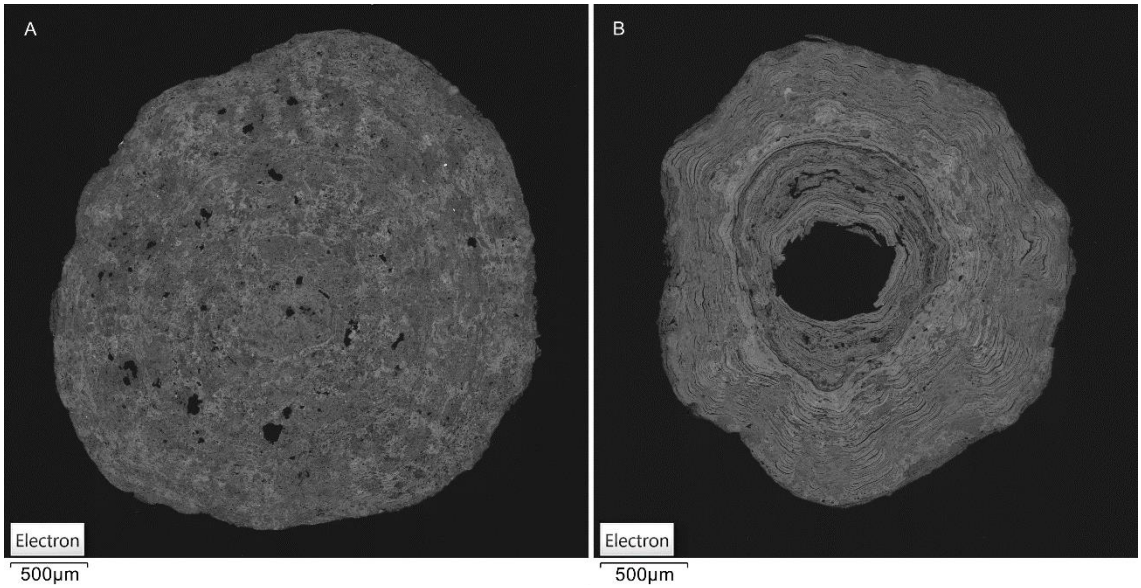

Figure 28. Samples PLA15-1H (A) and PLA15-4H (B) in FE-SEM image. Both samples lack the distinct crustal coating present in other PLA15 samples.

It has been suggested, that local lack of soil Mn, possibly due to Mn scavenging neighbouring nodules, during initial nodule formation can lead to poorly cemented, high Fe/Mn ratio nodules (Schwertmann and Fanning 1976). Later on, these Fe rich nodules can be impregnated with Mn through the nodule pore network (White and Dixon 1996). I suggest this, in combination with the lack of crustal coating, is the case with samples PLA15-1H and PLA15-4H.

FE-SEM identified minor amounts of Mo in samples 1H and 7D, 0.4 wt-% Pb in 4H and minor amounts of V in both 1H and 4H. Sample 9D contains substantial amounts of P, an element known to potentially be absorbed to pedogenic ferromanganese nodules via biotic processes (Table 2, Gasparatos et al. 2019). EDS-SEM results (Appendix A) reveal a spot in sample PLA15-8D, highly enriched in both Fe and Mn (41.00 and 36.00 wt-%, respectively) with 3.42 wt-% of Cu. While FE-SEM was not used to determine the phase association of Cu, organic fraction has been considered the most important carrier of Cu (Salomons et al. 1987) in soils and the theoretical association should be with Fe in nodules (McKenzie 1980). Based on EDS-SEM point analysis, other minor elements that commonly associate with higher Fe content in the PLA15 sample series include Ti, V and P (Appendix A).

Minor amounts of S are observed in several samples with wt-% ranging between 0.1–0.2. The role of S in Fe-Mn nodules is poorly studied. Even though soil S is by and large organically bounded (Eriksen et al. 1998), it is not known whether S in Fe-Mn nodules is purely trapped soil S or whether micro-organisms inside the nodule could make a measurable contribution to the amount of S present in the nodule. In EDS-SEM point measurements, S appears to correlate with elevated Fe content (Appendix A).

6.3.2. Zr7

The textural immaturity defies any reliable use of the development phase interpretation by Yu et al. (2020), but the spatially fairly evenly separated and, compared to the small nodule size, wide Mn rich rings could imply decreased frequency of change in the dominant redox settings, with Mn precipitation happening mostly during periods of increased soil redox potential. The relative scarcity of radial crack and void Mn cementation also suggest primarily direct Mn precipitation with only minor amounts of

Mn translocation through nodule network. However, this could be due to the immaturity of the nodules, as clear evidence of metal translocation can be seen in sample 6D that contains anomalously well enriched zones in a somewhat structureless nodule.

Anomalous among the trend of poorly enriched Fe-Mn nodules in the sample series is the sample Zr7-2H resembling heavily the sample PLA15-4H. The sample 2H is again marked by heavy Mn enrichment in radial void fillings and irregular shape. The presence of a more heavily enriched, highly hydromorphic sample serves as further evidence of the nodule possibly responding to microscale variations in redox settings and initial metal availability.

Both Si and Al are relatively abundant in the sample series (Table 3), while only very small primary Si rich soil mineral fragments are present, the largest mineral fragments, being Fe-heavy, are presumably micas. The appearance of mica fragments into the nodules reflects changing formation environment to one where micas are prevalent, but it has connotations for nodule formation as well. Fe-Mn bearing micas are known to act as sources of metals for proto-nodule formation, and the various weathering products like vermiculite are known to further leach Fe ions for nodule uptake (Šegvić et al. 2018). However, the abundance of other clay minerals reflected by the relatively high Al content (Table 3) could affect the overall compactness (Rhoton et al. 1993) and thus prevent metal translocation within the nodule potentially inhibiting Fe and Mn enrichment.

No heavy metals were measured in any of the Zr7 samples by either FE-SEM or EDS-SEM point analysis (Table 3, Appendix A). S was present in all but one sample. It is noteworthy, however, that the overall poor enrichment of Fe and Mn might promote the mass fraction-based appearance of S in the compositional table.

6.3.3. Zr5

The Zr5 sample series is the most heterogenous of all the sample series in both structure and elemental composition. Two larger samples (> 3 mm, samples 1H and 2H) and several smaller nodules display effectively the difference between samples at different stage of development even within the same paleosol unit. Two largest samples have distinct concentric ring structure with well-defined Fe-Mn distribution (Figure 9). Sample

2H has an Mn enriched interior (Figure 19), while the interior of 1H is relatively poor in both Fe and Mn (Figure 18) but rich in Al (Appendix A). The heavy Mn presence outside the poorly enriched nodule interior in the sample 1H gives credence to the notion of clay minerals affecting the effective porosity for metal translocation. The primary soil mineral fragments, judging by the chemical composition, appear to be both abundant and siliceous in sample 1H and a combination of smaller siliceous fragments and micas in sample 2H.

Fe is mainly located in the central rings of the sample 1H (Figure 18) and on the outer rings of the sample 2H (Figure 19). Sample 2H is much less Fe-Mn enriched but continues to have evenly distributed Mn rich bands between Mn poor bands. 2H however, has a much thicker Fe-heavy band, with minor, unevenly distributed Mn-heavy bands. Using the model by Yu et al. (2015, 2020), a prolonged stay at the Fe precipitation window would precipitate the thick Fe band, while the thin Mn bands are a result of relatively brief periods of more oxidizing soil conditions. The irregularity of the Mn bands suggests also redissolution and translocation as nodule surface is exposed to more reductive conditions. However, unlike the upper Bahe Fm samples, nodules from Lantian Fm lack the prevalent, radial Mn rich pore fill channels indicate lesser duration of the lower Eh Fe precipitation window where Mn remains mobile (White and Dixon 1996). No separation of the crustal coating band is observable in Zr5 samples of any size. Mn presence in the outer coating appears to be tied to the nodule size, with smaller nodules commonly having more Fe rich surface, possibly due to most Mn being translocated towards the nodule interior.

The expression of the samples 1H and 2H suggest that it is possible the measurements 6–15 (Figure 18) in sample 1H correspond fairly well with all the measurements of the sample 2H (Figure 19). Both samples share a fairly similar expression, where the nodule interior is high in Mn, but towards the exterior the Mn content dissipates and Fe content increases. Mn is present as mainly thinner bands and as very modest pore fills in the mid-nodule, suggesting enhanced co-deposition due to rapidly altering soil redox conditions (Yu et al. 2020). Sample 1H possesses a large, Mn rich outer layer that is not yet developed on the sample 2H. All in all, the general expression of 2H and the interior of 1H largely resemble that of phase 3 in the growth phase model of sample PLA15-2H (Figure 26).

The formation and enrichment rate are highly dependable on the porosity (Yu et al. 2015) and information about the amount of pore fill and the lack thereof would be needed to differentiate between co-precipitation of Fe and Mn and pore space filling with Mn. Likewise, the porosity information would be necessary to estimate the effects of maturity between two differently sized samples. If higher degree of porosity is observed in the central bands of sample 2H, it would suggest that the nodule is still maturing and that the observations are not comparable.

Smaller samples of the Zr5 bear striking similarity to samples of similar size from the series Zr7. All are poorly enriched and have a relatively even spread of Fe compared to Mn (Figure 29). The interpretational model of Yu et al. (2020) is not readily applicable to samples with somewhat stable Fe precipitation, but the thickness of the Mn bands suggests a prolonged period of increased soil redox potential.

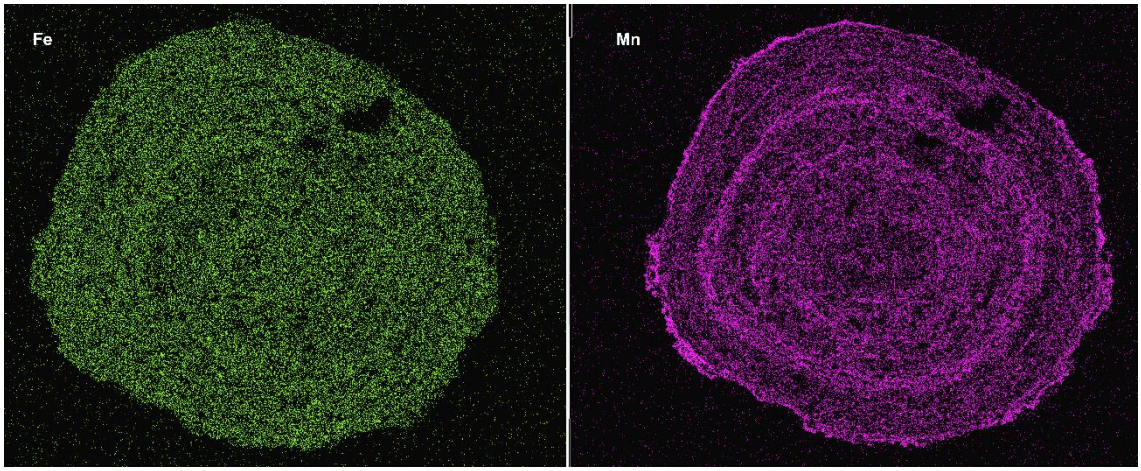

Figure 29. Side-by-side comparison of Fe and Mn distribution in the sample Zr5-6H.

It is notable, that most of the samples in the series contained no S (Table 4). This observation is suspect due to S being present in only the four thick section samples and missing from the thin section samples. However, Zr5-H samples suffered very little degradation and S has been present in both thin and thick section samples in both Zr7 and PLA15. This could possibly suggest soil S depravation through plant uptake, known to take place in light soils with thick vegetative coverage (Eriksen et al. 1998).

Sample Zr5-8D is anomalously rich in Fe, having the highest Fe content of all samples studied (16.1 wt-%). Mn is present only as crack and void fillings. The explanation for

such a high Fe content is not known, but could, speculatively speaking, result from microscale variation in the soil metal availability and redox conditions. Sample 8D contains also V that is strongly associated with Fe in PLA15 samples as well as S, most commonly associated with Fe in all samples (Appendix A). It is also the only sample in the series with any heavy metals detected with FE-SEM or EDS-SEM (Table 4, Appendix A).

6.4. Depositional environment and climate

All nodules have different formation times leading to different degrees of nodule fabric maturity. Nodule size and the number of concentric ring bands directly correlates with the amount of paleosol redox history recorded in the nodule (Yu et al. 2015). While the samples of different sizes are products of the same environment, the distribution of elements cannot be directly compared, as nodule maturation increases both elemental and structural differentiation. Hence, as the timeline of observed redox state changes in nodule fabric and age of nodules cannot be directly compared between nodules even within the same layer, information extraction must happen via trend observations and identification of different phases. Comparing nodules from different depositional environments poses even larger obstacles. In addition to the possible changes in soil chemical composition (mineral content and metal availability, grain size, porosity), one would have to also have a working estimate of the paleosol pH (Negra et al. 2005, Cornu et al. 2009, Szymański and Skiba 2013). Most importantly, however, the main drivers of soil redox state changes must be comparable.

PLA15 samples originate from a layer of floodplain sediments and while the amount of flooding and fluvial influence in the soil is certainly tied to precipitation, the expected flooding of the environment exposes nodules to highly reductive conditions that enhances the mobility of various metals depending on pH settings (Frohne et al. 2011). PLA15 samples from the upper Bahe Fm have, on average, the highest concentration of Fe in all the samples as well as highest concentrations of heavy metals. Water saturation during flooding changes the soil environment from aerobic to anaerobic for extended periods and the soil environment goes through many, often biologically catalysed reactions such as denitrification, Mn(IV) reduction, Fe(III) reduction, SO_4(-II) reduction and

methanogenesis (Patrick and Jugsujinda 1992). Heavily anaerobic conditions ensure the wide availability of metal cations and the prolonged, low Eh conditions allow for precipitation of high amounts of Fe as well as extensive Mn translocation via the nodule pore network (Yu et al. 2015).

These are features that can be tied to nodule formation taking place either in just above or at the highly redox sensitive oxic-anoxic interface layer (Salomons et al. 1987). The anoxic layer and overlaying oxic-anoxic interface layer may play a significant role in the upwards flux of heavy metals from the anoxic zone to the interface layer, where metals are trapped via inclusion in precipitates or to the oxic zones, where heavy metals may be trapped to Fe and Mn oxides via sorption (Du Laing et al. 2009). This, in conjunction with the increased Fe and Mn enrichment, could contribute the observed higher heavy metal concentrations in the samples.

While the poor drainage of low oxygen water from above the dense subsoil typical to stagnasols (IUSS WG WRB 2015) gives ample time window for Fe precipitation and Mn translocation in lower Eh conditions, the height of the oxic-anoxic interface layer is subject to change with time in the soil profile (Du Laing et al. 2007). The implication is that the precipitation signal present in floodplain Fe-Mn nodules is further obfuscated by the changes in the water table and drainage rates affecting the location of the oxic-anoxic interface layer. Furthermore, the possibility of PLA15 samples not being internally consistent in regard to the redox signal cannot be ruled out due to the long formation times of nodules. During periods of minor or non-flooding, the nodule formation may be more affected by direct precipitation. Shifting of the river channel can also affect nodule formation, as floodplain soil pH has been shown to increase with distance to the flooding river (Pahlavan-Rad and Akbarimoghaddam 2018). Dissolution of Fe in various Eh settings is controlled by pH, with dissolution happening in far less reductive settings as pH approaches neutrality (Frohne et al. 2011).

I propose that the formation of the redoximorphic features in the PLA15 nodules from upper Bahe Fm is primarily governed by changes in the flooding regime and soil oxic-anoxic interface depth, and that the increased hydromorphism is not directly due to higher precipitation. The Mn rich outer layers of the nodules imply that the formation possibly ended as Fe reductive conditions became less frequent as flooding regime subsided. It is

possible that the relative influence of flooding and direct meteoric precipitation has varied during nodule formation, leading to the observed changes in the Fe-Mn precipitation regime. The high amount of Mn crack and void fills present in PLA15 samples also suggest larger biotic component enhancing the nodule Fe-Mn enrichment and highlights the needs for measuring the carbon content of nodules to better estimate the amount of biotic enrichment.

Zr5 and Zr7 samples pose some potential for cross correlation. Nodules of the same size are remarkably similar in both structure and chemical composition and have been collected from similar soil elements. Both sample series host Fe rich, presumably mica fragments typical to 'Red Clay' sediments (Hu et al. 2009). The similarity of appearance suggest similar pathways of formation, meaning both sample series likely have had some influence from weathering of micas and leaching from mica weathering products (Šegvić et al. 2018). The fluvial overprint present in the sedimentological characteristics of topmost Bahe Fm does not appear to differentiate nodules from those of the eolian deposits in Lantian Fm, although fluvial contribution to the soil redox regime cannot be ruled out, especially due to the presence of highly hydromorphic sample Zr7-2H.

The soil redox state changes of both Zr series of samples are likely driven primarily by changes in precipitation and as such, they also pose the highest potential to estimate differences in precipitation during their respective times of formation. The interpretation is, however, stymied by the lack of information present in Zr7 samples. As no nodules of larger size were available, the samples contain little information on the changes and the possible ultimate expression of the nodules. All nodules of both Zr series suggest relatively low magnitude but higher frequency variance in prevailing soil redox conditions. This is in agreement with soil redox conditions being primarily controlled by meteoric precipitation. However, due to the lack of nodule porosity data, it is impossible to reliably differentiate between co-precipitation of rapidly alternating redox settings and higher frequency altering of the dominant precipitation windows.

The possibility of other variables existing between samples Zr5 and Zr7 has to also be considered. Red clay ultisols are typically acidic with a pH of ~5 (Xu et al. 2012, IUSS WG WRB, 2015) due to the leaching of carbonates by precipitation. Zr5 samples have been collected under a thick caliche layer, whereas no such layer is present at the topmost

Bahe Fm sediments, however, the strata does bear carbonates not visible to the naked eye (Kaakinen, personal comm. 2020). The caliche layer is indicative of very high precipitation, but its effect to the soil pH in Lantian study area and thus the Eh required for Fe dissolution is not known. However, the late dating of the caliche layer to the Pliocene–Pleistocene boundary (Kaakinen, personal comm. 2020) suggest reduced rates of eolian sediment deposition, which has the potential to greatly prolong the formation times of the nodules from Lantian Fm, thus potentially being the cause of increased hydromorphism in the larger Zr5 samples. The effects caused by differences in vegetation coverage are also not known. The lesser prevalence of S in Zr5 compared Zr7 samples could suggest higher S uptake by vegetation during formation of Zr5 nodules.

Speculatively, the relatively even Fe distribution and poorly enriched Mn bearing bands of smaller Fe-Mn nodules from the Bahe Fm and the Lantian Fm could be an expression typical to early-development nodules in Fe abundant ‘Red Clay’ sediments and that the lack of larger nodules in the topmost Bahe Fm is indeed indicative of either lesser precipitation or lesser duration of increased precipitation. Yu and Lu (2016) described Fe-Mn nodules from Quaternary red earth sections in Eastern China that show an abundance of hydromorphic features in very large nodules, much like the larger nodules found in Lantian Fm. These nodules were formed roughly 1 060 km SE of Lantian where climate is both warmer and more humid (Yu and Lu 2016). Then the lack of large nodules with well matured hydromorphic features in topmost Bahe Fm sediments could be a result of the relative rarity of precipitation induced redox states suitable for nodule development.

The appearance of eolian sediments implicate a major turnover in the depositional regime during the time of formation of the topmost Bahe Fm nodules. The EASM begun to intensify after 8 Ma (Ding et al. 2001, An et al. 2001, Guo et al. 2002, Zhao et al. 2020) and coincided with the beginning of ‘Red Clay’ deposition (An et al. 2001, Guo et al. 2002). All these events roughly coincide with the formation of the Zr7 series of samples. Although highly speculative and subject to change if more developed nodules from the strata are discovered, the lack of hydromorphic features could imply either shorter formation time or lesser precipitation compared to the more modern sample series from in the Lantian Fm. The EASM intensity reconstructions largely consider the time period

of 7.7 Ma to have increased in monsoon intensity compared to 14–8 Ma ago, but still lesser than during Late Pliocene (Wang et al. 2019).

During the formation of Zr5 samples, some 3.7 Ma ago, further intensification of the EASM took place. The exact timing of this intensification is unclear, with estimates ranging between 3.6 Ma (An et al. 2001) and 4.1 Ma (Wang et al. 2019). The presence of the thick caliche layer just above the location of the Lantian Fm nodules is direct evidence of intense precipitation and evaporation, so the increase of hydromorphic features in Fe-Mn nodules correlates well with both the carbonate features of the soil as well as the time frame of the EASM intensification.

6.5. Use of Fe-Mn nodules as paleoclimatic indicators

In 2001, Stiles et al. showed a very promising positive correlation between the total Fe content (Fe_{TOT}) of ferromanganese nodules and mean annual precipitation (MAP). An inverse and more subdued trend was also observed from $Mn_{TOT.}$ Regression analysis of mean Fe_{TOT} versus MAP yielded an equation that was turned into a predictive model to solve for MAP from nodule Fe_{TOT} that yielded results within 3.5 % of instrumentally measured MAP during formation of modern nodules (Stiles et al. 2001). This possible paleoprecipitation proxy has not been tested outside of the original study.

While the foundational premise of increased Fe enrichment due to lower soil redox regime is sound, the proxy proposed by Stiles et al. (2001) comes with several difficulties and uncertainties. It relies on finding contemporary nodules from biogeochemically matching soils and does not account for possible changes in soil water chemistry. More importantly, the literature (Gasparatos 2012, Yu et al. 2015, Sipos et al. 2016) and the results of this study indicate that relative ratios of Fe and Mn enrichment change as the nodule matures. Also, the studied nodules of similar size from both floodplain deposits and eolian deposits, with likely very different redox regimens, have strikingly similar chemical compositions. This does not rule out the possibility of the proxy being viable, but it should be tested in further studies by using nodules of various size classes and similar enrichment factors from several, precipitation controlled modern redoximorphic soils where rates of precipitation during time of formation can be more accurately estimated.

Nodules that are formed in soil environments where meteoric precipitation is the only driver of soil redox state changes pose the largest potential for paleoclimatological analysis. Currently the formation model by Yu et al. (2020) is largely limited to observing the rate of changes in dominant redox settings during the loosely defined time frame of nodule formation and is only applicable to large, texturally mature nodules. The model cannot be reliably implemented without information on the nodule internal porosity, surrounding soil matrix composition and nodule mineral composition that can distinguish between wider soil redox-induced precipitation and mineral effects on local precipitation (Schwertmann and Taylor 1989, Krishnamurti and Huang 1998).

It is possible, that even within precipitation controlled redoximorphic soils, the variance in depositional conditions and sub-environments will prevent reliable cross correlation of nodules from different time periods. The uncertainty caused by changing rates of deposition poses to significantly affect the ultimate expression present in the nodules.

Relatively little is also known about redox conditions and redox gradient within the nodule. Yu et al. (2015) take an approach that the nodule acts as a nucleus of high redox potential due to the kinetic resistance to reducibility, soliciting surface precipitation of Fe and Mn ions. This model supposes that reduction and redissolution of nodule oxides only takes place at the surface of the nodule as it is exposed to more reductive conditions. Porosity observations can thus be used to estimate the amount of metal translocation towards the nodule interior. However, as total lack of porosity is seldom observed (Yu et al. 2015) it may be that apart from Mn pore fill during Fe-precipitation conditions, the entropy reduction in the nodule interior is almost entirely biologically mediated (Tebo et al. 2004, Timofeeva et al. 2014) and that the purely abiotic translocation of metals only takes place within the very surface of the nodule. Thus, without a working understanding on the dynamics and spatial extent of the possible redox gradient as well as the controls and spatial extent of biotic processes, differentiation between nodule final expression and a nodule that is still in the process of maturing remains problematic.

7. CONCLUSIONS

The studied Fe-Mn nodules from three different time windows (8.07 Ma, 7.7 Ma and 3.7 Ma) show degrees of hydromorphism and differing elemental composition. Observations made using FE-SEM elemental mapping and EDS-SEM point analysis can be used to estimate the formation history of the nodules, but the uncertainty is high due to the lack of nodule porosity and mineralogical data. The structure and chemical composition of the nodule is heavily impacted by the local depositional environment.

The oldest samples from floodplain sediments of the Bahe Fm are highly Fe and Mn enriched and display apparent changes in the dominant soil redox state. However, these nodules are likely mainly influenced by the flooding regime and the highly reductive settings of floodplain soils and cannot be directly compared to nodules from other depositional environments to reconstruct changes in precipitation.

Samples from partly eolian deposits in topmost Bahe Fm and purely eolian deposits in Lantian Fm have mostly very similar chemical composition and structure, but the older Bahe Fm nodules lack larger samples with well-developed hydromorphic structure. Sample observations imply changes of higher frequency but lesser magnitude in the soil redox regime. The formation of both nodule horizons roughly coincides with periods of monsoon intensification and the increased hydromorphism in the more modern Lantian samples could be explained by higher precipitation. However, the uncertain effects of the fluvial overprint on the topmost Bahe Fm nodule formation and the possibly greatly reduced rate of sedimentation during the late Lantian Fm deposition can greatly affect the nodule expression and prevent direct comparison between the two series of samples.

The potential to cross-correlate Fe-Mn nodules from the eolian sediment horizons exists but is limited by the aforementioned uncertainties and small sample count from the topmost Bahe Fm sediments. Greatly increasing the sample count from topmost Bahe Fm and adding, if possible, larger samples would be necessary for the attempt to be viable. The samples should be strictly controlled by soil matrix chemical composition, sediment deposition rates and separated into comparable size groups. The internal porosity and mineralogical structure should be mapped to reduce uncertainty and assist interpretation.

For Fe-Mn nodules to mature into a reliable tool of paleoclimatic analysis, more robust information about nodules from different settings and in different points of formation is needed. While most studies take into accord the surrounding soil environment, a comprehensive review of nodule features and formation settings would have the potential to shed new light on Fe-Mn nodule based paleosol redox reconstructions. Every nodule should be described by their pedogenic environment, enrichment factor in regard to host soil, estimated or measured precipitation, nodule porosity and both bulk and structural elemental composition including C, S and P to reliably compare formation of nodules in different settings.

8. ACKNOWLEDGMENTS

I would like to thank my supervisors Anu Kaakinen, Juha Karhu and Joonas Wasiljeff for their support and input. Anu Kaakinen for her invaluable knowledge on the sedimentology of the CLP and her willingness to answer my questions on any hour. Juha Karhu for his attention to geochemistry and ability to focus on relevant questions and details. And Joonas Wasiljeff for extensively discussing and trying out different measurement techniques with me. I also want to thank the visual standard bearer of this thesis, Piritta Stark, whose input improved the aesthetics of this work. Lastly, I want to thank the internet for being full of pictures of sailing boats.

9. REFERENCES

Aide, M. 2005. Elemental Composition of Soil Nodules from Two Alfisols on an Alluvial Terrace in Missouri. Soil Science, 170, 1022–1033, doi: 10.1097/01.ss.0000187351.16740.55

AM Online Projects 2020. Climate Data for Cities Worldwide. AM Online Projects. Visited on 15.4.2020 https://en.climate-data.org/

An, Z., Kutzbach, J.E., Prell, W.L. and Porter, S.C. 2001. Evolution of Asian Monsoons and Phased Uplift of the Himalaya-Tibetan Plateau Since Late Miocene Times. Nature, 411, 62–66, doi: 10.1038/35075035

An, Z., Huang, Y., Liu, W., Guo, Z., Clemens, S., Li, L., Prell, W., Ning, Y., Cai, Y., Zhou, W., Lin, B., Zhang, Q., Cao, Y., Qiang, X., Chang, H. and Wu, Z. 2005. Multiple Expansions of C_4 plant Biomass in East Asia Since 7 Ma Coupled with Strengthened Monsoon Circulation. Geology, 33, 705–708, doi: 10.1130/G21423.1

Blume, H., Brümmer, G.W., Fleige, H., Horn, R., Kandeler, E., Kretzschmar, R., Kögel-Knabner, I., Stahr, K. and Wilke, B.-M. 2016. Scheffer/Schachtschabel Soil Science. Springer, Berlin, 618 p.

Cai, M., Wei, M., Xu, D., Miao, Y., Wu, F. and Pan, B. 2013. Vegetation and Climate Changes During Three Interglacial Periods Represented in the Luochuan Loess-Paleosol Section, on the Chinese Loess Plateau Quaternary International, 296, 131–140, doi: 10.1016/j.quaint.2012.06.041

Cerling, T.E. 1984. The Stable Isotopic Composition of Modern Soil Carbonate and Its Relationship to Climate. Earth and Planetary Science Letters, 71, 229–240, doi: 10.1016/0012-821X(84)90089-X

Chen, C., Bai, Y., Fang, X., Guo, H., Meng, Q., Zhang, W., Zhou, P. and Murodov, A. 2019. A Late Miocene Terrestrial Temperature History for the Northeastern Tibetan Plateau's Period of Tectonic Expansion. Geophysical Research Letters, 46, 8375–8386, doi: 10.1029/2019GL082805

Chen, F., Xu, Q., Chen, J., Birks, H.J.B., Liu, J., Zhang, S., Jin, L., An, C., Telford, R.J., Cao, X., Wang, Z., Zhang, X., Selvaraj, K., Lu, H., Li, Y., Zheng, Z., Wang, H., Zhou, A., Dong, G., Zhang, J., Huang, X., Bloemendal, J. and Rao, Z. 2015. East Asian Summer Monsoon Precipitation Variability Since the Last Deglaciation. Scientific Reports, 5, 11186, doi: 10.1038/srep11186

Childs, C.W. 1975, Composition of Iron-Manganese Concretions from Some New Zealand Soils. Geoderma, 13, 141–152, doi: 10.1016/0016-7061(75)90063-4

Christensen, J.H., Krishna Kumar, K., Aldrian, E., An, S., Cavalcanti, I.F.A., de Castro, M., Dong, W., Goswami, P., Hall, A., Kanyanga, J.K., Kitoh, A., Kossin, J., Lau, N., Renwick, J., Stephenson, D.B., Xie, S. and Zhou, T. 2013. Climate Phenomena and Their Relevance for Future Regional Climate Change. In: Stocker, T.F., Qin, D., Plattner, G.-K., Tignor, M.M.B., Allen, S.K., Boschung, J., Nauels, A., Xia, Y., Bex, V. and Midgley, P.M. (eds.) Climate Change 2013: The Physical Science Basis. Contribution of Working Group I to the Fifth Assessment Report of the Intergovernmental Panel on Climate Change. Cambridge University Press, 1217–1308.

Clift, P.D., Hodges, K.V., Heslop, D., Hannigan, R., Van Long, H. and Calves, G. 2008. Correlation of Himalayan Exhumation Rates and Asian Monsoon Intensity. Nature Geoscience, 1, 875–880, doi: 10.1038/ngeo351

Clift, P.D., Wan, S. and Blusztajn, J. 2014. Reconstructing Chemical Weathering, Physical Erosion and Monsoon Intensity Since 25 Ma in the Northern South China Sea: A Review of Competing Proxies. Earth-Science Reviews, 130, 86–102, doi: 10.1016/j.earscirev.2014.01.002

Cornu, S., Cattle, J.A., Samouelian, A., Laveuf, C., Guilherme, L.R.G. and Albéric, P. 2009. Impact of Redox Cycles on Manganese, Iron, Cobalt, and Lead in Nodules. Soil Science Society of America Journal, 73, 1231–1241, doi: 10.2136/sssaj2008.0024

Cornu, S., Deschatrettes, V., Salvador-Blanes, S., Clozel, B., Hardy, M., Branchut, S. and Le Forestier, L. 2005. Trace Element Accumulation in Mn-Fe-Oxide Nodules of a Planosolic Horizon. Geoderma, 125, 11–24, doi: 10.1016/j.geoderma.2004.06.009

D'Amore, J.J., Al-Abed, S.R., Scheckel, K.G. and Ryan, J.A. 2005. Methods for Speciation of Metals in Soils. Journal of Environmental Quality, 34, 1707–1745, doi: 10.2134/jeq2004.0014

Deines, P. 1980. The Isotopic Composition of Reduced Organic Carbon. In: Fritz, P. and Fontes, J.C. (eds.) Handbook of Environmental Isotope Geochemistry, Vol 1: The Terrestrial Environment. Elsevier, Amsterdam, 329–406, doi: 10.1016/B978-0-444-41780-0.50015-8

Du, J., Li, D., Wang, Y. and Ma, Y. 2017. Late Quaternary Activity of the Huashan Piedmont Fault and Associated Hazards in the Southeastern Weihe Graben, Central China. Acta Geologica Sinica, 91, 76–92, doi: 10.1111/1755-6724.13064

Du Laing, G., Rinklebe, J., Vandecasteele, B., Meers, E. and Tack, F.M.G. 2009. Trace Metal Behaviour in Estuarine and Riverine Floodplain Soils and Sediments: A Review. Science of the Total Environment, 407, 3972–3985, doi: 10.1016/j.scitotenv.2008.07.025

Du Laing, G., Vanthuyne, D.R.J., Vandecasteele, B., Tack, F.M.G. and Verloo, M.G. 2007. Influence of Hydrological Regime on Pore Water Metal Concentrations in a Contaminated Sediment-Derived Soil. Environmental Pollution, 147, 615–625, doi: 10.1016/j.envpol.2006.10.004

Duliu, O.G., Tufan, M.S. and Szobotka, S.A. 1997. Computer Axial Tomography Investigation of Polymetallic Nodules. Marine Geology, 138, 303–311.

Ehleringer, J.R., Cerling, T.E. and Helliker, B.R. 1997. C_4 Photosynthesis, Atmospheric CO_2, and Climate. Oecologia, 112, 285–299, doi: 10.1007/s004420050311

Elberling, B., Breuning-Madsen, H. and Knicker, H. 2013. Carbon Sequestration in Iron-Nodules in Moist Semi-Deciduous Tropical Forest Soil. Geoderma, 200–201, 202–207, doi: 10.1016/j.geoderma.2013.03.001

Eriksen, J., Murphy, M. and Schnug, E. 1998. The Soil Sulphur Cycle. In: Schnug, E. (eds.) Sulphur in Agroecosyslems. Kluwer Academic Publishers, Dordrecht, 39–73, doi: 10.1007/978-94-011-5100-9

Estes, E.R., Andeer, P.F., Nordlund, D., Wankel, S.D. and Hansel, C.M. 2017. Biogenic Manganese Oxides as Reservoirs of Organic Carbon and Proteins in Terrestrial and Marine Environments. Geobiology, 15, 158–172, doi: 10.1111/gbi.12195

Ettler, V., Chren, M., Mihaljevič, M., Drahota, P., Kříbek, B., Veselovský, F., Sracek, O., Vaněk, A., Penížek, V., Komárek, M., Mapani, B. and Kamona, F. 2017. Characterization of Fe-Mn Concentric Nodules from Luvisol Irrigated by Mine Water in a Semi-Arid Agricultural Area. Geoderma, 299, 32–42, doi: 10.1016/j.geoderma.2017.03.022

Flower, B.P. and Kennett, J.P. 1994. The Middle Miocene Climatic Transition: East Antarctic Ice Sheet Development, Deep Ocean Circulation and Global Carbon Cycling. Palaeogeography, Palaeoclimatology, Palaeoecology, 108, 537–555. doi: 10.1016/0031-0182(94)90251-8

Frohne, T., Rinklebe, J., Diaz-Bone, R.A. and Du Laing, G. 2011. Controlled Variation of Redox Conditions in a Floodplain Soil: Impact on Metal Mobilization and Biomethylation of Arsenic and Antimony. Geoderma, 160, 414–424, doi: 10.1016/j.geoderma.2010.10.012

Fu, B., Wang, S., Liu, Y., Liu, J., Liang, W. and Miao, C. 2017. Hydrogeomorphic Ecosystem Responses to Natural and Anthropogenic Changes in the Loess Plateau of China. Annual Review of Earth and Planetary Sciences, 45, 223–243, doi: 10.1146/annurev-earth-063016-020552

Gai, C., Liu, Q., Roberts, A.P., Chou, Y., Zhao, X., Jiang, Z. and Liu, J. 2020. East Asian Monsoon Evolution Since the Late Miocene from the South China Sea. Earth and Planetary Science Letters, 530, 115960, doi: 10.1016/j.epsl.2019.115960

Gasparatos, D. 2007. Genesis of Fe-Mn Concretions and Nodules in Alfisols of Thessaly. PhD-thesis. Agricultural University of Athens, Department of Natural Resources Management and Agricultural Engineering, 275 p.

Gasparatos, D. 2012. Fe–Mn Concretions and Nodules to Sequester Heavy Metals in Soils. In: Lichtfouse, E., Schwarzbauer, J. and Robert, D. (eds.) Environmental Chemistry for a Sustainable World, Vol 1. Springer, Dordrecht, 443-474, doi: 10.1007/978-94-007-2439-6_11

Gasparatos, D., Massas, I. and Godelitsas, A. 2019. Fe-Mn Concretions and Nodules Formation in Redoximorphic Soils and Their Role on Soil Phosphorus Dynamics: Current Knowledge and Gaps. Catena, 182, 104106, doi: 10.1016/j.catena.2019.104106

Gasparatos, D., Tarenidis, D., Haidouti, C. and Oikonomou, G. 2005. Microscopic Structure of Soil Fe-Mn Nodules: Environmental Implication. Environmental Chemistry Letters, 2, 175–178, doi: 10.1007/s10311-004-0092-5

Golden, D.C., Chen, C.C., Dixon, J.B. and Tokashiki, Y. 1988. Pseudomorphic Replacement of Manganese Oxides by Iron Oxide Minerals. Geoderma, 42, 199–211, doi: 10.1016/0016-7061(88)90001-8

Goldstein, J.I., Newbury, D.E., Joy, D.C., Lyman, C.E., Echlin, P., Lifshin, E., Sawyer, L. and Michael, J.R. 2003. Scanning Electron Microscopy and X-Ray Microanalysis. 3rd edition. Springer, New York, 689 p.

Guo, Z., Ruddiman, W., Hao, Q., Wu, H.B., Qiao, Y., Zhu, R., Peng, S., Wei, J.J., Yuan, B.Y. and Liu, T.S. 2002. Onset of Asian Desertification by 22 Myr Ago Inferred from Loess Deposits in China. Nature, 416, 159–163, doi: 10.1038/416159a

Guo, Z.T., Sun, B., Zhang, Z.S., Peng, S.Z., Xiao, G.Q., Ge, J.Y., Hao, Q.Z., Qiao, Y.S., Liang, M.Y., Liu, J.F., Yin, Q.Z. and Wei, J.J. 2008. A Major Reorganization of Asian Climate by the Early Miocene. Climate of the Past, 4, 153–174, doi: 10.5194/cp-4-153-2008

Hess, S. and Kuhnt, W. 2005. Neogene and Quaternary Paleoceanographic Changes in the Southern South China Sea (Site 1143): The Benthic Foraminiferal Record. Marine Micropaleontology, 54, 63–87, doi: 10.1016/j.marmicro.2004.09.004

Hönisch, B., Hemming, N.G., Archer, D., Siddall, M. and McManus, J.F. 2009. Atmospheric Carbon Dioxide Concentration Across the Mid-Pleistocene Transition. Science, 324, 1551–1555, doi: 10.1126/science.1171477

Hu, X., Xu, L., Pan, Y. and Shen, M. 2009. Influence of the Aging of Fe Oxides on the Decline of Magnetic Susceptibility of the Tertiary Red Clay in the Chinese Loess Plateau. Quaternary International, 209, 22–30, doi: 10.1016/j.quaint.2009.02.019

Huang, L., Hong, J., Tan, W., Hu, H., Liu, F. and Wang, M. 2008. Characteristics of Micromorphology and Element Distribution of Iron-Manganese Cutans in Typical Soils of Subtropical China. Geoderma, 146, 40–47, doi: 10.1016/j.geoderma.2008.05.007

IUSS Working Group WRB 2015. World Reference Base for Soil Resources 2014: International Soil Classification System for Naming Soils and Creating Legends for Soil Maps, Update 2015. Food and Agriculture Organization of United Nations, World Soil Resources Reports No: 106, 192 p.

Janis, C.M. 1993. Tertiary Mammal Evolution in the Context of Changing Climates, Vegetation, and Tectonicc Events. Annual Review of Ecology, Evolution, and Systematics, 24, 467–500.

Jarvis, A., Reuter, H.I., Nelson, A. and Guevara, E. 2008. Hole-Filled Seamless SRTM Data V4. International Centre for Tropical Agriculture. Visited on 14.5.2020. http://srtm.csi.cgiar.org/

Jiang, H. and Ding, Z. 2008. A 20 Ma Pollen Record of East-Asian Summer Monsoon Evolution from Guyuan, Ningxia, China. Palaeogeography, Palaeoclimatology, Palaeoecology, 265, 30–38, doi: 10.1016/j.palaeo.2008.04.016

Jien, S., Hseu, Z. and Chen, Z. 2010. Hydropedological Implications of Ferromanganiferous Nodules in Rice-Growing Plinthitic Ultisols Under Different Moisture Regimes. Soil Science Society of America Journal, 74, 880–891, doi: 10.2136/sssaj2009.0020

Kaakinen, A. 2005. A Long Terrestrial Sequence in Lantian – a Window into the Late Neogene Palaeoenvironments of Northern China. PhD-thesis. University of Helsinki, Department of Geology D4, 49 p.

Kaakinen, A. and Lunkka, J.P. 2003. Sedimentation of the Late Miocene Bahe Formation and Its Implications for Stable Environments Adjacent to Qinling Mountains in Shaanxi, China. Journal of Asian Earth Sciences, 22, 67–78, doi: 10.1016/S1367-9120(03)00044-0

Kaakinen, A., Sonninen, E. and Lunkka, J.P. 2006. Stable Isotope Record in Paleosol Carbonates from the Chinese Loess Plateau: Implications for Late Neogene Paleoclimate and Paleovegetation. Palaeogeography, Palaeoclimatology, Palaeoecology, 237, 359–369, doi: 10.1016/j.palaeo.2005.12.011

Krishnamurti, G.S.R. and Huang, P.M. 1989. Influence of Mn^{2+} and pH on the Formation of Iron Oxides from Ferrous Chloride and Ferrous Sulfate Solutions. Clays and Clay Minerals, 37, 451–458, doi: 10.1346/CCMN.1989.0370509

Liu, F., Colombo, C., Adamo, P., He, J.Z. and Violante, A. 2002. Trace Elements in Manganese–Iron Nodules from a Chinese Alfisol. Soil Science Society of America Journal, 66, 661–670, doi: 10.2136/sssaj2002.6610

Liu, G. 1999. Soil Conservation and Sustainable Agriculture on the Loess Plateau: challenges and prospects. Ambio, 28, 663–668.

Liu, J., Chen, X., Shi, W., Chen, P., Zhang, Y., Hu, J., Dong, S. and Li, T. 2019. Tectonically Controlled Evolution of the Yellow River Drainage System in the Weihe Region, North China: Constraints from Sedimentation, Mineralogy and Geochemistry. Journal of Asian Earth Sciences, 179, 350–364, doi: 10.1016/j.jseaes.2019.05.008

Liu, J., Zhang, P., Lease, R.O., Zheng, D., Wan, J., Wang, W. and Zhang, H. 2013. Eocene Onset and Late Miocene Acceleration of Cenozoic Intracontinental Extension in the North Qinling Range - Weihe Graben: Insights from Apatite Fission Track Thermochronology. Tectonophysics, 584, 281–296, doi: 10.1016/j.tecto.2012.01.025

Liu, L., Eronen, J.T. and Fortelius, M. 2009. Significant Mid-Latitude Aridity in the Middle Miocene of East Asia. Palaeogeography, Palaeoclimatology, Palaeoecology, 279, 201–206, doi: 10.1016/j.palaeo.2009.05.014

Liu, W., Huang, Y., An, Z., Clemens, S.C., Li, L., Prell, W.L. and Ning, Y. 2005. Summer Monsoon Intensity Controls C4/C3 Plant Abundance During the Last 35 ka in the Chinese Loess Plateau: Carbon Isotope Evidence from Bulk Organic Matter and Individual Leaf Waxes. Palaeogeography, Palaeoclimatology, Palaeoecology, 220, 243–254, doi: 10.1016/j.palaeo.2005.01.001

Lu, H. and Guo, Z. 2014. Evolution of the Monsoon and Dry Climate in East Asia During Late Cenozoic: A Review. Science China Earth Sciences, 57, 70–79, doi: 10.1007/s11430-013-4790-3

McKenzie, R.M. 1980. The Adsorption of Lead and Other Heavy Metals on Oxides of Manganese and Iron, Australian Journal of Soil research, 18, 61–73, doi: 10.1071/sr9800061

McKenzie, R.M. 1989. Manganese Oxides and Hydroxides. In: Dixon, G.B. and Weed, S.B. (eds.) Minerals in Soil Environments. 2nd edition. Soil Science Society of America, Madison, 439–466.

Manceau, A., Tamura, N., Celestre, R.S., Macdowell, A.A., Geoffroy, N., Sposito, G. and Padmore, H.A. 2003. Molecular-Scale Speciation of Zn and Ni in Soil Ferromanganese Nodules from Loess Soils of the Mississippi Basin. Environmental Science & Technology, 37, 75–80, doi: 10.1021/es025748r

Manceau, A., Tamura, N., Marcus, M.A., Macdowell, A.A., Celestre, R.S., Sublett, R.E., Sposito, G. and Padmore, H.A. 2002. Deciphering Ni Sequestration in Soil Ferromanganese Nodules by Combining X-Ray Fluorescence, Absorption, and Diffraction at Micrometer Scales of Resolution. American Mineralogist, 87, 1494–1499, doi: 10.2138/am-2002-1028

Natural Earth 2018. Free Vector and Raster Map Data at 1:10m, 1:50m, and 1:110m Scales. Natural Earth. Visited on 14.5.2020. https://www.naturalearthdata.com

Neaman, A., Martínez, C.E., Trolard, F. and Bourrié, G. 2008. Trace Element Associations with Fe- and Mn-Oxides in Soil Nodules: Comparison of Selective Dissolution with Electron Probe Microanalysis. Applied Geochemistry, 23, 778–782, doi: 10.1016/j.apgeochem.2007.12.025

Negra, C., Ross, D.S. and Lanzirotti, A. 2005. Oxidizing Behavior of Soil Manganese: Interactions Among Abundance, Oxidation State, and pH. Soil Science Society of America Journal, 69, 87–95.

Newbury, D.E. and Ritchie, N.W.M. 2013. Is Scanning Electron Microscopy/Energy Dispersive X-Ray Spectrometry (SEM/EDS) Quantitative? Scanning, 35, 141–168, doi: 10.1002/sca.21041

Ostrooumov, M. 2017. Raman and Infrared Reflection Spectroscopic Study of Mineralogical Composition of Iron-Manganese Nodules (Pacific and Indian Oceans). International Journal of Experimental Spectroscopic Techniques, 2, 1–12, doi: 10.35840/2631-505X/8512

Pahlavan-Rad, M.R. and Akbarimoghaddam, A. 2018. Spatial Variability of Soil Texture Fractions and pH in a Flood Plain (Case Study from Eastern Iran). Catena, 160, 275–281, doi: 10.1016/j.catena.2017.10.002

Palumbo, B., Bellanca, A., Neri, R. and Roe, M.J. 2001. Trace Metal Partitioning in Fe-Mn Nodules from Sicilian Soils, Italy. Chemical Geology, 173, 257–269, doi: 10.1016/S0009-2541(00)00284-9

Passey, B.H., Ayliffe, L.K., Kaakinen, A., Zhang, Z., Eronen, J.T., Zhu, Y., Zhou, L., Cerling, T.E. and Fortelius, M. 2009. Strengthened East Asian Summer Monsoons During a Period of High-Latitude Warmth? Isotopic Evidence from Mio–Pliocene Fossil Mammals and Soil Carbonates from Northern China. Earth and Planetary Science Letters, 277, 443–452, doi: 10.1016/j.epsl.2008.11.008

Patrick, W.H., Jr. and Jugsujinda, A. 1992. Sequential Reduction and Oxidation of Inorganic Nitrogen, Manganese, and Iron in Flooded Soil. Soil Science Society of America Journal, 56, 1071–1073, doi: 10.2136/sssaj1992.03615995005600040011x

Pawluk, S. and Dumanski, J. 1973. Ferruginous Concretions in a Poorly Drained Soil of Alberta. Soil Science Society of America Journal, 37, 124–127, doi: 10.2136/sssaj1973.03615995003700010036x

Ram, H., Singh, R.P. and Prasad, J. 2001. Chemical and Mineralogical Composition of Fe-Mn Concretions and Calcretes Occurring in Sodic Soils of Eastern Uttar Pradesh, India. Australian Journal of Soil Research, 39, 641–648, doi: 10.1071/SR98098

Rao, G., Cheng, Y., Yu, Y., Yan, B. and Lin, A. 2017. Tectonic Characteristics of the Lishan Piedmont Fault in the SE Weihe Graben (Central China), as Revealed by the Geomorphological and Structural Analyses. Geomorphology, 282, 52–63, doi: 10.1016/j.geomorph.2017.01.014

Ratschbacher, L., Hacker, B.R., Calvert, A., Webb, L.E., Grimmer, J., McWilliams, M., Ireland, T., Dong, S. and Hu, J. 2003. Tectonics of the Qinling (Central China): Tectonostratigraphy, Geochronology, and Deformation History. Tectonophysics, 366, 1–53, doi: 10.1016/S0040-1951(03)00053-2

Rennert, T., Händel, M., Höschen, C., Lugmeier, J., Steffens, M. and Totsche, K.U. 2014. A NanoSIMS Study on the Distribution of Soil Organic Matter, Iron and Manganese in a Nodule from a Stagnosol. European Journal of Soil Science, 65, 684–692, doi: 10.1111/ejss.12157

Rhoton, F.E., Bigham, J.M. and Schulze, D.G. 1993. Properties of Iron-Manganese Nodules from a Sequence of Eroded Fragipan Soils. Soil Science Society of America Journal, 57, 1386–1392, doi: 10.2136/sssaj1993.03615995005700050037x

Ritchie, N.W.M., Newbury, D.E. and Davis, J.M. 2012. EDS Measurements of X-Ray Intensity at WDS Precision and Accuracy Using a Silicon Drift Detector. Microscopy and Microanalysis, 18, 892–904.

Salomons, W., Rooij, N.M. de, Kerdijk, H. and Bril, J. 1987. Sediments as a Source for Contaminants? Hydrobiologia, 149, 13–30.

Schwertmann, U. and Fanning, D.S. 1976. Iron-Manganese Concretions in Hydrosequences of Soils in Loess in Bavaria. Soil Science Society of America Journal, 40, 731–738, doi: 10.2136/sssaj1976.03615995004000050034x

Schwertmann, U. and Taylor, R.M. 1989. Iron Oxides. In: Dixon, G.B. and Weed, S.B. (eds.) Minerals in Soil Environments. 2nd edition. Soil Science Society of America, Madison, 379–438.

Šegvić, B., Girardclos, S., Zanonia, G., Arbiol González, C., Steimer-Herbet, T. and Besse, M. 2018. Origin and Paleoenvironmental Significance of Fe-Mn Nodules in the Holocene Perialpine Sediments of Geneva Basin, Western Switzerland. Applied Clay Science, 160, 22–39, doi: 10.1016/j.clay.2018.01.027

Shang, Y., Beets, C.J., Tang, H., Prins, M.A., Lahaye, Y., Elsas, R. van, Sukselainen, L. and Kaakinen, A. 2016. Variations in the Provenance of the Late Neogene Red Clay Deposits in Northern China. Earth and Planetary Science Letters, 439, 88–100, doi: 10.1016/j.epsl.2016.01.031

Shen, X., Wan, S., Colin, C., Tada, R., Shi, X., Pei, W., Tan, Y., Jiang, X. and Li, A. 2018. Increased Seasonality and Aridity Drove the C4 Plant Expansion in Central Asia Since the Miocene–Pliocene Boundary. Earth and Planetary Science Letters, 502, 74–83, doi: 10.1016/j.epsl.2018.08.056

Sipos, P., Balázs, R., Bozsó, G. and Németh, T. 2016. Changes in Micro-Fabric and Re-Distribution of Fe and Mn with Nodule Formation in a Floodplain Soil. Journal of Soils and Sediments, 16, 2105–2117, doi: 10.1007/s11368-016-1393-6

Stiles, C.A., Mora, C.I. and Driese, S.G. 2001. Pedogenic Iron-Manganese Nodules in Vertisols: A New Proxy for Paleoprecipitation? Geology, 29, 943–946, doi: 10.1130/0091-7613(2001)029<0943:PIMNIV>2.0.CO;2

Strömberg, C.A.E. 2011. Evolution of Grasses and Grassland Ecosystems. Annual Review of Earth and Planetary Sciences, 39, 517–544, doi: 10.1146/annurev-earth-040809-152402

Sun, X. and Wang, P. 2005. How Old is the Asian Monsoon System? – Palaeobotanical Records from China. Palaeogeography, Palaeoclimatology, Palaeoecology, 222, 181–222, doi: 10.1016/j.palaeo.2005.03.005

Szymański, W. and Skiba, M. 2013. Distribution, Morphology, and Chemical Composition of Fe-Mn Nodules in Albeluvisols of the Carpathian Foothills, Poland. Pedosphere, 23, 445–454, doi: 10.1016/S1002-0160(13)60037-5

Szymański, W., Skiba, M. and Błachowski, A. 2014. Mineralogy of Fe-Mn Nodules in Albeluvisols in the Carpathian Foothills, Poland. Geoderma, 217–218, 102–110, doi: 10.1016/j.geoderma.2013.11.008

Tan, W., Liu, F., Li, Y., Hu, H. and Huang, Q. 2006. Elemental Composition and Geochemical Characteristics of Iron-Manganese Nodules in Main Soils of China. Pedosphere, 16, 72–81, doi: 10.1016/S1002-0160(06)60028-3

Tebo, B.M., Parker, D., Bargar, J.R., Verity, R., Clement, B.G., Webb, S.M., Dick, G.J. and Murray, K.J. 2004. Biogenic Manganese Oxides: Properties and Mechanisms of Formation. Annual Review of Earth and Planetary Science, 32, 287–328.

Timofeeva, Y.O. 2008. Accumulation and Fractionation of Trace Elements in Soil Ferromanganese Nodules of Different Size. Geochemistry International, 46, 260–267, doi: 10.1134/S0016702908030038

Timofeeva, Y.O., Karabtsov, A.A., Semal', V.A., Burdukovskii, M.L. and Bondarchuk, N.V. 2014. Iron-Manganese Nodules in Udepts: The Dependence of the Accumulation of Trace Elements on Nodule Size. Soil Science Society of America Journal, 78, 767–778, doi: 10.2136/sssaj2013.10.0444

Tokashiki, Y., Hentona, T., Shimo, M. and Vidhana Arachchi, L.P. 2003. Improvement of the Succesive Selective Dissolution Procedure for the Separation of Birnessite, Lithiophorite, and Goethite in Soil Manganese Nodules. Soil Science Society of America Journal, 67, 837–843.

Tzou, Y.M., Wang, M.K. and Loeppert, R.H. 2003. Sorption of Phosphate and Cr(VI) by Fe(III) and Cr(III) Hydroxides. Archives of Environmental Contamination and Toxicology, 44, 445–453, doi: 10.1007/s00244-002-2090-6

Vepraskas, M.J. and Lindbo, D.L. 2012. Redoximorphic Features as Related to Soil Hydrology and Hydric Soils. In: Lin, H. (eds.) Hydropedology. Academic Press, Boston, 143–172.

Vidhana Arachchi, L.P., Tokashiki, Y. and Baba, S. 2004. Mineralogical Characteristics and Micromorphological Observations of Brittle/Soft Fe/Mn Concretions from Okinawan Soils. Clays and Clay Minerals, 52, 462–472, doi: 10.1346/CCMN.2004.0520407

Vodyanitskii, Y.N. 2006. The Composition of Fe-Mn Nodules as Determined by Synchrotron X-Ray Analysis (Review of Publications). Eurasian Soil Science, 39, 147–156, doi: 10.1134/S1064229306020050

Wang, B., Zheng, H., He, Z., Wang, P., Kaakinen, A. and Zhou, X. 2014. Middle Miocene Eolian Sediments on the Southern Chinese Loess Plateau Dated by Magnetostratigraphy. Palaeogeography, Palaeoclimatology, Palaeoecology, 411, 257–266, doi: 10.1016/j.palaeo.2014.07.007

Wang, H. and Follmer, L.R. 1998. Proxy of Monsoon Seasonality in Carbon Isotopes from Paleosols of the Southern Chinese Loess Plateau, Geology, 26, 987–991, doi: 10.1130/0091-7613(1998)026<0987:POMSIC>2.3.CO;2

Wang, J. 1987. The Fenwei Rift and Its Recent Periodic Activity. Tectonophysics, 133, 257–275, doi: 10.1016/0040-1951(87)90269-1

Wang, Q., Song, Y. and Li, Y. 2019. Clay Mineralogy of the Upper Miocene–Pliocene Red Clay from the Central Chinese Loess Plateau and Its Paleoclimate Implications. Quaternary International, in press. doi: 10.1016/j.quaint.2019.11.039

Webster, P.J., Magaña, T.N., Palmer, J., Shukla, J., Tomas, R.A., Yanai, M. and Yasunari, T. 1998. Monsoons: Processes, Predictability, and the Prospects for Prediction. Journal of Geophysical Research, 103, 14451–14510

Wei, K. and Kennett, J.P. 1986. Taxonomic Evolution of Neogene Planktonic Foraminifera and Paleoceanographic Relations. Paleoceanography, 1, 67–84, doi: 10.1029/PA001i001p00067

White, G.N. and Dixon, J.B. 1996. Iron and Manganese Distribution in Nodules from a Young Texas Vertisol. Soil Science Society of America Journal, 60, 1254–1262, doi: 10.2136/sssaj1996.03615995006000040042x

Wu, Y., Qiu, S., Fu, S., Rao, Z. and Zhu, Z. 2018. Pleistocene Climate Change Inferred from Multi-Proxy Analyses of a Loess–Paleosol Sequence in China. Journal of Asian Earth Sciences, 154, 428–434, doi: 10.1016/j.jseaes.2017.10.007

Xu, R., Zhao, A., Yuan, J. and Jiang, J. 2012. pH Buffering Capacity of Acid Soils from Tropical and Subtropical Regions of China as Influenced by Incorporation of Crop Straw Biochars. Journal of Soils and Sediments, 12, 494–502, doi: 10.1007/s11368-012-0483-3

Yu, X. and Lu, S. 2016. Micrometer-Scale Internal Structure and Element Distribution of Fe-Mn Nodules in Quaternary Red Earth of Eastern China. Journal of Soils and Sediments, 16, 621–633, doi: 10.1007/s11368-015-1212-5

Yu, X., Fu, Y., Brookes, P.C. and Lu, S. 2015. Insights into the Formation Process and Environmental Fingerprints of Iron-Manganese Nodules in Subtropical Soils of China. Soil Science Society of America Journal, 79, 1101–1114, doi: 10.2136/sssaj2015.01.0049

Yu, X., Wang, Y., Zhou, G., Peng, G., Brookes, P.C. and Lu, S. 2020. Paleoclimatic Fingerprints of Ferromanganese Nodules in Subtropical Chinese Soils Identified by Synchrotron Radiation-Based Microprobes. Chemical Geology, 531, 119357, doi: 10.1016/j.chemgeo.2019.119357

Zachos, J., Pagani, M., Sloan, L., Thomas, E. and Billups, K. 2001, Trends, Rhythms, and Aberrations in Global Climate 65 Ma to Present. Science, 292, 686–693, doi: 10.1126/science.1059412

Zhang, A., Yang, Z., Zhong, J. and Mi, F. 1995. Characteristics of Late Quaternary Activity Along the Southern Border Fault Zone of Weihe Graben Basin. Quaternary International, 25, 25–31, doi: 10.1016/1040-6182(94)P3715-K

Zhang, G., He, J., Liu, F. and Zhang, L. 2014. Iron-Manganese Nodules Harbor Lower Bacterial Diversity and Greater Proportions of Proteobacteria Compared to Bulk Soils in Four Locations Spanning from North to South China. Geomicrobiology Journal, 31, 562–577, doi: 10.1080/01490451.2013.854428

Zhang, M. and Karathanasis, A. 1997. Characterization of Iron-Manganese Concretions in Kentucky Alfisols with Perched Water Tables, Clays and Clay Minerals, 45, 428–439, doi: 10.1346/CCMN.1997.0450312

Zhang, R. and Nie, J. 2017. Goethite Concentration Variations in the Red Clay Sequence on the Chinese Loess Plateau. Geochemistry, Geophysics, Geosystems, 18, 4179–4185, doi: 10.1002/2017GC007148

Zhang, Z., Kaakinen, A., Liu, L., Lunkka, J.P., Sen, S., Gose, W.A., Qiu, Z., Zheng, S. and Fortelius, M. 2013. Mammalian Biochronology of the Late Miocene Bahe Formation In: Wang, X., Flynn, L.J. and Fortelius, M. (eds.) Fossil Mammals of Asia: Neogene Biostratigraphy and Chronology. Columbia University Press, New York, 187–202.

Zhao, H., Qiang, X., Xu, X. and Sun, Y. 2020. Iron Oxide Characteristics of the Chinese Loess - Red Clay Sequences and Their Implications for the Evolution of the East Asian Summer Monsoon Since the Late Oligocene. Palaeogeography, Palaeoclimatology, Palaeoecology, 543, 109604, doi: 10.1016/j.palaeo.2020.109604

Zheng, H., Powell, C.M., Rea, D.K., Wang, J. and Wang, P. 2004. Late Miocene and Mid-Pliocene Enhancement of the East Asian Monsoon as Viewed from the Land and Sea. Global and Planetary Change, 41, 147–155, doi: 10.1016/j.gloplacha.2004.01.003

APPENDIX A: EDS-SEM POINT MEASUREMENTS

Sample: PLA15-1H 10.10.2019 13:51:56

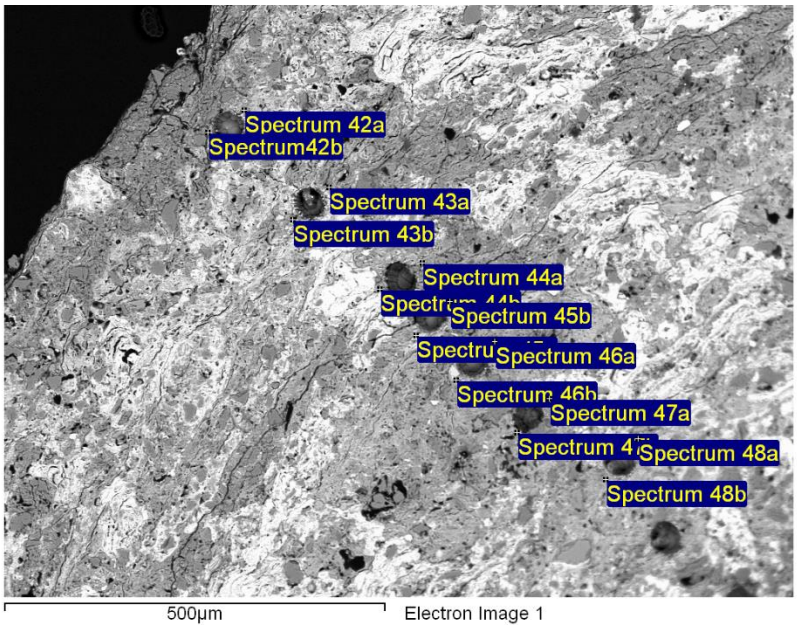

Processing option : All elements analysed (Normalised)

Spectrum	In stats.	O	Na	Mg	Al	Si	P	Cl	K	Ca	Ti	Mn	Fe	Total
Spectrum 42a	Yes	59.68			0.19	39.39						0.34	0.40	100.00
Spectrum42b	Yes	39.43		0.96	4.58	21.32			0.38	0.73	0.56	3.80	28.24	100.00
Spectrum 43a	Yes	53.08		1.36	7.36	17.11			1.74	0.54	0.28	2.23	16.31	100.00
Spectrum 43b	Yes	52.05		0.72	2.84	5.35	0.24	0.18	0.48	0.60	0.38	5.61	31.55	100.00
Spectrum 44a	Yes	60.99	0.32	0.71	3.87	22.85		0.13	0.78	0.28		0.67	9.40	100.00
Spectrum 44b	Yes	60.24		0.36	2.30	31.48			0.71			0.55	4.36	100.00
Spectrum 45a	Yes	57.76		0.76	7.78	11.79	0.15		2.06	0.62	0.28	8.45	10.34	100.00
Spectrum 45b	Yes	70.02			2.98	6.32		9.92					10.75	100.00
Spectrum 46a	Yes	45.07		0.64	4.74	22.09		1.75	1.49	0.49	1.01	1.18	21.54	100.00
Spectrum 46b	Yes	13.17		0.52	4.01	11.85			3.29	1.62	0.73	2.32	62.50	100.00
Spectrum 47a	Yes	60.69		0.20	1.04	33.60			0.42	0.20		2.04	1.80	100.00
Spectrum 47b	Yes	42.47		0.93	5.31	12.02	0.28	0.43	1.11	0.55	0.32	1.95	34.62	100.00
Spectrum 48a	Yes	41.87		0.61	4.56	10.92	0.26		1.39	0.64	0.45	6.84	32.46	100.00
Spectrum 48b	Yes	48.09		1.10	6.90	14.87	0.22		1.90	0.62	0.36	1.33	24.60	100.00
Max.		70.02	0.32	1.36	7.78	39.39	0.28	9.92	3.29	1.62	1.01	8.45	62.50	
Min.		13.17	0.32	0.20	0.19	5.35	0.15	0.13	0.38	0.20	0.28	0.34	0.40	

All results in weight%

Sample: PLA15-1H 10.10.2019 13:57:09

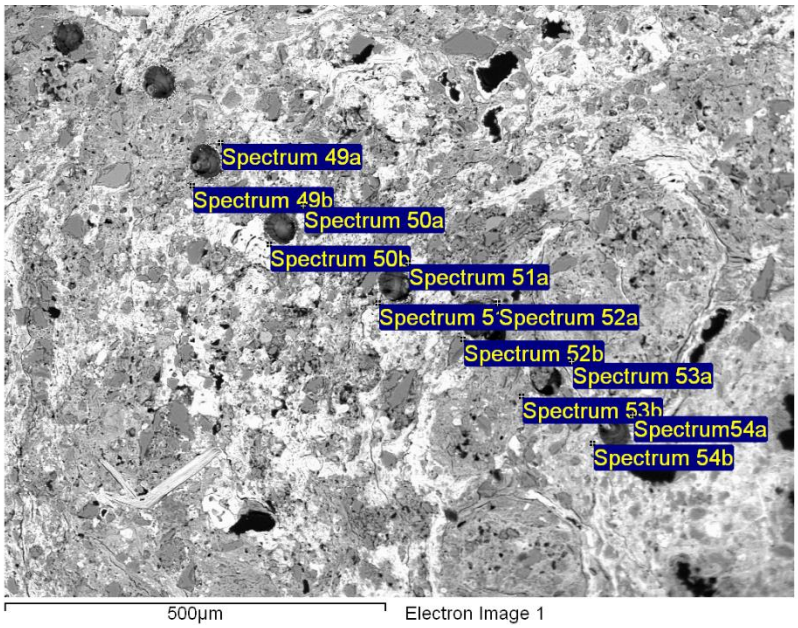

Processing option : All elements analysed (Normalised)

Spectrum	In stats.	O	F	Na	Mg	Al	Si	P	Cl	K	Ca	Ti	Mn	Fe	Ba	Total
Spectrum 49a	Yes	49.51		5.26	0.23	6.76	24.10		0.24	0.54	0.46		0.56	12.33		100.00
Spectrum 49b	Yes	49.30			0.97	5.42	11.47	0.26		1.15	0.54	0.25	2.91	27.73		100.00
Spectrum 50a	Yes	48.46			1.52	6.67	14.85	0.18		2.06	0.63	0.44	7.07	18.15		100.00
Spectrum 50b	Yes	46.21	0.00		0.76	2.61	7.23			0.79	0.80		24.35	13.95	3.31	100.00
Spectrum 51a	Yes	37.81			0.43	1.92	12.67	0.24		0.56	1.22		24.44	18.68	2.03	100.00
Spectrum 51b	Yes	63.16				0.60	35.25			0.20			0.39	0.40		100.00
Spectrum 52a	Yes	43.54			0.87	5.67	12.41	0.20		1.55	1.27	0.42	9.14	24.94		100.00
Spectrum 52b	Yes	43.31		0.58	1.03	6.13	19.55		0.50	1.95	0.74	0.43	8.32	17.45		100.00
Spectrum 53a	Yes	48.20			1.03	5.74	16.92	0.19		1.96	0.58	0.38	2.32	22.67		100.00
Spectrum 53b	Yes	48.38			1.17	7.23	17.40			2.63	0.64	0.45	2.89	19.21		100.00
Spectrum54a	Yes	51.79			1.27	6.58	14.34	0.17		2.32	0.63	0.41	6.48	16.02		100.00
Spectrum 54b	Yes	50.42			0.83	4.52	16.05			1.36	0.62		16.44	6.63	3.13	100.00
Max.		63.16	0.00	5.26	1.52	7.23	35.25	0.26	0.50	2.63	1.27	0.45	24.44	27.73	3.31	
Min.		37.81	0.00	0.58	0.23	0.60	7.23	0.17	0.24	0.20	0.46	0.25	0.39	0.40	2.03	

All results in weight%

Sample: PLA15-2H 10.10.2019 13:40:56

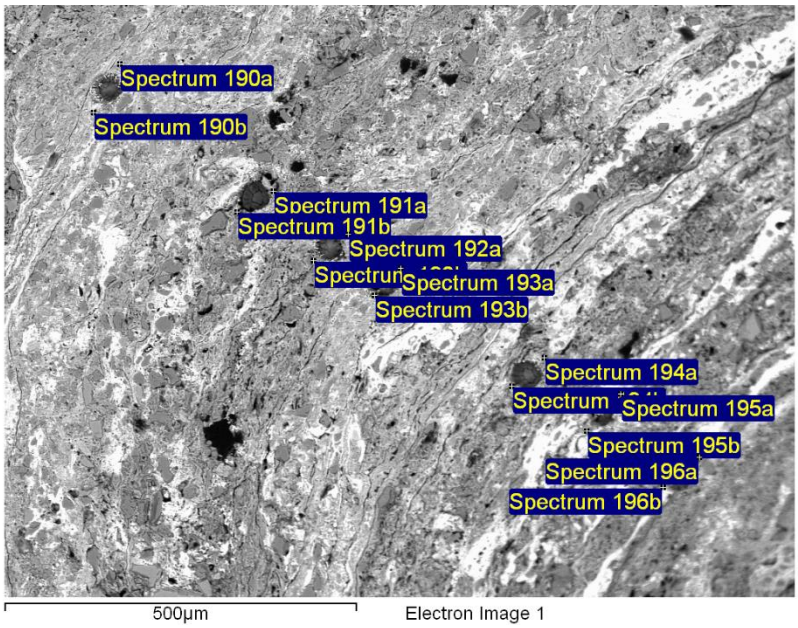

Processing option : All elements analysed (Normalised)

Spectrum	In stats.	O	Mg	Al	Si	P	Cl	K	Ca	Ti	Mn	Fe	Ba	Total
Spectrum 190a	Yes	57.89	0.93	6.98	18.32			2.27	0.24		0.52	12.84		100.00
Spectrum 190b	Yes	56.24	1.32	6.16	15.62			1.57	0.39		2.71	15.60	0.40	100.00
Spectrum 191a	Yes	55.40	1.28	6.78	16.55		1.18	1.55	1.01	0.61	8.09	7.57		100.00
Spectrum 191b	Yes	60.43	1.52	5.08	17.24		1.45	0.46	1.35		5.35	7.12		100.00
Spectrum 192a	Yes	59.87	0.28	1.00	33.52			0.29	0.35		2.37	2.33		100.00
Spectrum 192b	Yes	40.24	0.64	2.66	16.34	0.24		0.64	0.55	0.58	9.29	28.81		100.00
Spectrum 193a	Yes	49.99	1.08	6.64	13.86			2.15	0.54	0.36	1.22	24.16		100.00
Spectrum 193b	Yes	35.11	1.53	7.05	10.85			1.35	0.74	0.46	2.46	40.45		100.00
Spectrum 194a	Yes	58.92	1.40	6.97	15.62			2.23	0.75	0.41	5.28	8.41		100.00
Spectrum 194b	Yes	7.92		1.13	5.57			0.90	1.77	0.99	36.88	39.58	5.25	100.00
Spectrum 195a	Yes	18.78		1.35	4.58			2.71			29.37	37.97	5.24	100.00
Spectrum 195b	Yes	54.32	1.33	4.56	16.54			1.11	0.49		11.32	8.13	2.19	100.00
Spectrum 196a	Yes	54.19	1.06	4.22	19.63			1.59	0.47	0.53	9.06	7.71	1.54	100.00
Spectrum 196b	Yes	52.70	0.76	3.80	14.29			0.84	0.58		18.98	3.91	4.14	100.00
Max.		60.43	1.53	7.05	33.52	0.24	1.45	2.71	1.77	0.99	36.88	40.45	5.25	
Min.		7.92	0.28	1.00	4.58	0.24	1.18	0.29	0.24	0.36	0.52	2.33	0.40	

All results in weight%

Sample: PLA15-2H 10.10.2019 13:43:48

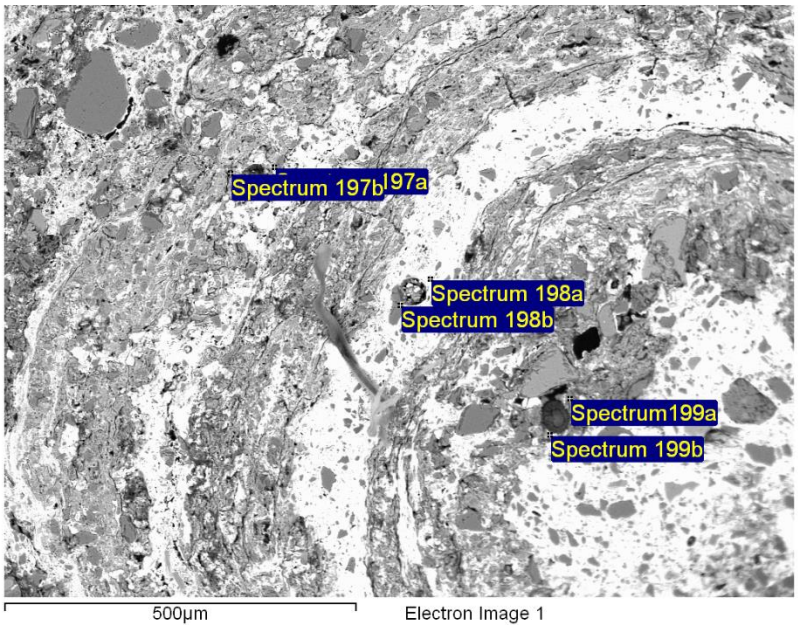

Processing option : All elements analysed (Normalised)

Spectrum	In stats.	O	Na	Mg	Al	Si	K	Ca	Ti	Mn	Fe	Ba	Total
Spectrum 197a	Yes	47.99	0.86	1.21	6.23	16.29	1.87	0.59	0.40	5.68	18.87		100.00
Spectrum 197b	Yes	49.24		1.19	9.53	16.60	3.24	1.95	0.26	1.04	16.94		100.00
Spectrum 198a	Yes	42.92	0.68	0.45	1.44	3.20	0.21	0.49		40.78	1.04	8.79	100.00
Spectrum 198b	Yes	54.30		0.21	1.22	25.72	0.75	0.21		13.77	0.90	2.93	100.00
Spectrum199a	Yes	57.95	7.23		8.24	26.59							100.00
Spectrum 199b	Yes	10.51	0.42	0.33	1.28	4.19	0.49	0.77		60.74	11.37	9.89	100.00
Max.		57.95	7.23	1.21	9.53	26.59	3.24	1.95	0.40	60.74	18.87	9.89	
Min.		10.51	0.42	0.21	1.22	3.20	0.21	0.21	0.26	1.04	0.90	2.93	

All results in weight%

Sample: PLA15-5D 10.10.2019 12:14:07

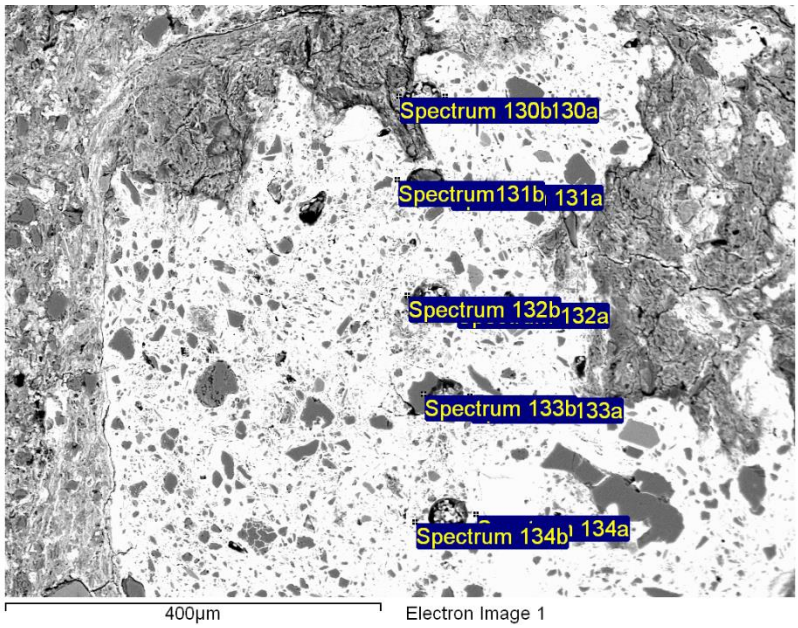

Processing option : All elements analysed (Normalised)

Spectrum	In stats.	O	Na	Mg	Al	Si	K	Ca	Ti	Mn	Fe	Ba	Total
Spectrum 134a	Yes	38.09		0.80	1.79	3.11	0.66	0.45		43.28	2.52	9.30	100.00
Spectrum 134b	Yes	38.47		0.77	5.63	9.66	2.08	0.34		31.97	3.75	7.33	100.00
Spectrum 133a	Yes	53.21		0.20	1.13	20.25	0.42	0.18		19.02	1.27	4.33	100.00
Spectrum 133b	Yes	60.71				38.58				0.71			100.00
Spectrum 132a	Yes	45.90	0.46	0.70	3.95	15.93	1.21	0.39		22.28	4.48	4.71	100.00
Spectrum 132b	Yes	60.25		0.28	1.25	29.16	0.40			5.69	1.64	1.34	100.00
Spectrum 131a	Yes	46.65		0.86	5.26	10.56	2.00	0.36		22.90	6.21	5.21	100.00
Spectrum131b	Yes	43.64		0.46	2.56	4.88	0.90	0.43	1.09	34.01	4.85	7.19	100.00
Spectrum 130a	Yes	50.21		1.05	3.27	5.99	1.04	0.50		27.21	4.74	5.99	100.00
Spectrum 130b	Yes	55.87		1.16	4.57	23.94	1.27	0.44		1.61	11.15		100.00
Max.		60.71	0.46	1.16	5.63	38.58	2.08	0.50	1.09	43.28	11.15	9.30	
Min.		38.09	0.46	0.20	1.13	3.11	0.40	0.18	1.09	0.71	1.27	1.34	

All results in weight%

Sample: PLA15-5D 10.10.2019 12:17:47

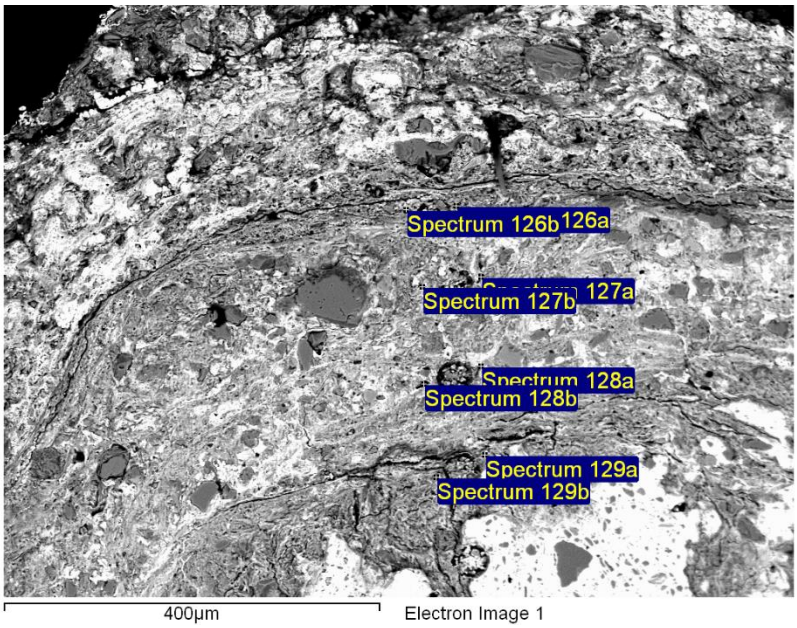

Processing option : All elements analysed (Normalised)

Spectrum	In stats.	O	Mg	Al	Si	K	Ca	Ti	Mn	Fe	Ba	Total
Spectrum 129a	Yes	50.59	1.65	6.16	19.35	1.95	0.46	0.30	2.84	16.70		100.00
Spectrum 129b	Yes	16.92	0.53	2.34	5.73	2.70	0.91	1.60	23.70	45.57		100.00
Spectrum 128a	Yes	39.81	0.98	6.12	16.45	3.68	0.39	0.38	0.96	31.22		100.00
Spectrum 128b	Yes	14.44	0.48	1.95	6.45	1.40	1.09	0.83	9.74	63.62		100.00
Spectrum 127a	Yes	59.81	1.46	5.16	11.14	1.38	0.31	0.57	2.41	17.76		100.00
Spectrum 127b	Yes	53.89	0.40	2.86	27.33	1.53	0.25		7.24	5.10	1.41	100.00
Spectrum 126a	Yes	57.07	1.74	6.63	20.63	2.31	0.31	0.31	1.02	9.98		100.00
Spectrum 126b	Yes	33.90	1.13	4.46	15.82	2.36	0.72	0.98	10.37	30.26		100.00
Max.		59.81	1.74	6.63	27.33	3.68	1.09	1.60	23.70	63.62	1.41	
Min.		14.44	0.40	1.95	5.73	1.38	0.25	0.30	0.96	5.10	1.41	

All results in weight%

Sample: PLA15-5D 10.10.2019 12:20:47

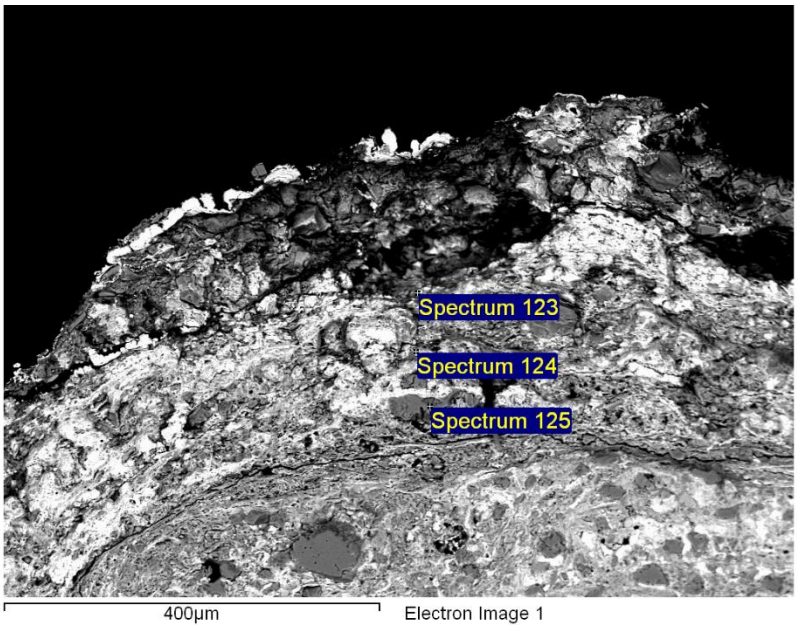

Processing option : All elements analysed (Normalised)

Spectrum	In stats.	O	Mg	Al	Si	P	K	Ca	Ti	Mn	Fe	Ba	Total
Spectrum 125	Yes	66.35			33.35					0.30			100.00
Spectrum 124	Yes	54.57	1.72	5.78	13.30		2.07	0.51	0.29	13.73	5.93	2.09	100.00
Spectrum 123	Yes	39.94	0.92	1.82	5.60	0.19	0.49	0.61		36.95	5.55	7.94	100.00
Max.		66.35	1.72	5.78	33.35	0.19	2.07	0.61	0.29	36.95	5.93	7.94	
Min.		39.94	0.92	1.82	5.60	0.19	0.49	0.51	0.29	0.30	5.55	2.09	

All results in weight%

Sample: PLA15-8D 10.10.2019 12:27:57

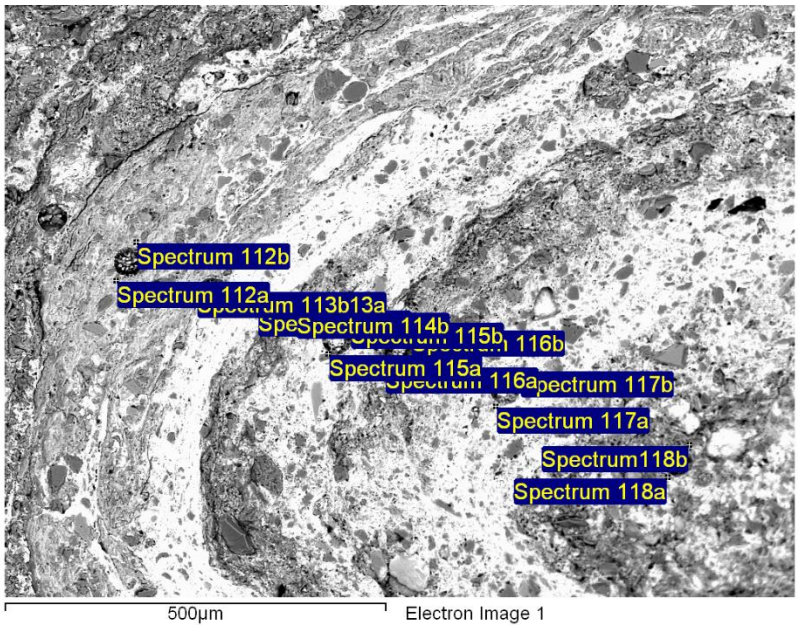

Processing option : All elements analysed (Normalised)

Spectrum	In stats.	O	F	Na	Mg	Al	Si	K	Ca	Ti	V	Mn	Fe	Ba	Total
Spectrum 118a	Yes	43.02		0.31	0.98	4.31	10.15	1.31	0.53			26.87	6.62	5.90	100.00
Spectrum118b	Yes	51.01			0.75	4.39	29.28	1.59	0.26			7.15	4.04	1.53	100.00
Spectrum 117a	Yes	53.96			1.61	7.94	10.89	2.52		0.41		15.93	3.41	3.33	100.00
Spectrum 117b	Yes	60.47				0.36	36.55	0.18				2.11	0.33		100.00
Spectrum 116a	Yes	45.70			0.48	4.01	9.10	1.18	0.36			29.45	3.60	6.11	100.00
Spectrum 116b	Yes	63.85		0.26	0.67	9.36	13.41	0.69	0.25			7.35	2.54	1.63	100.00
Spectrum 115a	Yes	67.85				0.41	30.18		0.08	0.14		1.09	0.25		100.00
Spectrum 115b	Yes	54.47				0.53	39.18	0.24				3.96	0.77	0.85	100.00
Spectrum 114a	Yes	43.96			0.33	1.30	16.91	0.57	0.40			27.97	2.56	6.01	100.00
Spectrum 114b	Yes	39.68	0.00		1.03	2.68	8.51	0.73	0.84			29.05	12.29	5.18	100.00
Spectrum 113a	Yes	46.34			0.44	1.26	1.77	0.33	0.55			38.28	3.11	7.91	100.00
Spectrum 113b	Yes	11.14										31.04	57.82		100.00
Spectrum 112a	Yes	57.12			1.26	5.46	12.21	1.55	0.43	0.28		1.62	20.06		100.00
Spectrum 112b	Yes	47.26			0.86	3.26	8.48	1.11	0.35	0.32	0.27	0.89	37.19		100.00
Max.		67.85	0.00	0.31	1.61	9.36	39.18	2.52	0.84	0.41	0.27	38.28	57.82	7.91	
Min.		11.14	0.00	0.26	0.33	0.36	1.77	0.18	0.08	0.14	0.27	0.89	0.25	0.85	

All results in weight%

Sample: PLA15-8D 10.10.2019 12:36:12

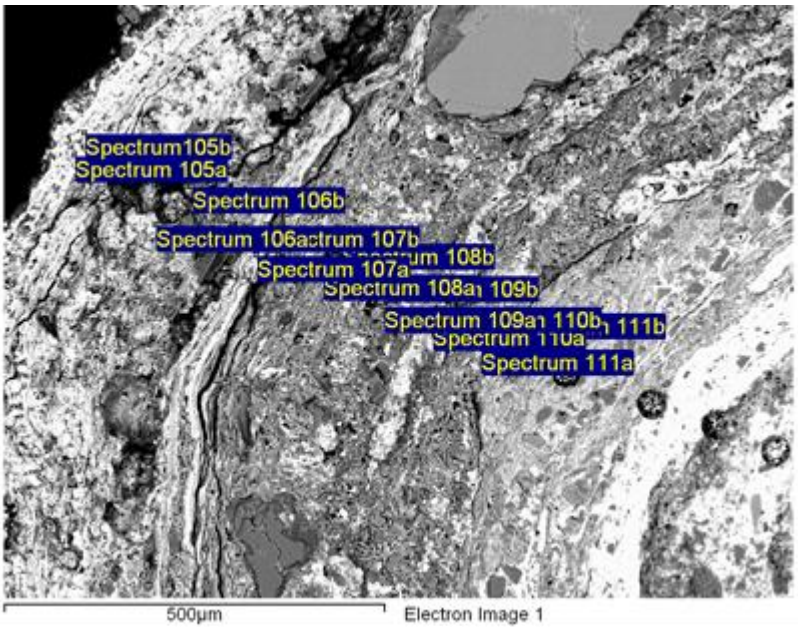

Processing option : All elements analysed (Normalised)

Spectrum	In stats.	O	F	Na	Mg	Al	Si	K	Ca	Ti	Mn	Fe	Cu	Ba	Total
Spectrum 111a	Yes	56.35			1.08	4.89	25.43	4.67			2.43	5.16			100.00
Spectrum 111b	Yes	27.03			0.90	6.35	22.52	4.49	0.82		16.70	18.21		2.97	100.00
Spectrum 110a	Yes	59.01			0.19	0.73	35.85	0.23		0.22	2.56	1.21			100.00
Spectrum 110b	Yes	61.16			0.67	1.62	32.15	0.13	0.24		2.02	1.38		0.63	100.00
Spectrum 109a	Yes	66.16		0.43	0.37	6.24	18.65	4.85			0.99	1.69		0.63	100.00
Spectrum 109b	Yes	58.99			0.75	6.70	19.97	5.23			2.56	5.33		0.47	100.00
Spectrum 108a	Yes	51.29			1.37	5.46	15.23	1.78	0.66	0.83	10.05	13.34			100.00
Spectrum 108b	Yes	55.54			1.16	3.89	24.75	1.02	0.36	0.31	4.70	8.28			100.00
Spectrum 107a	Yes	57.15	0.00		1.44	5.41	10.58	1.26	0.54		14.82	6.24		2.56	100.00
Spectrum 107b	Yes	11.33				1.11	2.50	1.73	1.23	1.68	36.00	41.00	3.42		100.00
Spectrum 106a	Yes	8.44				2.26	17.53	3.00	0.92		45.18	13.64		9.03	100.00
Spectrum 106b	Yes	43.43			0.89	4.54	11.03	7.60		1.65	15.51	15.35			100.00
Spectrum 105a	Yes	33.21			0.86	3.24	6.86	1.12	0.60		40.23	5.10		8.78	100.00
Spectrum105b	Yes	39.41			1.00	4.12	8.73	1.57	0.65	0.58	32.44	4.88		6.61	100.00
Max.		66.16	0.00	0.43	1.44	6.70	35.85	7.60	1.23	1.68	45.18	41.00	3.42	9.03	
Min.		8.44	0.00	0.43	0.19	0.73	2.50	0.13	0.24	0.22	0.99	1.21	3.42	0.47	

All results in weight%

Sample: PLA15-10D 10.10.2019 11:57:57

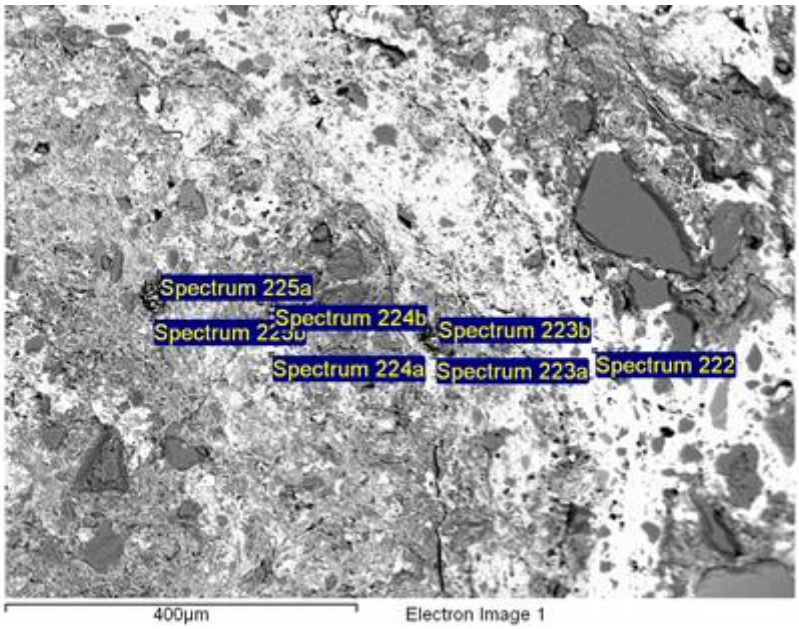

Processing option : All elements analysed (Normalised)

Spectrum	In stats.	O	Na	Mg	Al	Si	P	K	Ca	Ti	Mn	Fe	Ba	Total
Spectrum 225a	Yes	29.04		1.03	4.94	14.60	0.30	2.78	0.69	0.65	6.74	39.24		100.00
Spectrum 225b	Yes	53.19		1.38	6.00	15.37		1.36	0.43	0.48	8.56	13.25		100.00
Spectrum 224a	Yes	46.70		0.99	4.53	10.10	0.22	1.34	0.72	0.68	11.63	23.10		100.00
Spectrum 224b	Yes	34.68	2.14	0.46	7.28	20.05		1.81	1.64		9.01	22.92		100.00
Spectrum 223a	Yes	51.54		1.12	4.33	9.47		1.18	0.34	0.68	20.30	6.52	4.50	100.00
Spectrum 223b	Yes	50.18		1.25	6.35	16.86		1.95	0.49	0.38	11.41	8.93	2.20	100.00
Spectrum 222	Yes	32.42		0.38	1.31	2.42		0.51	0.48		48.65	3.39	10.43	100.00
Max.		53.19	2.14	1.38	7.28	20.05	0.30	2.78	1.64	0.68	48.65	39.24	10.43	
Min.		29.04	2.14	0.38	1.31	2.42	0.22	0.51	0.34	0.38	6.74	3.39	2.20	

All results in weight%

Sample: PLA15-10D 10.10.2019 12:02:47

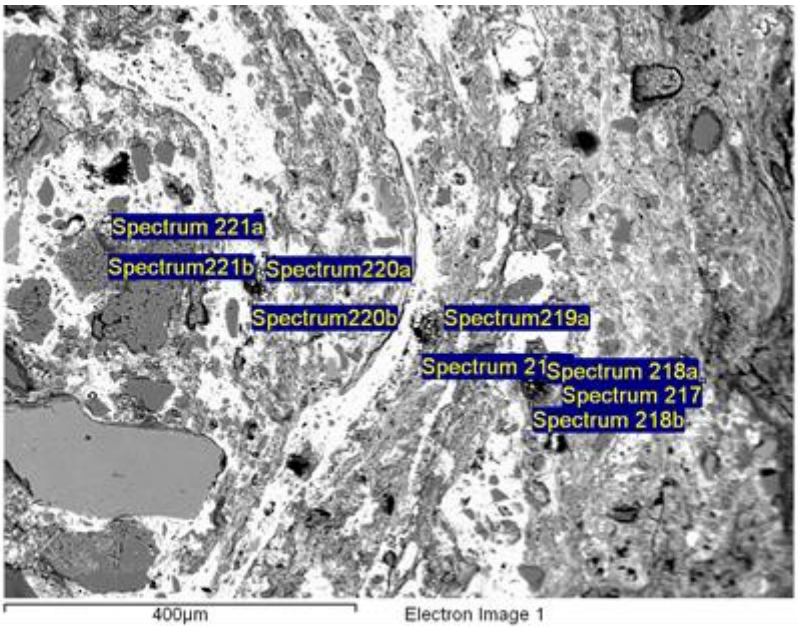

Processing option : All elements analysed (Normalised)

Spectrum	In stats.	O	Na	Mg	Al	Si	K	Ca	Ti	V	Mn	Fe	Ba	Total
Spectrum 221a	Yes	59.82			0.95	36.51					1.37	0.34	1.00	100.00
Spectrum221b	Yes	62.05	5.45		10.26	19.68	0.76	0.32			0.71	0.78		100.00
Spectrum220a	Yes	61.00		0.27	1.25	33.05	0.49		0.33		2.50	1.12		100.00
Spectrum220b	Yes	58.15	4.63	0.46	7.31	19.00	0.41	0.34			5.48	2.67	1.55	100.00
Spectrum219a	Yes	49.24		0.96	4.53	9.63	1.28	0.75		0.30	21.11	8.36	3.85	100.00
Spectrum 219b	Yes	38.20		1.35	5.23	15.95	2.48	0.79	1.02		9.98	24.99		100.00
Spectrum 218a	Yes	57.87		1.24	5.72	11.92	1.37	0.52			10.30	9.71	1.36	100.00
Spectrum 218b	Yes	53.63		1.77	5.34	18.50	0.69	0.96			4.74	13.73	0.64	100.00
Spectrum 217	Yes	51.76		1.73	4.79	16.70	1.48	0.47	0.91		4.18	17.98		100.00
Max.		62.05	5.45	1.77	10.26	36.51	2.48	0.96	1.02	0.30	21.11	24.99	3.85	
Min.		38.20	4.63	0.27	0.95	9.63	0.41	0.32	0.33	0.30	0.71	0.34	0.64	

All results in weight%

Sample: PLA15-10D 10.10.2019 12:04:43

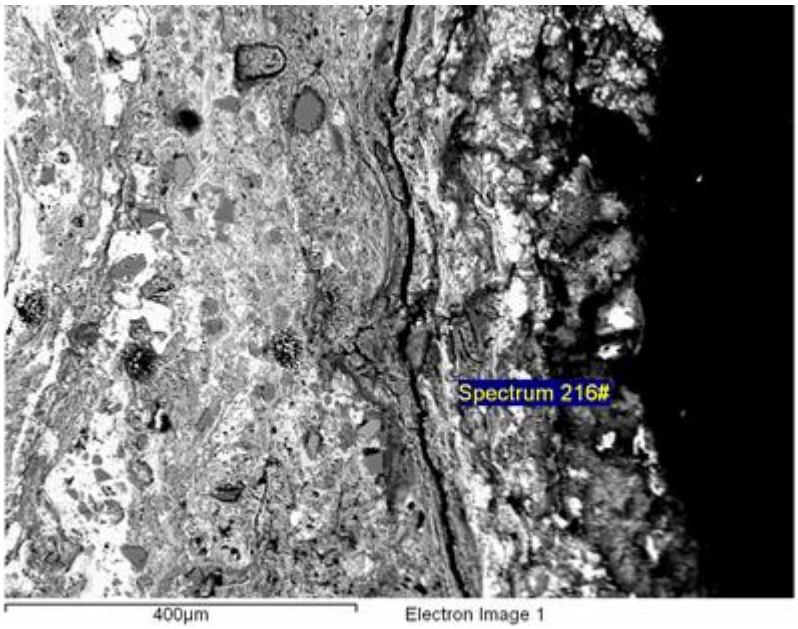

Processing option : All elements analysed (Normalised)

Spectrum	In stats.	O	Mg	Al	Si	K	Ca	Mn	Fe	Ba	Total
Spectrum 216#	Yes	19.40	0.76	2.40	7.21	2.75	1.19	38.86	22.12	5.30	100.00
Max.		19.40	0.76	2.40	7.21	2.75	1.19	38.86	22.12	5.30	
Min.		19.40	0.76	2.40	7.21	2.75	1.19	38.86	22.12	5.30	

All results in weight%

Sample: PLA15-11D 10.10.2019 11:47:02

Processing option : All elements analysed (Normalised)

Spectrum	In stats.	O	Na	Mg	Al	Si	P	S	K	Ca	Ti	V	Mn	Fe	Ba	Total
Spectrum 100	Yes	49.12		0.65	4.06	13.64			1.00	0.33			22.38	3.50	5.32	100.00
Spectrum 99a	Yes	53.06		0.45	2.38	15.65			0.78	0.28			19.20	4.20	4.01	100.00
Spectrum 99b	Yes	25.12	0.30	0.36	2.40	7.62			1.53	0.68			44.43	8.17	9.39	100.00
Spectrum 98a	Yes	47.16		1.52	9.18	20.46			4.05	0.36	0.39		0.70	16.18		100.00
Spectrum 98b	Yes	49.66		1.50	7.36	14.31			2.20	0.54	0.47		6.88	17.07		100.00
Spectrum 97a	Yes	46.86		4.22	7.39	15.77			1.93	0.47	0.46		7.85	13.28	1.77	100.00
Spectrum 97b	Yes	55.88		1.18	5.70	9.86			1.63	0.37	0.32		15.96	5.64	3.47	100.00
Spectrum 96a	Yes	5.28			0.98	2.06			3.73	1.04	1.80		23.30	61.82		100.00
Spectrum 96b	Yes	61.79		3.96	6.90	12.05			2.19	0.24	0.67		3.24	8.96		100.00
Spectrum 95a	Yes	38.96	0.31	0.53	2.91	5.89			1.02	0.49			37.27	4.22	8.40	100.00
Spectrum 95b	Yes	12.24			1.60	4.89			1.52				54.11	16.64	9.01	100.00
Spectrum 94a	Yes	28.12		0.62	1.72	20.40			0.50	0.65			38.13	4.12	5.73	100.00
Spectrum 94b	Yes	41.35		0.43	1.96	10.82			0.61	0.50			32.60	4.32	7.41	100.00
Spectrum 93a	Yes	20.81		0.52	3.17	20.05			3.23	0.70	1.20		9.07	41.25		100.00
Spectrum 93b	Yes	61.02		1.40	5.82	17.42		0.25	1.61	0.31	0.88		3.12	8.17		100.00
Spectrum 92a	Yes	32.61		1.21	5.69	14.10	0.26		1.92	3.36			4.60	36.24		100.00
Spectrum 92b	Yes	38.77		2.36	6.56	17.11			3.01	0.75			1.46	29.98		100.00
Spectrum 91a	Yes	42.69		0.83	3.02	9.75	0.18		1.00	0.31		0.40	0.74	41.07		100.00
Spectrum 91b	Yes	41.35		0.89	5.78	15.94			4.10	0.65	0.60		3.74	26.95		100.00
Max.		61.79	0.31	4.22	9.18	20.46	0.26	0.25	4.10	3.36	1.80	0.40	54.11	61.82	9.39	
Min.		5.28	0.30	0.36	0.98	2.06	0.18	0.25	0.50	0.24	0.32	0.40	0.70	3.50	1.77	

All results in weight%

Sample: PLA15-11D 10.10.2019 11:50:12

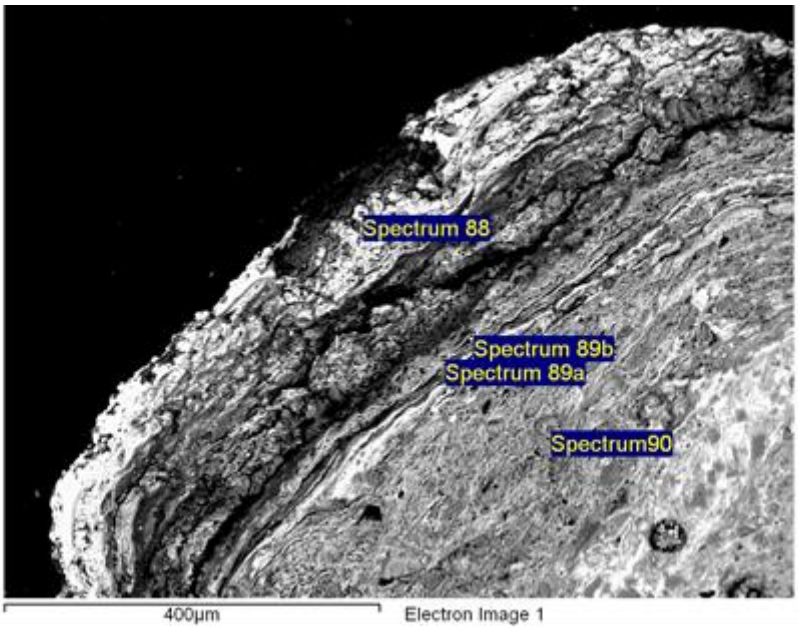

Processing option : All elements analysed (Normalised)

Spectrum	In stats.	O	Na	Mg	Al	Si	K	Ca	Ti	Mn	Fe	Ba	Ce	Total
Spectrum90	Yes	48.94	0.30	1.51	6.54	18.14	2.19	0.51	0.58	1.54	19.75			100.00
Spectrum 89a	Yes	58.15		2.99	6.42	14.02	1.70	0.50	0.79	6.36	8.68		0.39	100.00
Spectrum 89b	Yes	53.35		1.52	6.33	14.42	2.40	0.56	0.35	10.86	8.59	1.61		100.00
Spectrum 88	Yes									80.25	12.24	7.51		100.00
Max.		58.15	0.30	2.99	6.54	18.14	2.40	0.56	0.79	80.25	19.75	7.51	0.39	
Min.		48.94	0.30	1.51	6.33	14.02	1.70	0.50	0.35	1.54	8.59	1.61	0.39	

All results in weight%

Sample: Zr7-7D 10.10.2019 11:06:48

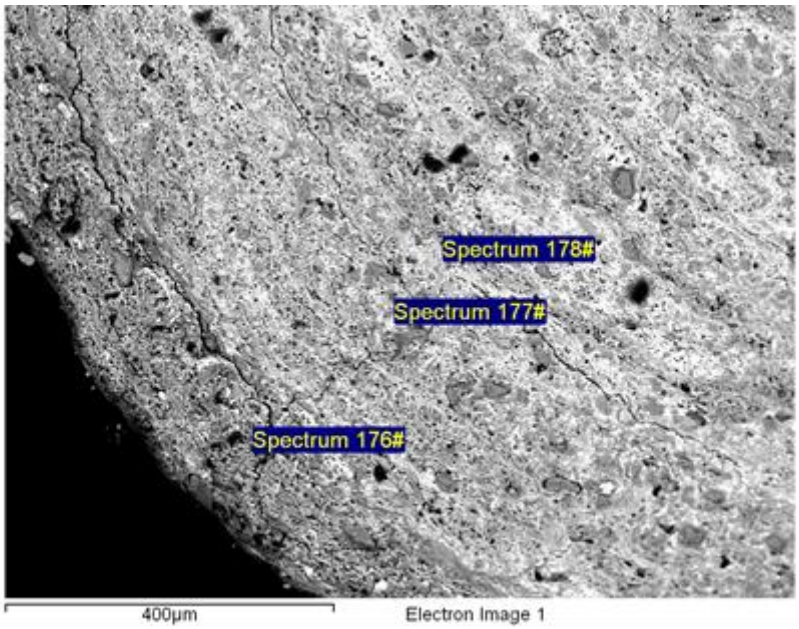

Processing option : All elements analysed (Normalised)

Spectrum	In stats.	O	Na	Mg	Al	Si	K	Ca	Ti	Mn	Fe	Ba	Total
Spectrum 176#	Yes	61.16	0.40	0.53	4.06	26.14	1.89		0.22	2.65	2.94		100.00
Spectrum 177#	Yes	49.13		1.70	6.36	23.03	2.16	0.33		6.61	9.54	1.15	100.00
Spectrum 178#	Yes	57.44	0.40	1.70	7.63	17.81	2.14	0.33	0.48	4.47	7.60		100.00
Max.		61.16	0.40	1.70	7.63	26.14	2.16	0.33	0.48	6.61	9.54	1.15	
Min.		49.13	0.40	0.53	4.06	17.81	1.89	0.33	0.22	2.65	2.94	1.15	

All results in weight%

Sample: Zr7-7D 10.10.2019 11:11:27

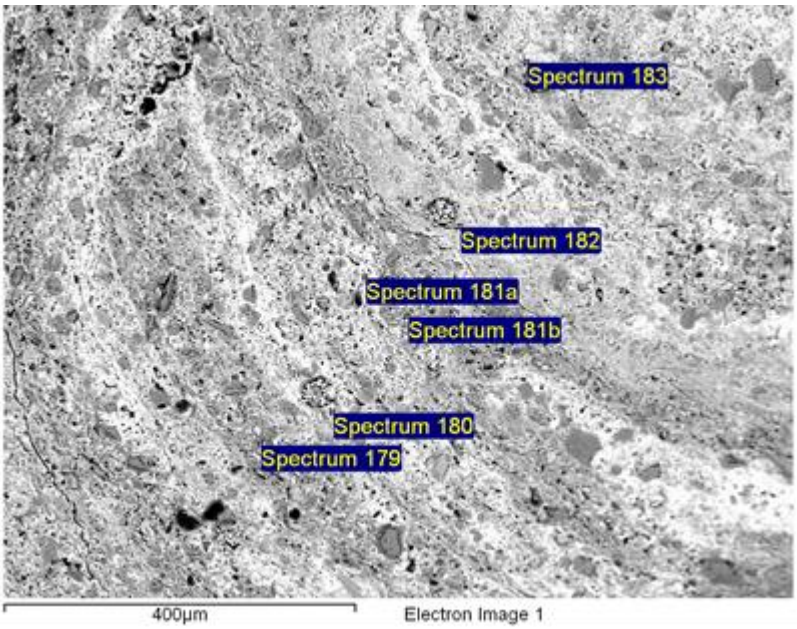

Processing option : All elements analysed (Normalised)

Spectrum	In stats.	O	Na	Mg	Al	Si	P	K	Ca	Ti	Mn	Fe	Ba	Total
Spectrum 180	Yes	54.94	0.45	0.89	7.16	14.44		1.83	0.41	0.43	5.67	13.78		100.00
Spectrum 181	Yes	53.27		1.20	6.01	14.38		1.98	0.35		14.12	5.69	3.01	100.00
Spectrum 182a	Yes	27.63		1.24	4.90	9.76		2.70	0.82	0.70	32.14	15.25	4.87	100.00
Spectrum 182b	Yes	61.97		0.66	2.56	29.93		0.75			1.22	2.63	0.28	100.00
Spectrum 183	Yes	53.82		1.36	7.74	17.18		2.58	0.41	0.38	7.30	7.82	1.40	100.00
Spectrum 184	Yes	27.45		0.65	5.21	18.67	0.23	3.55	0.84		23.78	14.75	4.87	100.00
Max.		61.97	0.45	1.36	7.74	29.93	0.23	3.55	0.84	0.70	32.14	15.25	4.87	
Min.		27.45	0.45	0.65	2.56	9.76	0.23	0.75	0.35	0.38	1.22	2.63	0.28	

All results in weight%

Sample: Zr7-7D 10.10.2019 11:18:08

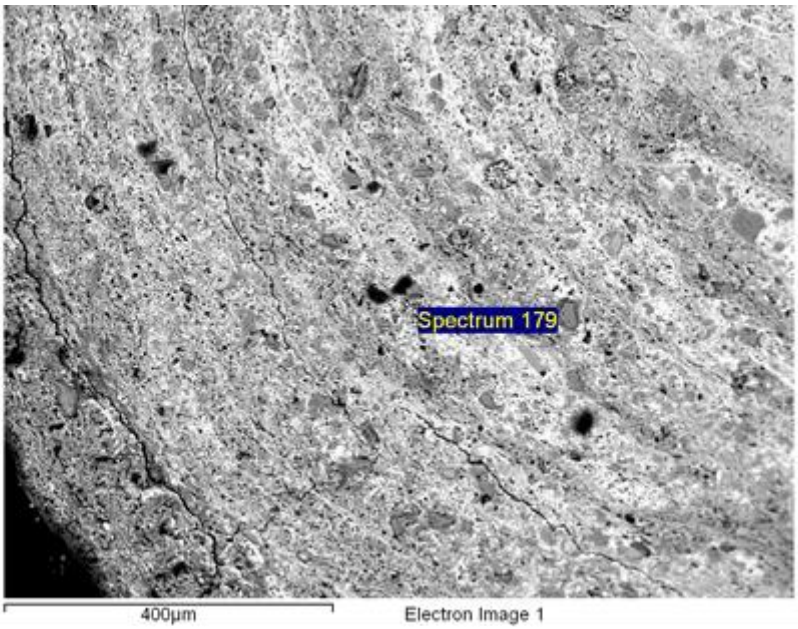

Processing option : All elements analysed (Normalised)

Spectrum	In stats.	O	Na	Mg	Al	Si	K	Ti	Mn	Fe	Total
Spectrum 179	Yes	45.89	3.51	0.28	9.33	28.53	1.28	0.61	6.16	4.40	100.00
Max.		45.89	3.51	0.28	9.33	28.53	1.28	0.61	6.16	4.40	
Min.		45.89	3.51	0.28	9.33	28.53	1.28	0.61	6.16	4.40	

All results in weight%

Sample: Zr7-7D 10.10.2019 11:20:08

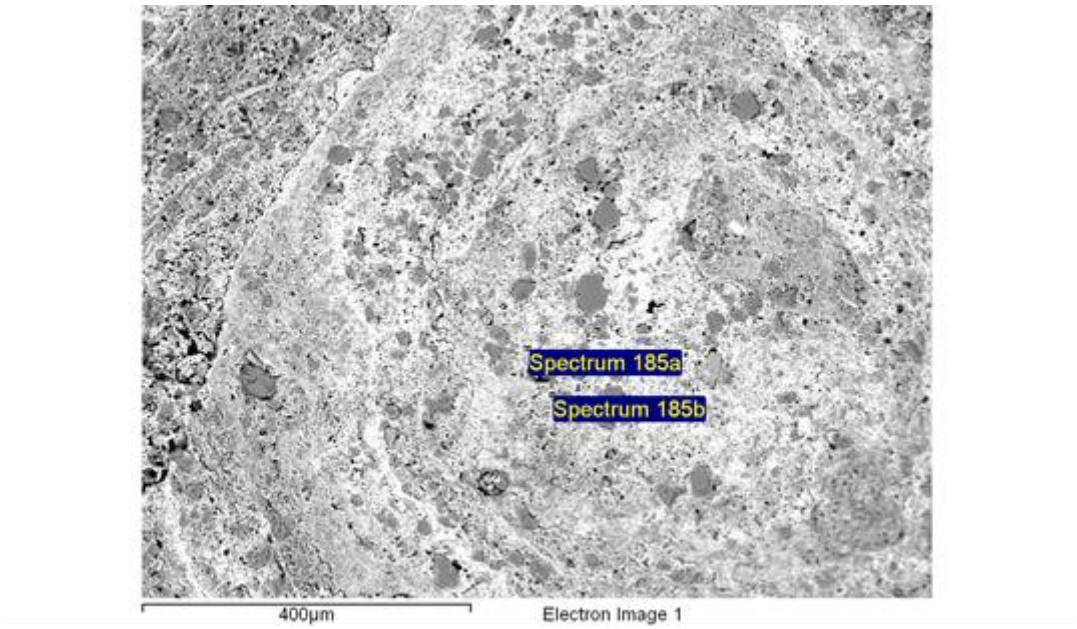

Processing option : All elements analysed (Normalised)

Spectrum	In stats.	O	Na	Mg	Al	Si	K	Ca	Ti	Mn	Fe	Ba	Total
Spectrum 185a	Yes	45.95		0.81	7.18	13.16	2.74	0.42	0.45	19.08	6.28	3.92	100.00
Spectrum 185b	Yes	53.65	0.88	0.94	7.37	16.95	1.88	0.31	0.49	10.57	4.87	2.11	100.00
Max.		53.65	0.88	0.94	7.37	16.95	2.74	0.42	0.49	19.08	6.28	3.92	
Min.		45.95	0.88	0.81	7.18	13.16	1.88	0.31	0.45	10.57	4.87	2.11	

All results in weight%

Sample: Zr5-1H 10.10.2019 14:03:52

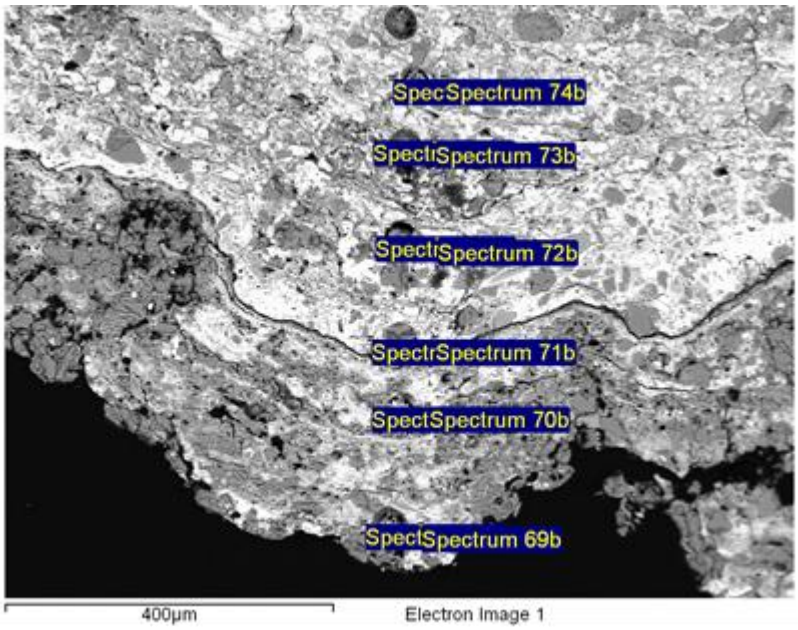

Processing option : All elements analysed (Normalised)

Spectrum	In stats.	O	F	Na	Mg	Al	Si	Cl	K	Ca	Ti	Mn	Fe	Ba	Total
Spectrum 69a	Yes	45.13			1.77	6.06	13.31		1.47	0.53	0.37	19.94	7.22	4.21	100.00
Spectrum 69b	Yes	45.16			1.57	5.23	11.08		1.63	0.50		23.99	6.24	4.60	100.00
Spectrum 70a	Yes	65.95			0.44	2.87	26.10		1.04		0.19	1.69	1.73		100.00
Spectrum 70b	Yes	41.95			0.67	1.75	4.13		0.65	0.71		37.17	5.73	7.24	100.00
Spectrum 71a	Yes	41.82	0.00		0.33	0.58	1.28		0.15	0.61		38.96	7.75	8.52	100.00
Spectrum 71b	Yes	43.94			0.57	2.88	8.59		1.10	0.53		28.69	7.70	6.00	100.00
Spectrum 72a	Yes	26.12			0.58	2.27	5.03		0.66	0.82		35.27	22.60	6.66	100.00
Spectrum 72b	Yes	39.76	0.00		0.66	1.81	4.09	0.17	0.63	0.71		30.26	16.65	5.25	100.00
Spectrum 73a	Yes	11.53			0.47	1.44	8.92		1.40	1.07		42.11	25.94	7.12	100.00
Spectrum 73b	Yes	58.42			0.80	6.80	15.15		1.77	0.37		7.65	7.59	1.43	100.00
Spectrum 74a	Yes	13.65			0.54	2.04	5.95		3.19	1.12		6.36	67.13		100.00
Spectrum 74b	Yes	56.83		6.87		8.47	26.97			0.20		0.29	0.38		100.00
Max.		65.95	0.00	6.87	1.77	8.47	26.97	0.17	3.19	1.12	0.37	42.11	67.13	8.52	
Min.		11.53	0.00	6.87	0.33	0.58	1.28	0.17	0.15	0.20	0.19	0.29	0.38	1.43	

All results in weight%

Sample: Zr5-1H 10.10.2019 14:07:37

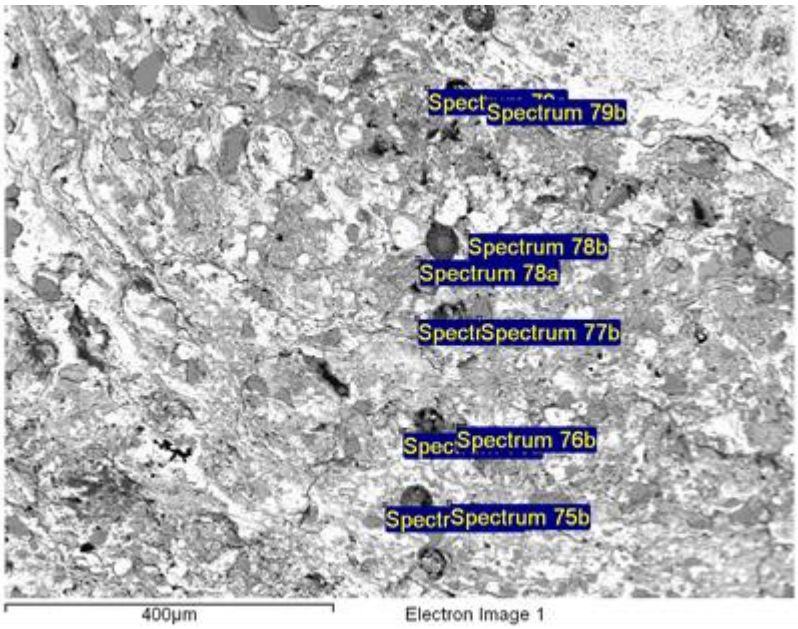

Processing option : All elements analysed (Normalised)

Spectrum	In stats.	O	Na	Mg	Al	Si	K	Ca	Ti	Mn	Fe	Ba	Total
Spectrum 75a	Yes	40.07		1.02	5.92	22.29	1.76	0.62		10.32	16.36	1.65	100.00
Spectrum 75b	Yes	49.72	0.63	1.07	7.03	18.43	2.14	0.50		2.08	18.41		100.00
Spectrum 76a	Yes	54.87		1.23	5.51	13.23	1.66	0.63		9.77	11.31	1.78	100.00
Spectrum 76b	Yes	13.76		0.95	2.32	11.79	2.69	1.23	1.43	31.87	28.10	5.87	100.00
Spectrum 77a	Yes	43.47		1.05	5.83	12.76	2.42	0.82		16.23	14.28	3.15	100.00
Spectrum 77b	Yes	65.55	0.17		2.75	30.22	0.72			0.23	0.36		100.00
Spectrum 78a	Yes	34.10		1.08	4.42	12.87	3.39	1.02	1.32	16.42	25.38		100.00
Spectrum 78b	Yes	52.66		1.00	4.01	8.37	1.10	0.63		20.90	7.46	3.87	100.00
Spectrum 79a	Yes	39.33		1.21	5.42	23.05	2.07	0.72	0.52	11.45	14.27	1.95	100.00
Spectrum 79b	Yes	3.70			1.52	4.69	3.49	0.88		52.26	24.14	9.32	100.00
Max.		65.55	0.63	1.23	7.03	30.22	3.49	1.23	1.43	52.26	28.10	9.32	
Min.		3.70	0.17	0.95	1.52	4.69	0.72	0.50	0.52	0.23	0.36	1.65	

All results in weight%

Sample: Zr5-1H 10.10.2019 14:12:01

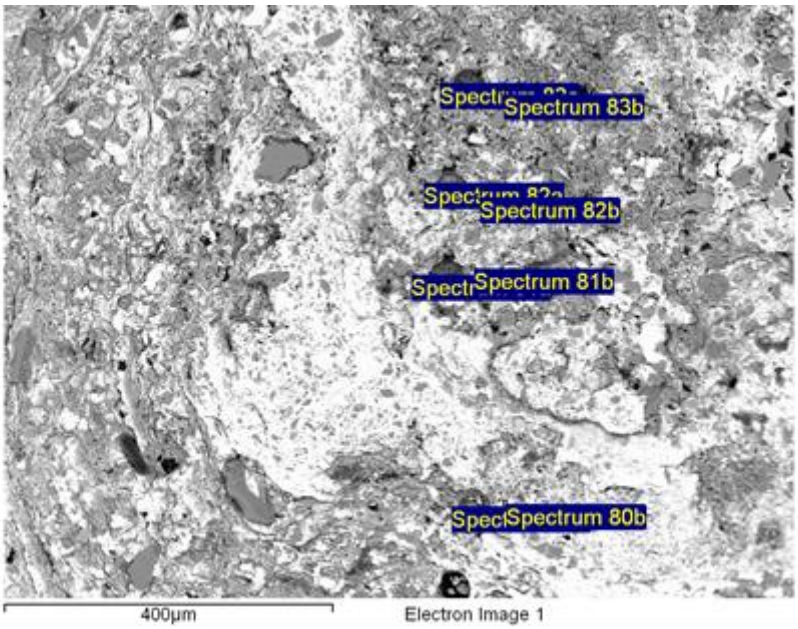

Processing option : All elements analysed (Normalised)

Spectrum	In stats.	O	F	Na	Mg	Al	Si	Cl	K	Ca	Ti	Mn	Fe	Ba	Ce	Total
Spectrum 80a	Yes	56.67		0.41	1.33	7.81	16.38		2.27	0.44	0.53	5.56	8.61			100.00
Spectrum 80b	Yes	55.80	0.00		1.11	3.24	11.53		1.21	0.36	3.82	16.53	5.46		0.95	100.00
Spectrum 81a	Yes	10.26			0.91	7.39	30.17		3.21	1.75		14.36	31.95			100.00
Spectrum 81b	Yes	55.53		0.24	1.06	6.42	12.93		1.65	0.50		11.79	7.36	2.51		100.00
Spectrum 82a	Yes	55.54		5.50	0.32	8.52	24.38		0.84	0.35		1.56	2.99			100.00
Spectrum 82b	Yes	59.23				0.15	40.63									100.00
Spectrum 83a	Yes	35.24			1.53	11.12	34.14	1.23	3.16	1.50		2.68	9.40			100.00
Spectrum 83b	Yes	47.06		0.48	0.57	8.71	16.67		2.04	0.51		14.86	6.18	2.91		100.00
Max.		59.23	0.00	5.50	1.53	11.12	40.63	1.23	3.21	1.75	3.82	16.53	31.95	2.91	0.95	
Min.		10.26	0.00	0.24	0.32	0.15	11.53	1.23	0.84	0.35	0.53	1.56	2.99	2.51	0.95	

All results in weight%

Sample: Zr5-2H 10.10.2019 14:19:11

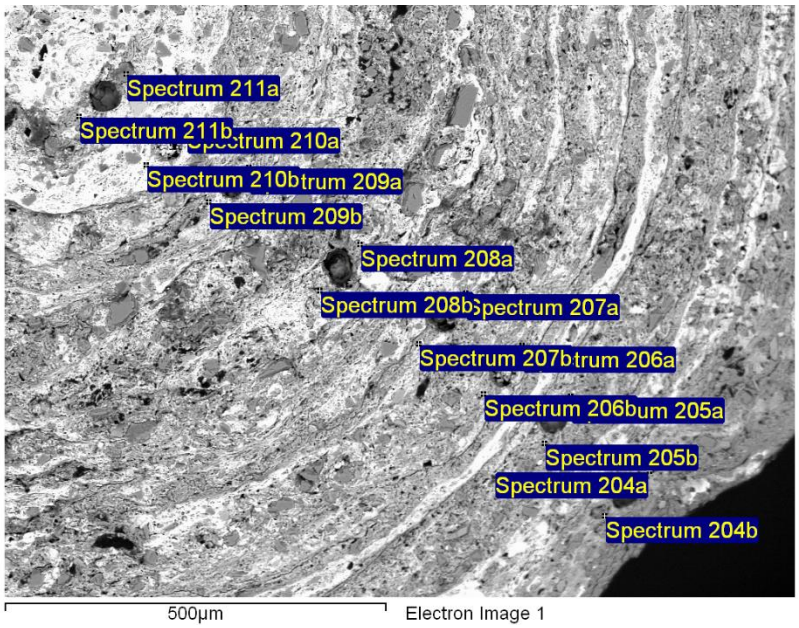

Processing option : All elements analysed (Normalised)

Spectrum	In stats.	O	Na	Mg	Al	Si	Cl	K	Ca	Ti	Mn	Fe	Ba	Total
Spectrum 204a	Yes	43.75		1.63	7.09	18.43		3.67		0.98	5.45	18.99		100.00
Spectrum 204b	Yes	55.78		1.46	5.82	21.62	0.15	1.56	0.34		5.62	6.35	1.30	100.00
Spectrum 205a	Yes	19.84		1.41	4.96	13.42		3.80	0.82	0.85	11.68	43.21		100.00
Spectrum 205b	Yes	52.95	1.75	1.29	7.47	19.80		2.23	0.35	0.43	2.50	11.22		100.00
Spectrum 206a	Yes	46.65		3.70	5.95	18.79		2.73	0.47	0.72	5.98	15.00		100.00
Spectrum 206b	Yes	58.10		1.36	6.86	13.86		2.42	0.32	4.05	4.67	8.36		100.00
Spectrum 207a	Yes	45.40		1.46	6.29	17.91		2.65	0.90	0.72	7.18	17.49		100.00
Spectrum 207b	Yes	47.05	0.31	1.02	5.22	11.65		1.54	0.72		16.82	12.60	3.06	100.00
Spectrum 208a	Yes	21.29		0.31	4.09	17.17		6.40	0.62		29.05	14.11	6.95	100.00
Spectrum 208b	Yes	56.16		1.26	8.94	17.11		4.26		0.82	4.85	6.59		100.00
Spectrum 209a	Yes	54.03		1.19	5.89	16.13		2.11	0.47		10.92	7.37	1.89	100.00
Spectrum 209b	Yes	56.88	0.37	1.57	5.27	12.00		1.32	0.60		13.24	6.34	2.42	100.00
Spectrum 210a	Yes	52.96		0.77	3.32	7.43		0.87	0.35		24.36	4.14	5.80	100.00
Spectrum 210b	Yes	40.51		0.90	3.01	6.31		1.19	0.43		35.03	4.85	7.77	100.00
Spectrum 211a	Yes	58.89	7.16		8.11	25.58					0.26			100.00
Spectrum 211b	Yes	28.99		0.33	2.79	12.43		5.10	0.78		34.52	7.76	7.30	100.00
Max.		58.89	7.16	3.70	8.94	25.58	0.15	6.40	0.90	4.05	35.03	43.21	7.77	
Min.		19.84	0.31	0.31	2.79	6.31	0.15	0.87	0.32	0.43	0.26	4.14	1.30	

All results in weight%

Sample: Zr5-5H 10.10.2019 14:43:25

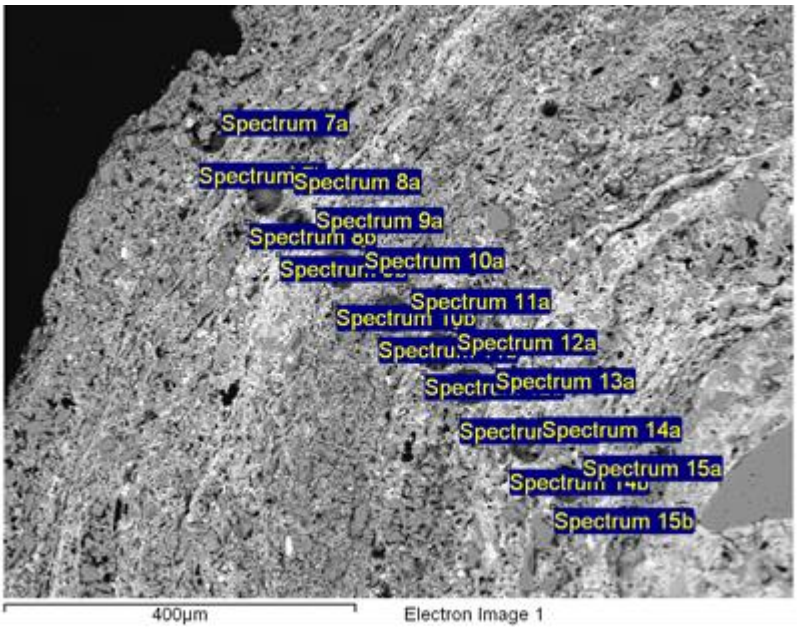

Processing option : All elements analysed (Normalised)

Spectrum	In stats.	O	Na	Mg	Al	Si	Cl	K	Ca	Ti	Mn	Fe	Ba	Ce	Total
Spectrum 7a	Yes	25.48		1.00	11.13	31.16		6.98		1.24	5.49	17.54			100.00
Spectrum 7b	Yes	58.27		1.67	9.85	18.62		4.11		1.02	0.84	5.62			100.00
Spectrum 8a	Yes	66.82		0.43	1.47	28.90		0.42			0.56	1.40			100.00
Spectrum 8b	Yes	42.01		1.26	5.94	20.61	0.51	3.07	0.77	0.72	18.23	6.89			100.00
Spectrum 9a	Yes	57.68	3.83	0.45	6.61	20.39		1.80		0.53	5.55	2.68		0.48	100.00
Spectrum 9b	Yes	57.91		0.29	1.42	34.36		0.47		0.45	3.74	1.35			100.00
Spectrum 10a	Yes	57.11	3.70	0.56	6.88	21.86		1.24	0.58	0.22	4.73	3.13			100.00
Spectrum 10b	Yes	23.17		1.23	6.53	13.34	0.57	3.01	1.14	0.65	30.65	16.80	2.92		100.00
Spectrum 11a	Yes	62.05	5.99	0.20	7.71	21.53		0.53	0.55		0.84	0.60			100.00
Spectrum 11b	Yes	39.91	0.84	0.72	9.59	18.64		7.23		0.68	8.05	14.35			100.00
Spectrum 12a	Yes	61.20		1.79	5.00	13.71	7.71	1.62			5.23	3.74			100.00
Spectrum 12b	Yes	56.46			7.74	25.13		9.73			0.57	0.36			100.00
Spectrum 13a	Yes	48.11		1.40	6.93	15.05		2.47	0.57	0.39	14.61	8.30	2.16		100.00
Spectrum 13b	Yes	34.40		0.90	6.29	13.10	0.25	3.85	0.68		24.58	12.19	3.75		100.00
Spectrum 14a	Yes	48.60		0.22	2.41	39.07		3.14		0.55	4.21	1.79			100.00
Spectrum 14b	Yes	48.43		1.34	5.35	11.70		2.24	0.76	0.38	22.08	5.09	2.63		100.00
Spectrum 15a	Yes	57.60		1.12	4.29	10.43		2.01	0.24	12.65	7.63	4.02			100.00
Spectrum 15b	Yes	24.05		0.30	2.20	35.18		2.36		1.13	21.40	13.37			100.00
Max.		66.82	5.99	1.79	11.13	39.07	7.71	9.73	1.14	12.65	30.65	17.54	3.75	0.48	
Min.		23.17	0.84	0.20	1.42	10.43	0.25	0.42	0.24	0.22	0.56	0.36	2.16	0.48	

All results in weight%

Sample: Zr5-6H 10.10.2019 14:29:04

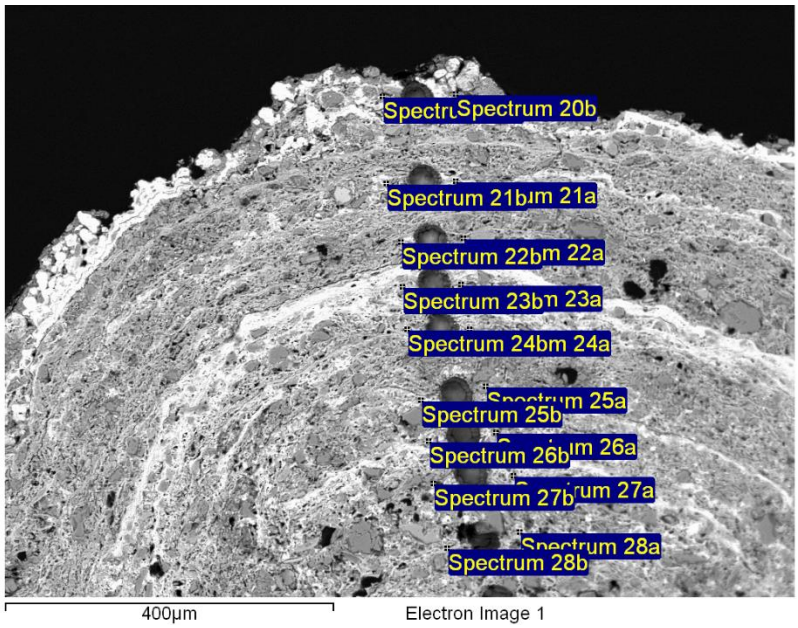

Processing option : All elements analysed (Normalised)

Spectrum	In stats.	O	F	Na	Mg	Al	Si	Cl	K	Ca	Ti	Mn	Fe	Ba	Total
Spectrum 20a	Yes	50.77			1.21	8.68	17.53		3.45		0.38	10.89	4.90	2.20	100.00
Spectrum 20b	Yes	51.46			2.54	8.90	19.69		2.15	0.28		5.81	7.57	1.60	100.00
Spectrum 21a	Yes	45.79			1.35	7.10	14.69		2.68	0.65	0.77	12.71	11.83	2.43	100.00
Spectrum 21b	Yes	59.42		0.38	1.60	5.02	24.80		1.15	0.27	0.27	3.19	3.91		100.00
Spectrum 22a	Yes	57.83			0.71	3.53	28.13		1.01	0.26	1.56	3.12	3.85		100.00
Spectrum 22b	Yes	15.09			0.56	3.83	10.93		2.81	1.02		29.85	30.77	5.14	100.00
Spectrum 23a	Yes	52.01			1.88	7.63	14.75		2.54	0.52		10.39	7.83	2.44	100.00
Spectrum 23b	Yes	28.57			1.12	6.34	20.59		3.02	0.80		23.22	11.54	4.79	100.00
Spectrum 24a	Yes	31.21			0.78	5.54	26.09		3.38	0.88		16.45	12.55	3.11	100.00
Spectrum 24b	Yes	64.03		0.19	0.78	10.03	15.63		3.61		0.39	3.16	2.19		100.00
Spectrum 25a	Yes	52.17			2.36	7.90	18.74		1.70	0.78	0.29	3.14	12.92		100.00
Spectrum 25b	Yes	56.26	0.00		1.24	5.32	11.31		1.49	0.65	0.69	14.64	6.03	2.37	100.00
Spectrum 26a	Yes	48.01			0.95	5.79	19.55	0.76	2.58	0.75	0.67	7.89	13.04		100.00
Spectrum 26b	Yes	47.81			1.12	5.10	10.54		1.60	0.76	0.35	21.57	7.70	3.46	100.00
Spectrum 27a	Yes	20.85			0.52	3.95	11.95		3.19	0.67		36.32	16.66	5.88	100.00
Spectrum 27b	Yes	37.92			1.12	5.32	12.26	1.01	2.45	1.17	1.91	23.99	12.85		100.00
Spectrum 28a	Yes	56.92		0.68	0.96	8.84	14.98		2.71	0.37		8.21	4.76	1.58	100.00
Spectrum 28b	Yes	56.07			1.75	7.04	14.00		2.03	0.54		9.67	6.80	2.09	100.00
Max.		64.03	0.00	0.68	2.54	10.03	28.13	1.01	3.61	1.17	1.91	36.32	30.77	5.88	
Min.		15.09	0.00	0.19	0.52	3.53	10.54	0.76	1.01	0.26	0.27	3.12	2.19	1.58	

All results in weight%

Sample: Zr5-6H 10.10.2019 14:34:20

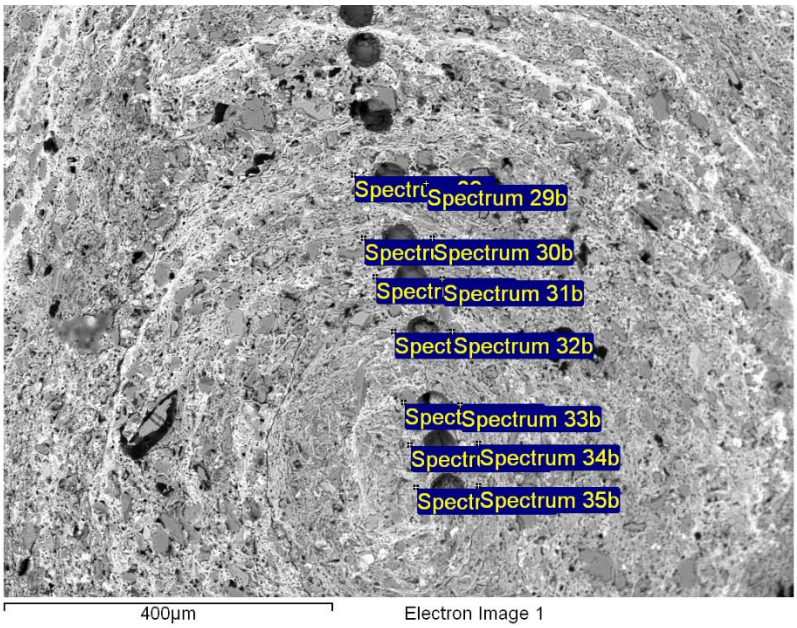

Processing option : All elements analysed (Normalised)

Spectrum	In stats.	O	F	Na	Mg	Al	Si	K	Ca	Ti	Mn	Fe	Ba	Total
Spectrum 29a	Yes	55.65			1.27	6.14	12.42	1.78	0.50		13.52	5.91	2.81	100.00
Spectrum 29b	Yes	57.58	0.00		1.72	7.23	15.44	2.32	0.33	0.42	8.50	4.89	1.58	100.00
Spectrum 30a	Yes	14.69			0.69	5.40	12.31	7.15		2.13	27.06	30.57		100.00
Spectrum 30b	Yes	42.90		0.51	1.03	8.06	19.50	3.36	0.84		12.56	8.93	2.31	100.00
Spectrum 31a	Yes	21.02			0.80	4.91	11.11	7.24	1.32	1.52	21.71	30.38		100.00
Spectrum 31b	Yes	44.64	0.00		2.36	6.96	17.25	4.14	0.54	1.22	11.81	11.08		100.00
Spectrum 32a	Yes	51.56			1.49	7.76	16.08	2.48	0.56	0.36	9.32	8.89	1.51	100.00
Spectrum 32b	Yes	43.89			0.28	1.39	50.67	0.59			1.03	2.14		100.00
Spectrum 33a	Yes	64.14			0.32	1.94	32.12	0.83		0.24		0.42		100.00
Spectrum 33b	Yes	55.94			1.96	8.56	17.42	2.88	0.39	0.48	4.59	7.78		100.00
Spectrum 34a	Yes	51.67			0.85	10.66	19.26	5.42		0.66	6.78	4.70		100.00
Spectrum 34b	Yes	51.95		0.29	1.43	7.73	15.74	2.03	0.54		6.20	12.55	1.54	100.00
Spectrum 35a	Yes	55.87			1.81	8.11	15.43	2.25	0.88	0.51	5.68	7.93	1.53	100.00
Spectrum 35b	Yes	44.86			1.42	9.32	19.58	3.17	0.75		7.78	11.32	1.79	100.00
Max.		64.14	0.00	0.51	2.36	10.66	50.67	7.24	1.32	2.13	27.06	30.57	2.81	
Min.		14.69	0.00	0.29	0.28	1.39	11.11	0.59	0.33	0.24	1.03	0.42	1.51	

All results in weight%

Sample: Zr5-9D 10.10.2019 11:27:36

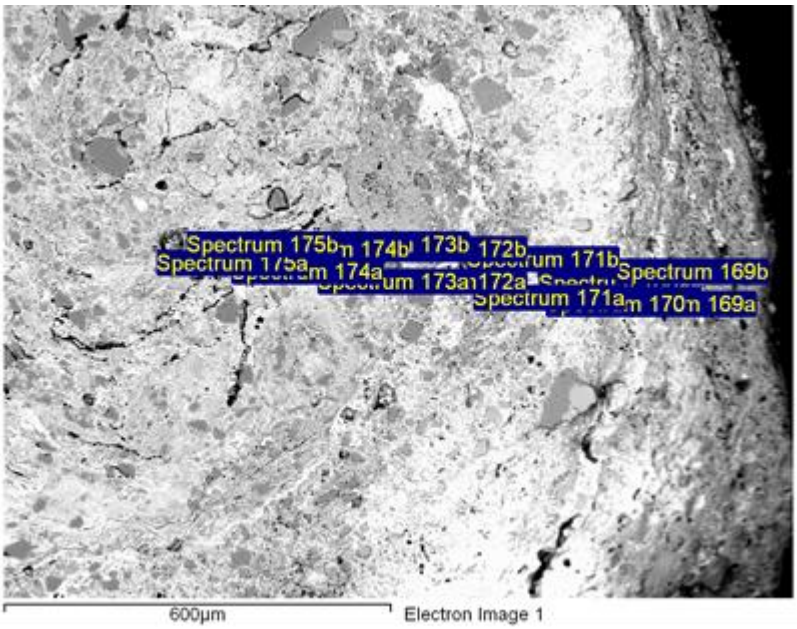

Processing option : All elements analysed (Normalised)

Spectrum	In stats.	O	Na	Mg	Al	Si	P	K	Ca	Ti	Mn	Fe	As	Ba	Total
Spectrum 168a	Yes	48.81		1.53	7.08	22.43		2.95	0.47		1.03	15.70			100.00
Spectrum 168b	Yes	49.66		1.94	7.74	18.41	0.28	3.22	0.35	0.32	0.42	17.65			100.00
Spectrum 169a	Yes	61.04	2.04	0.75	5.73	21.07		1.08	0.25	0.30		7.73			100.00
Spectrum 169b	Yes	32.20		0.48	3.26	10.46	0.50	1.86	0.61	0.60	0.92	49.10			100.00
Spectrum 170	Yes	57.59		1.02	6.83	13.29	0.33	1.67	0.28			18.98			100.00
Spectrum 171a	Yes	44.67		1.96	4.65	7.57		1.53	0.37		26.72	7.28	0.00	5.25	100.00
Spectrum 171b	Yes	51.41		1.57	7.30	13.56	0.15	2.57	0.32	0.30	2.69	20.12			100.00
Spectrum172a	Yes	38.25		1.09	5.18	12.87	0.34	2.02	0.53	0.61	0.94	38.17			100.00
Spectrum 172b	Yes	4.51			1.16	4.84		3.25			2.51	83.73			100.00
Spectrum 173a	Yes	49.56		1.04	7.51	18.44	0.26	2.53			0.32	20.34			100.00
Spectrum 173b	Yes	64.06		0.34	1.90	27.72		0.44	0.12			5.42			100.00
Spectrum 174a	Yes	42.79	0.30	1.48	8.79	11.52	0.20	1.37	0.74	0.58	0.63	31.59			100.00
Spectrum 174b	Yes	44.01		2.73	6.61	17.87	0.39	2.67	0.53	0.33	0.68	24.20			100.00
Spectrum 175a	Yes	36.07		2.41	6.06	14.74	0.55	3.03	1.84	0.49		34.80			100.00
Spectrum 175b	Yes	51.60		1.13	7.45	15.82	0.49	2.63	0.60			20.27			100.00
Max.		64.06	2.04	2.73	8.79	27.72	0.55	3.25	1.84	0.61	26.72	83.73	0.00	5.25	
Min.		4.51	0.30	0.34	1.16	4.84	0.15	0.44	0.12	0.30	0.32	5.42	0.00	5.25	

All results in weight%

Sample: Zr5-10D 10.10.2019 10:45:02

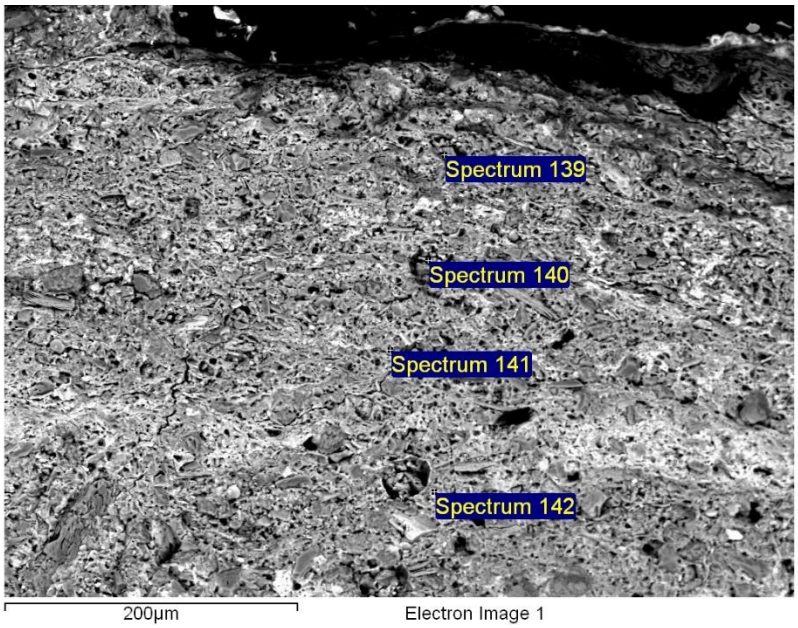

Processing option : All elements analysed (Normalised)

Spectrum	In stats.	O	Mg	Al	Si	K	Ca	Ti	Mn	Fe	Total
Spectrum 139	Yes	61.17	0.85	4.13	25.70	1.07	0.20	0.29	3.09	3.49	100.00
Spectrum 140	Yes	46.01	1.24	5.39	17.77	2.47		0.92	11.64	14.55	100.00
Spectrum 141	Yes	38.25	1.87	7.98	25.86	4.10	0.50	1.26	7.68	12.50	100.00
Spectrum 142	Yes	50.47	1.47	8.68	17.82	4.44	0.38	1.08	5.79	9.86	100.00
Max.		61.17	1.87	8.68	25.86	4.44	0.50	1.26	11.64	14.55	
Min.		38.25	0.85	4.13	17.77	1.07	0.20	0.29	3.09	3.49	

All results in weight%

Sample: Zr5-10D 10.10.2019 10:48:45

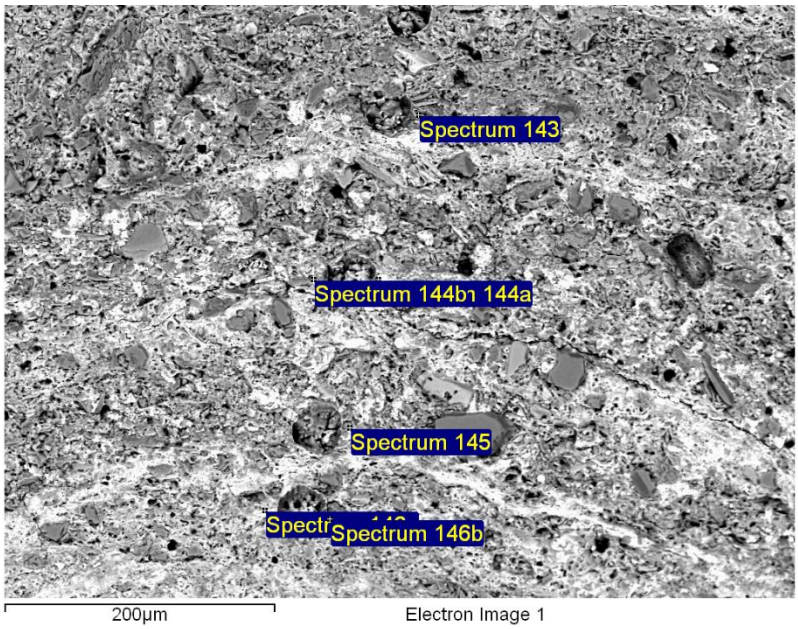

Processing option : All elements analysed (Normalised)

Spectrum	In stats.	O	Na	Mg	Al	Si	K	Ca	Ti	Mn	Fe	Ba	Total
Spectrum 143	Yes	58.84	0.30	1.59	10.02	16.25	3.67	0.45	0.35	2.83	5.69		100.00
Spectrum 144a	Yes	32.49				0.54			1.58	0.54	64.85		100.00
Spectrum 144b	Yes	61.23		0.85	4.18	25.64	1.07	0.20	0.35	2.64	3.82		100.00
Spectrum 145	Yes	55.49		2.01	6.90	16.92	1.76	1.11	1.31	4.75	9.74		100.00
Spectrum 146a	Yes	45.31		1.63	4.82	12.66	1.50	0.56		23.72	6.25	3.56	100.00
Spectrum 146b	Yes	45.75		2.22	8.58	17.59	3.14	0.50	0.33	11.68	8.47	1.73	100.00
Max.		61.23	0.30	2.22	10.02	25.64	3.67	1.11	1.58	23.72	64.85	3.56	
Min.		32.49	0.30	0.85	4.18	0.54	1.07	0.20	0.33	0.54	3.82	1.73	

All results in weight%

Sample: Zr5-10D 10.10.2019 10:53:21

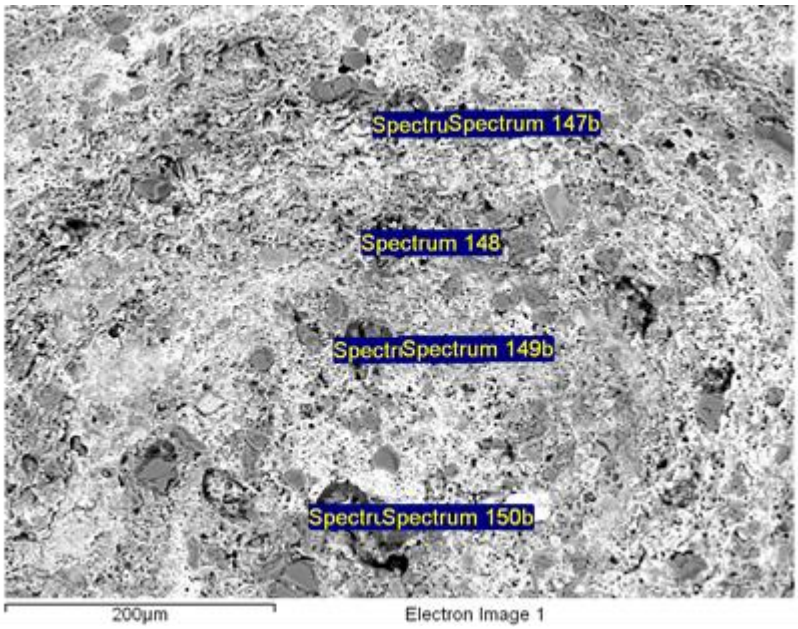

Processing option : All elements analysed (Normalised)

Spectrum	In stats.	O	Na	Mg	Al	Si	P	S	K	Ca	Ti	Mn	Fe	Ba	Total
Spectrum 147a	Yes	57.52		0.29	1.43	35.52			0.70			2.40	1.65	0.49	100.00
Spectrum 147b	Yes	48.28		1.18	7.20	14.99			3.09	0.42	0.57	15.17	6.41	2.71	100.00
Spectrum 148	Yes	41.77		1.00	10.21	16.73	0.74	0.86	6.45	0.65		9.35	10.24	2.00	100.00
Spectrum 149a	Yes	51.78		1.10	9.97	19.38			5.07			6.87	4.30	1.52	100.00
Spectrum 149b	Yes	55.84		1.13	5.17	21.90			1.80			8.35	4.13	1.67	100.00
Spectrum 150a	Yes	65.80			0.19	33.68						0.32			100.00
Spectrum 150b	Yes	60.78	5.43	0.82	7.59	19.75			0.82	0.25	0.26	2.14	2.17		100.00
Max.		65.80	5.43	1.18	10.21	35.52	0.74	0.86	6.45	0.65	0.57	15.17	10.24	2.71	
Min.		41.77	5.43	0.29	0.19	14.99	0.74	0.86	0.70	0.25	0.26	0.32	1.65	0.49	

All results in weight%

Sample: Zr5-12D 10.10.2019 10:34:10

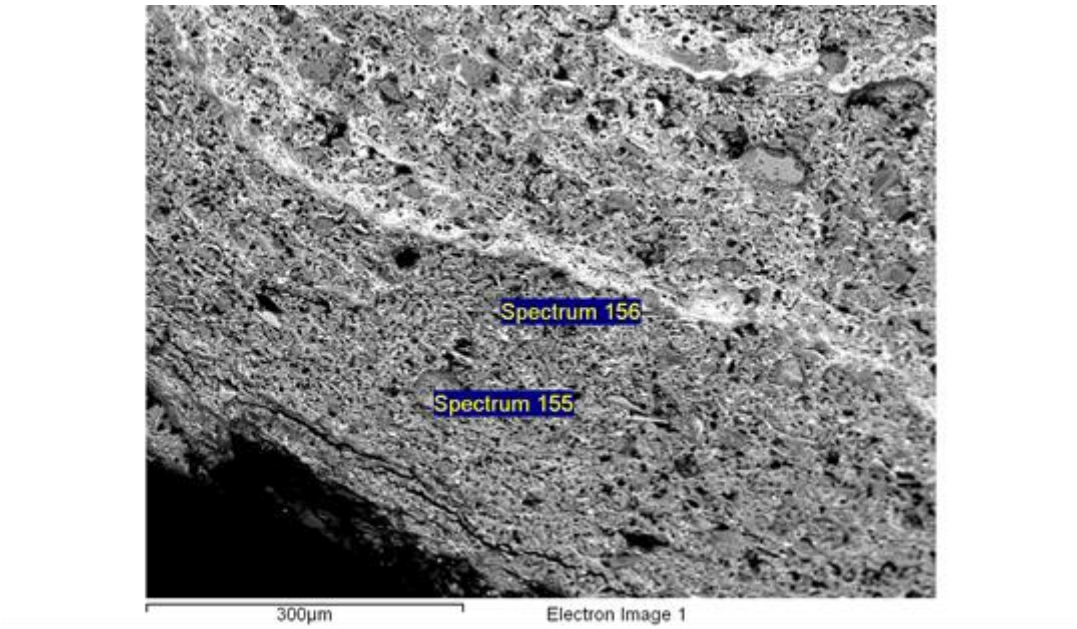

Processing option : All elements analysed (Normalised)

Spectrum	In stats.	O	Na	Mg	Al	Si	K	Ca	Mn	Fe	Total
Spectrum 155	Yes	61.34		4.55	3.75	22.42	0.75	0.15	0.88	6.15	100.00
Spectrum 156	Yes	43.64	4.90		11.11	36.97	0.89	0.85		1.64	100.00
Max.		61.34	4.90	4.55	11.11	36.97	0.89	0.85	0.88	6.15	
Min.		43.64	4.90	4.55	3.75	22.42	0.75	0.15	0.88	1.64	

All results in weight%

Sample: Zr5-12D 10.10.2019 10:34:41

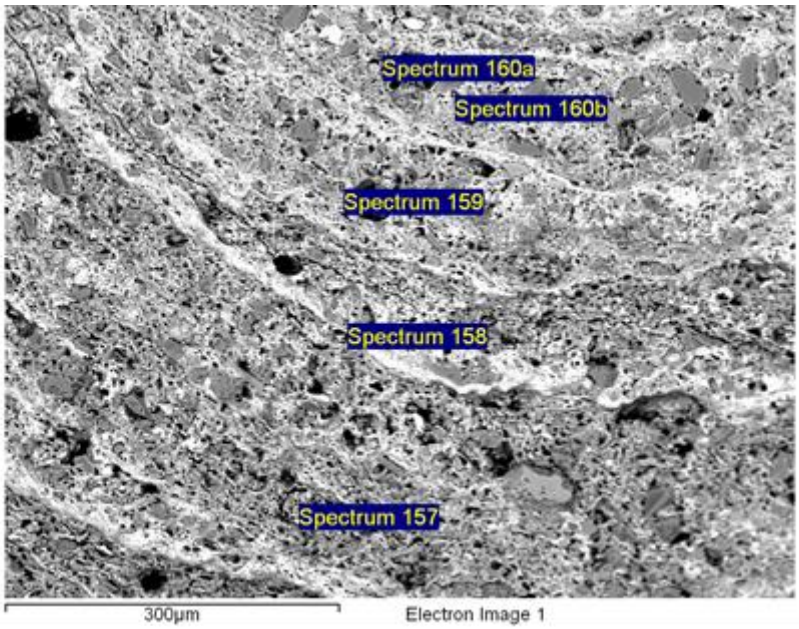

Processing option : All elements analysed (Normalised)

Spectrum	In stats.	O	Na	Mg	Al	Si	K	Ca	Ti	Mn	Fe	Ba	Total
Spectrum 157	Yes	43.56		1.06	6.37	27.40	2.94	0.47	0.90	9.86	7.43		100.00
Spectrum 158	Yes	57.48		1.64	8.54	16.09	3.40	0.27		6.23	5.09	1.26	100.00
Spectrum 159	Yes	53.34		2.30	7.37	13.91	2.26	0.39	0.35	11.38	7.14	1.54	100.00
Spectrum 160a	Yes	34.01	0.72	0.31	7.30	23.94	10.34			16.08	4.44	2.86	100.00
Spectrum 160b	Yes	62.18		0.16	0.61	32.71	0.28			2.23	1.44	0.38	100.00
Max.		62.18	0.72	2.30	8.54	32.71	10.34	0.47	0.90	16.08	7.43	2.86	
Min.		34.01	0.72	0.16	0.61	13.91	0.28	0.27	0.35	2.23	1.44	0.38	

All results in weight%

Sample: Zr5-12D 10.10.2019 10:36:28

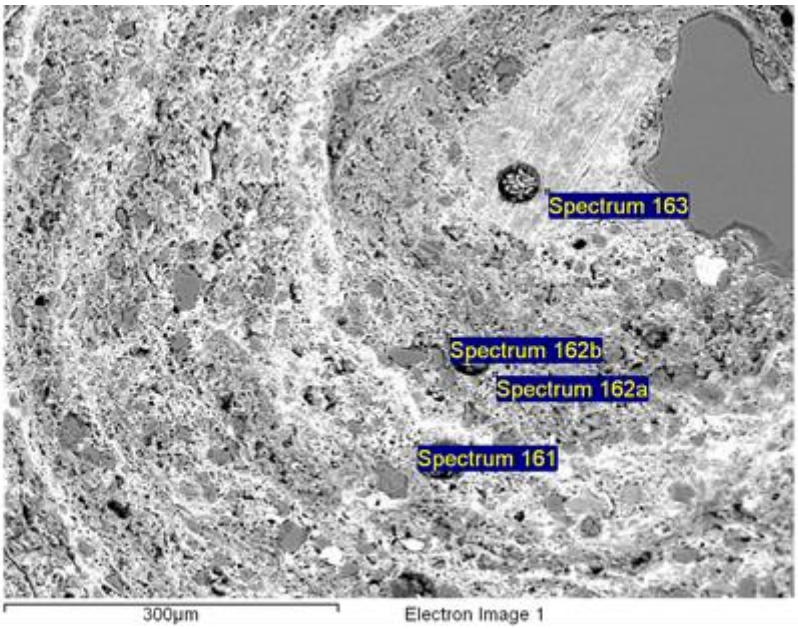

Processing option : All elements analysed (Normalised)

Spectrum	In stats.	O	Mg	Al	Si	K	Ca	Ti	Mn	Fe	Ba	Ce	Total
Spectrum 161	Yes	49.71	1.34	7.82	15.43	3.19	0.49		12.35	7.26	2.42		100.00
Spectrum 162a	Yes	55.32	1.01	5.54	18.01	1.84	0.47	0.45	10.02	5.59	1.73		100.00
Spectrum 162b	Yes	58.09	0.72	3.22	19.90	1.26	0.35	1.14	10.61	4.19		0.52	100.00
Spectrum 163	Yes	53.67	2.10	11.78	17.36	5.63				9.46			100.00
Max.		58.09	2.10	11.78	19.90	5.63	0.49	1.14	12.35	9.46	2.42	0.52	
Min.		49.71	0.72	3.22	15.43	1.26	0.35	0.45	10.02	4.19	1.73	0.52	

All results in weight%